UNIVERSIDAD AUTÓNOMA DE SAN LUIS POTOSÍ

EL INSTITUTO DE FÍSICA Y LA FACULTAD DE CIENCIAS

THESIS

A THEORETICAL APPROACH TO STRUCTURAL AND DYNAMICAL PROPERTIES OF IONIC LIQUIDS

PROGRAM:

PH.D. IN INTERDISCIPLINARY SCIENCES

PRESENT:

JUAN CARLOS AVILÉS SÁNCHEZ

THESIS ADVISORS:
DR. PEDRO EZEQUIEL RAMÍREZ GONZÁLEZ
DR. GUILLERMO IVÁN GUERRO GARCÍA

SAN LUIS POTOSÍ, SAN LUIS POTOSÍ, August 2025

A THEORETICAL APPROACH TO STRUCTURAL AND DYNAMICAL PROPERTIES OF IONIC LIQUIDS

Contents

Acknowledgements

I would like to express my sincere gratitude to the Consejo Nacional de Ciencia y Tecnología (CONACYT) for the financial support provided throughout grants: ”becas de posgrado”, IxM No. 1631 and 7119. As well the grant CF-2023-I-1013. Without their support, this work would not have been possible.

My deepest appreciation goes to Dr. Pedro Ezequiel Ramírez González, who was far more than an academic advisor. His guidance, dedication, and unwavering confidence in my work were fundamental at every stage of this project. I am profoundly grateful for his constant availability, regardless of the day or time. No matter how many times I asked the same question, he always responded with patience, kindness, and often with enthusiasm—as if explaining was his way of celebrating learning. He continuously sought new ways to help me understand, always making sure the concepts were truly clear. His commitment, generosity, and human warmth have left a lasting impact on both my academic journey and personal growth.

I am also thankful to Dr. Guillermo Iván Guerro García for allowing me to pursue my doctoral studies under his supervision. For providing technical resources that were essential to my development. His willingness to share computational resources greatly accelerated my progress, and the learning resources he provided significantly contributed to deepening my understanding of programming.

To Laboratorio Nacional de Ingeniería de la Materia Fuera de Equilibrio (LANIMFE), thank you for granting me a dedicated workspace, which was essential for carrying out my project effectively.

To my mother, with all my love and gratitude—none of this would have been possible without you. Thank you for your endless sacrifices, your words of encouragement, your unconditional support, and for believing in me even during the moments when I doubted myself. You are the reason I never gave up. This achievement is as much yours as it is mine.

Finally, to my wife, thank you for your unwavering support, patience, and love throughout this journey. Your presence has been a source of strength and balance during this demanding yet rewarding stage of my life.

Resumen

Los líquidos iónicos (ILs) a temperatura ambiente son sustancias formadas completamente por iones, usualmente grandes cationes orgánicos combinados con aniones orgánicos o inorgánicos, con puntos de fusión por debajo de 100 °C. Desde el primer IL reportado en 1914, estos compuestos han sido objeto de amplia investigación debido a sus propiedades físico-químicas únicas, como baja volatilidad, alta conductividad iónica y estabilidad térmica, así como su gran diversidad estructural. Esta tesis evalúa la validez de un marco teórico basado en la ecuación de Langevin generalizada auto-consistente (SCGLE) aplicado al modelo primitivo de líquidos iónicos, comparando sus predicciones con simulaciones de dinámica molecular de todos los átomos.

Un aspecto clave es el comportamiento vítreo que presentan los ILs a temperatura ambiente, incluyendo la aparición de estados parcialmente arrestados donde un tipo de ion queda inmovilizado mientras el otro permanece móvil, un fenómeno influenciado por la asimetría de tamaño y carga entre iones. Estos estados son similares a los observados en materiales superiónicos usados en baterías.

Se realizaron simulaciones moleculares en una serie de ILs basados en imidazolium con el anión tetrafluoroborato, para estudiar cómo la flexibilidad de los cationes afecta sus propiedades estructurales y dinámicas. En particular, se observa que en el sistema $EMI^{+}BF_{4}^{-}$ el anión queda inmovilizado mientras el catión permanece fluido, validando predicciones del modelo teórico. Este trabajo busca avanzar en la comprensión fundamental del comportamiento dinámico de líquidos iónicos y su transición vítrea, con potenciales aplicaciones en materiales conductores a temperatura ambiente.

Abstract

Room-temperature ionic liquids (ILs) are substances composed entirely of ions, typically large organic cations paired with organic or inorganic anions, with melting points below 100 °C. Since the first reported IL in 1914, they have been extensively studied due to their unique physicochemical properties such as low volatility, high ionic conductivity, and thermal stability, as well as their vast structural diversity. This thesis evaluates the validity of a theoretical framework based on the Self-Consistent Generalized Langevin Equation (SCGLE) applied to the primitive model of ionic liquids, by comparing its predictions with all-atom molecular dynamics simulations.

A key feature of ILs is their glassy behavior at room temperature, including the presence of partially arrested states where one ion species becomes immobilized while the other remains mobile, a phenomenon driven by size and charge asymmetry between ions. Such states resemble those observed in superionic materials used in battery technologies.

Molecular dynamics simulations were performed on a series of imidazolium-based ILs with the tetrafluoroborate anion to investigate the influence of cation flexibility on their structural and dynamic properties. In particular, the $EMI^+BF_4^-$ system exhibits immobilization of the anion while the cation remains fluid, confirming theoretical model predictions. This work aims to deepen the fundamental understanding of ionic liquids' dynamic behavior and glass transition, with potential applications in room-temperature conductive materials.

Chapter 1

Introduction

Room-temperature molten salts, also known as ionic liquids (ILs), are substances composed entirely of ions. They typically consist of large organic cations paired with organic or inorganic anions and have a melting point below 100 °C. The first IL, ethyl ammonium nitrate, was reported by Paul Walden in 1914 [1]. Since then, ILs have emerged as a significant field of scientific research, leading to extensive experimental, theoretical, and simulation studies aimed at understanding their physical and chemical properties [1]. Indeed, several multidisciplinary studies on ILs are emerging, including chemistry, materials science, chemical engineering, and environmental science, and they have also become a very active field due to their promising applications in the industry [2, 3].

Some of the physicochemical properties of ILs are non-volatile, non-flammable, thermally stable and with high ionic conductivity. The vast number of possible cation-anion combinations that qualify as ILs results in a wide range of behaviors. As a consequence, ILs have been categorized into various types, including room-temperature ionic liquids (RTILs), task-specific ionic liquids (TSILs), polyionic liquids (PILs), and supported ionic liquid membranes (SILMs), the latter incorporating IL composites supported on metal-organic frameworks (MOFs) [1]. It is important to note that deep eutectic solvents (DESs) are not discussed in this thematic issue since DESs and ILs belong to distinct solvent families [1]. However, despite the diversity of ILs, many open questions remain unanswered in this field. Despite the intense research on the topic, the complexity of ILs represents a great challenge from the fundamental theoretical point of view since most of our knowledge of ILs is due to experimental and computational simulation work. Some years ago, a theoretical framework was developed by Farias-Anguiano and co-workers [4] by combining the Ornstein-Zernike solution for the primitive model of ionic liquids under the mean-spherical approximation (MSA) with the Self-Consistent Generalized Langevin Equation (SCGLE) theory for dynamical properties and dynamic arrest. This thesis aims to probe the validity limits of the previously mentioned theoretical framework by comparing its predictions with all-atom molecular dynamics simulations of model ILs.

An important characteristic of ILs is that they possess a glassy behaviour at room temperatures [5]. Especially for this feature, the theoretical framework based on the SCGLE theory, let us refer it as the Primitive model-SCGLE (PM-SCGLE) framework, is useful leading to interesting predictions about the glassy dynamics and arrested states of ILs [6]. The most important prediction obtained from PM-SCGLE is [4, 6] the prediction of partially-arrested states, where one of the ions becomes arrested while the other ions are able to diffuse. These domains of mixed states are associated with the size and charge asymmetries between ions.

This type of partially arrested state has been observed in materials classified as superionic conductors [9]. Both crystalline and glassy superionic conductors have been extensively used in battery technology since the 1980s [10]. However, these materials often have highly complex compositions, making direct comparisons with the theoretical framework of SCGLE challenging. Interestingly, ILs exhibit glassy behavior at room temperature, making them more suitable for theoretical predictions [11, 12].

The glass transition in ionic liquids is a phenomenon of great interest due to its fundamental and applied implications. Unlike conventional liquids, ionic liquids exhibit a strong correlation between electrostatic interactions and relaxation dynamics, leading to complex behaviors during their transition to the glassy state. In this regard, the glass transition in ILs is characterized by the emergence of heterogeneous dynamics, where some ions become trapped in a structurally rigid matrix while others retain a certain degree of mobility. This mixed behavior is crucial for applications in energy storage and electronics, as it allows fine-tuning of properties such as ionic conductivity and thermal stability in advanced devices [13, 14].

From a theoretical perspective, understanding the glass transition in ILs remains a challenge, as these systems exhibit a unique combination of long-range interactions and structural frustration. In particular, the presence of asymmetry in size and charge between cations and anions influences the formation of partially arrested states, a feature that distinguishes them from other conventional glassy materials. Molecular dynamics simulations have proven to be valuable tools for exploring these phenomena at a microscopic level, allowing for an analysis of the relationship between local structure and ion dynamics. By comparing these simulations with theoretical predictions based on SCGLE, it is possible to assess the extent to which a simplified model can capture the richness of behaviors observed in highly asymmetric ILs [14].

The interest in the glass transition of ionic liquids is not limited to theoretical research but also has significant technological implications. In the development of materials for batteries, supercapacitors, and electrochemical devices, the ability to modulate ionic mobility through control of the glass transition is a key factor. In particular, the possibility of designing ILs with partially arrested states could open new avenues for the development of electrolytes with optimized properties, combining high conductivity with mechanical stability. Thus, a detailed exploration of the relationship between structure, dynamics, and the glass transition in ILs not only contributes to advancing fundamental knowledge but also has the potential to significantly impact the design of novel functional

materials [15].

In the present work, we present a comprehensive comparison between an imidazolium-based ILs, 1-Ethyl-3Methyl-Imidazolium tetrafluoroborate ($EMI^+BF_4^-$), 1-Butyl-3Methyl-Imidazolium tetrafluoroborate ($BMI^+BF_4^-$), 1-Hexyl-3Methyl-Imidazolium tetrafluoroborate ($HMI^+BF_4^-$), 1-Octyl -3Methyl-Imidazolium tetrafluoroborate ($OMI^+BF_4^-$) , and 1-Decyl-3Methyl-Imidazolium tetrafluoroborate ($DMI^+BF_4^-$). The anion tetrafluoroborate (BF_4^-) was chosen because we want to have a very rigid anion which permits to study the influence of the flexibility of the cations. We have conducted molecular dynamics (MD) simulations to investigate the structural and dynamical properties of these ILs using an all-atom molecular dynamics approach. Additionally, we analyze the glassy behavior of the described systems, particularly the $EMI^+BF_4^-$ system, where the emergence of partially arrested states has been observed. In this state, the small anion (BF_4^-) becomes immobilized while the large cation (EMI^+) remains fluid [7]. Therefore, this project aims to explore the existence of partially arrested states in ILs, which could pave the way for the development of novel conductive materials operating near room temperature.

The presented work consists of a comprehensive comparison between the most important predictions of the Self-Consistent Generalized Langevin Equation (SCGLE) theory applied to the Primitive Model (PM) of ionic liquids and the overall behavior observed using all-atom molecular dynamics (MD) simulations of highly-asymmetric room temperature ionic liquids (RTILs), based on imidazolium. We are trying to probe the limits of validity of our simple model based on the PM, which implies the risky assumption of considering the RTILs as charged hard spheres. Even though quite important effects were ignored, we consider that the long-range nature of coulombic interactions should dominate the overall behavior of such systems.

This work is organized as follows: Chapter 2 summarizes the most important methods and procedures. Chapter 3 discusses the results obtained from all-atom molecular dynamics simulations of selected ILs. Next, we review the theoretical predictions of the PM-SCGLE framework for systems that mimic the ILs of interest. The final chapters contain the main perspectives and conclusions for further research.

Chapter 2

Scope, objectives, methods, and procedures.

The main aim of this chapter is the description of the thesis' fundamental objectives, the detailed description of the strategy necessary to achieve the goals and a brief review of the essential methodology aspects. A detailed review of the computational methods can be consulted in appendix A.

2.1 Main purpose and objectives

In 2009, L.E. Sánchez-Díaz and co-workers [6] presented a study using the self-consistent generalized Langevin equation (SCGLE) theory of dynamic arrest to show the ergodic-nonergodic phase diagram of a classical mixture of charged hard spheres. Later, in 2016, Pedro E. Ramírez-González and co-workers [5], inspired by the work of Sánchez-Díaz, performed a molecular dynamics study where the existence of partially arrested states in imidazolium ionic liquids was shown. Recently, in 2022, Mariana E. Farias et. al., [4] a theoretical framework was incorporated to describe the structural and dynamical properties of ionic liquids. This framework is based on the SCGLE theory which predicts the dynamically arrested states of several physical systems, to simple models of charge and size asymmetric ionic liquids. Such a theoretical framework was consistent with the previous results of Ramírez-González and co-workers and with experimental measurements of superionic conductors based on phosphates. The advantage of this theoretical framework is that it is not limited to RTILs and can be applied to a wide range of ionic liquids with size and/or charge asymmetries. Indeed, the main objective of this work is to test in detail the predictions of the SCGLE using the framework developed for a larger range of size asymmetries. Hence, our overall goal is to explore the validity of the theoretical framework (from now on, let us call the Framework developed by Farias-Anguiano as PM-SCGLE) by comparing them with all-atom molecular dynamics simulations of imidazolium-based ionic liquids.

The specific objectives are:

- Implement molecular dynamics models for imidazolium-based ionic liquids.
- Studying the glassy behavior of ILs using all-atom molecular dynamics simulations.
- Implement the PM-SCGLE model for the asymmetries of simulated systems.
- Comparing the molecular dynamics results with the theoretical predictions.
- Explore the limits of validity of the PM-SCGLE framework.

2.2 Thesis road-map

In this section, we present the thesis' overall structure:

- Chapter 3 contains the results obtained from all-atom molecular dynamics simulations of imidazolium-based ionic liquids.
- In Chapter 4, the results obtained using the PM-SCGLE framework for the same size asymmetries used in the simulations are shown.
- Chapter 5 details the comparisons between the simulations and the PM-SCGLE framework.
- Chapter 6 the perspectives are discussed.
- Chapter 7 shows the conclusions.

2.3 Methodological aspects

2.3.1 Simulation details

The systems simulated throughout this thesis are those that have an imidazolium base, this means that they share the imidazolium residue (head) and differ in one of the alkyl chains length (tail). As shown in Fig. 2.1, the imidazolium residue is the pentagonal arrangement of atoms and the alkyl tail is the chain formed by CH_2 groups. The specific systems studied are the following: Ethyl-Methyl-Imidazolium (EMI^+ BF_4^-), Bthyl-Methyl-Imidazolium Tetraflourborate (BMI^+ BF_4^-), Exyl-Methyl-Imidazolium Tetraflourborate (HMI^+ BF_4^-), Octyl-Methyl-Imidazolium Tetraflourborate (OMI^+ BF_4^-), and Decyl-Methyl-Imidazolium Tetraflourborate (DMI^+ BF_4^-).

The force field parameters for EMI^+, BMI^+, HMI^+, OMI^+, and DMI^+ were obtained from reference [25], which relies on the AMBER force field [26]. The force field for BF_4^- was developed

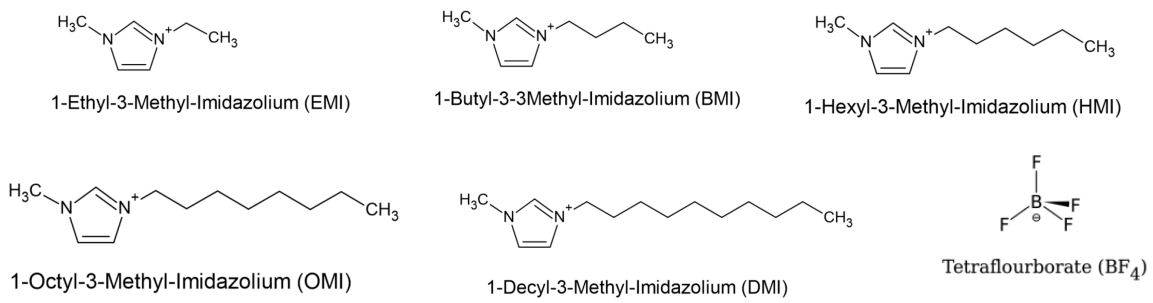

Figure 2.1: Molecular structures of the ions constituting the ILs studied in this work.

by J. de Andrade and collaborators [27]. The AMBER force field was applied to model both bonded and nonbonded interactions of the ions.

All simulations were conducted using the Gromacs 2022.2 molecular dynamics (MD) simulation package [16, 17]. Periodic boundary conditions (PBC) were imposed in all three spatial dimensions within a cubic simulation box, and a 1.6 nm cutoff was set for nonbonded interactions. Long-range electrostatic interactions [19, 20] were handled using the particle mesh Ewald (PME) method [29]. Each of the five systems consisted of 1024 ion pairs. In our study, we selected $T = 500K$ as one of the target temperatures, as experimental results have shown that this temperature is significantly above the melting point of $EMI^+BF_4^-$ [7].

2.3.2 Main elements of PM-SCGLE framework

The PM-SCGLE framework was developed with the aim of consolidating the understanding of the dynamical properties and arrested states of ionic liquids, using the SCGLE theory. This framework is used to predict the dynamical properties and arrest diagrams of ionic liquids, including charge and size asymmetric systems.

The asymptotic solution of the SCGLE theory is employed to compute dynamical arrest diagrams. Moreover, a dynamic formulation of the theory for any correlation time t can be implemented within the same system, offering additional insights into the Mean Squared Displacement behavior of all ionic species. Figure 2.2 presents the flowchart illustrating the theory's implementation (for a more detailed explanation, refer to [4]).

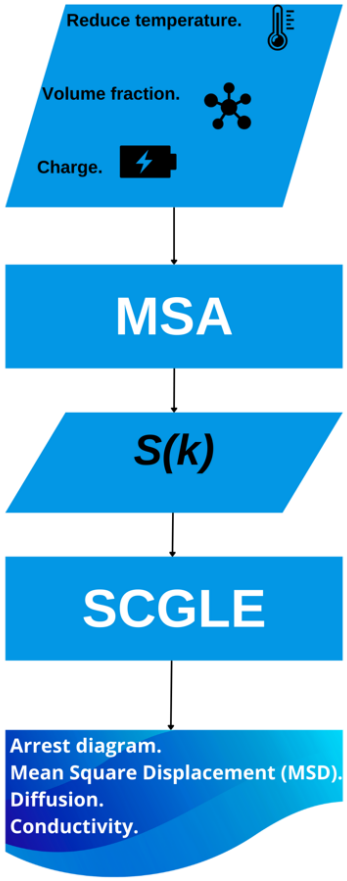

Figure 2.2: The flowchart provides a summary of the SCGLE theory implementation. An analytical solution for the structure factor is derived using specified values of reduced temperature, packing fraction, and charge. These parameters are then input into the SCGLE equations to obtain numerical solutions. The resulting outputs include various relevant dynamical properties [4].

Chapter 3

Molecular Dynamics Simulations Results

This chapter presents our main results obtained from all-atom molecular dynamics simulations of model systems of ILs. As being described previously, the main aim of this thesis is to probe the reliability and the validity limits of the SCGLE theory predictions.

In order to achieve the goal, we started by reproducing of previous results contained in references [5, 4], namely, the existence of partially-arrested states in which only one of the ions (cations or anions) are dynamically arrested while the others are free to diffuse. Such partially-arrested states depend on the charge and size asymmetries between ions. For example, size-asymmetry leads to a pair of partially arrested regions, one at high temperatures and densities, while the other is found at low temperatures and densities [4]. Such a prediction was proven true after the work of Ramirez-Gonzalez et. al. [5] where the glassy-behavior of Ethyl-Methyl-Imidazolium tetrafluoroborate (EMI-BF_4) IL was studied with all-atom MD simulations obtaining qualitative agreement with the theoretical predictions.

Let us remark that previous results were obtained within homogeneous states. However, during the development of this work, different routes which lead to homogeneous and inhomogeneous states were found. Aiming to show a comprehensive picture of the system's behavior we started with production runs at NPT conditions in order to ensure homogeneity and being able to reproduce previous results. On the other hand, we used NVT production runs in order to study inhomogeneous systems.

3.1 Homogeneous systems

3.1.1 $EMI^+BF_4^-$

In this section we are comparing the current simulation results for ($EMI^+BF_4^-$) at 500°K obtained with Gromacs 2022.2 with the previous results obtained by Ramírez - González and co-workers [7].

The main aim of doing this comparison is to corroborate that all the parameters have been adapted correctly, allowing the reproducibility of the simulation results. An schematic representation of the $EMI^+BF_4^-$ is shown in Figure 3.1.

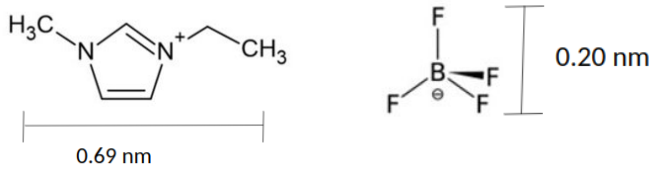

(a) EMI^+. (b) BF_4^-.

Figure 3.1: Schematic representations of the sizes of the ions studied by MD simulation. Reproduced from [60], with the permission of AIP Publishing.

Structural properties

The Radial Distribution Functions (RDFs) of anions and cations around their center of mass are calculated to examine the structural correlations between the ions. In Figure 3.2(b) the cation-cation (black line), the cation-anion (orange line) and anion-anion (red line) RDFs are shown at 500°K. Here, the center of mass of the cation is used and the same for the anion. As shown in Figure 3.2, our results for RDFs are generally consistent with the structural results obtained by Ramírez-González et. al. [7] since we can see that the peaks are the same. The RDFs exhibit well-defined features and distinct oscillatory patterns, indicating spatial correlations among the species. Specifically, the first peak in the cation-cation RDF appears at $r = 0.76$ nm, while the first peak in the anion-anion RDF is at $r = 0.69$ nm, and the first peak in the cation-anion RDF is at $r = 0.5$ nm. These peaks represent the average positions of the first neighboring ions. From Figure 3.2(b), we observe that the first peaks occur at $r = (\sigma_c + \sigma_a)/2$, where σ denotes the ionic diameter, with the subscript c referring to cations (positively charged species) and a to anions (negatively charged species).

The BF_4^- anion has a tetrahedral structure with an average size of approximately 0.20 nm, while the $EMI^+BF_4^-$ cation has an average size (measured from methyl to ethyl) of around 0.69 nm (see Fig. 3.1). Notably, the first peak of the anion-anion RDF is more than three times the size of σ_a, a characteristic feature of a Wigner glass, where the average distance between its components is significantly large [8]. Our findings suggest that cations exhibit low efficiency in screening the charge of anions due to the distribution of their charge over a larger surface. As a result, the anion-anion repulsion is stronger than the cation-cation repulsion.

Figure 3.2 shows the RDFs for T=300°K (3.2(a)), T=500°K (3.2(b)), and T=700°K (3.2(c)), where g_{+-}(r) represents $EMI^+BF_4^-$, g_{++}(r) is EMI^+EMI^+, and g_{--}(r) is $BF_4^-BF_4^-$. The primary peak of $g_{++}(r)$ is observed at $r = 0.76$ nm, while the first peak of $g_{+-}(r)$ is located around 0.5 nm. Both peaks exhibit minimal dependence on temperature. Conversely, the first peak of $g_{--}(r)$ shifts from 0.74 nm to 0.63 nm as the temperature decreases.

To demonstrate that the results are the same, it was decided to digitize the data from the article by Ramírez-González et. al [7]. The following figures present the results of the digitized data alongside the obtained data.

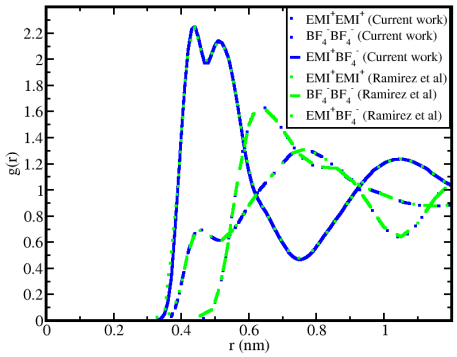

(a) Current results and results by Ramírez González et. al., at 300°K.

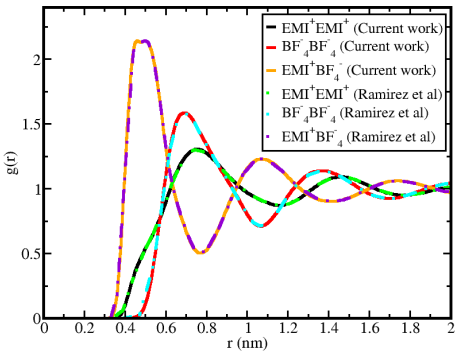

(b) Current results and results by Ramírez González et. al., at 500°K.

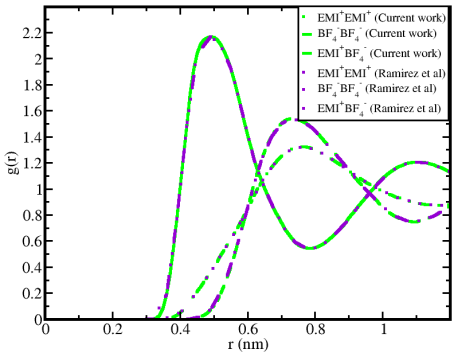

(c) Current results and results by Ramírez González et. al., at 700°K.

Figure 3.2: Radial distribution functions for the system $EMI^+BF_4^-$ at $P = 1$ atm and different temperatures.

With this, it is demonstrated that they are indeed the same, Figures 3.2 present the results we obtained along with the digitized results. In Figure 3.2(b), the solid lines in black, red, and orange

(EMI^+ EMI^+, BF_4^- BF_4^-, and EMI^+ BF_4^-, respectively) correspond to the results recently obtained, along with the digitized data. We have demonstrated that we have obtained the same results, even though we changed the final production run.

Mean Squared Displacement

The self-diffusion coefficients of the cation and anion are calculated from their Mean Squared Displacements (MSDs). The cation EMI^+, despite being heavier than the anion BF_4^-, diffuses faster, which is observed by Ramírez-González and co-workers [5]. The calculated MSDs at $T = 500$ °K for the $EMI^+BF_4^-$ system are presented in Figure 3.3, and show the results we obtained with Gromacs 2022.2 and the results from [7]. In this case, Figure 3.3 shows similar data, we did not obtain the same numerical result, but they are very similar, so we obtain the same behavior in which it is observed that the BF_4^- anion has a slightly smaller MSD slope than the EMI^+ cation.

Once again, we digitized the data and obtained something very similar; however, this time we did not achieve the exact quantitative result. Nevertheless, we can observe that the behavior remains the same, where the molecule that diffuses faster is the largest one. An important note is that the reason we did not obtain the same quantitative value is that Gromacs is constantly being optimized, which causes slight differences in the results. However, the key point is that we observe the same behavior.

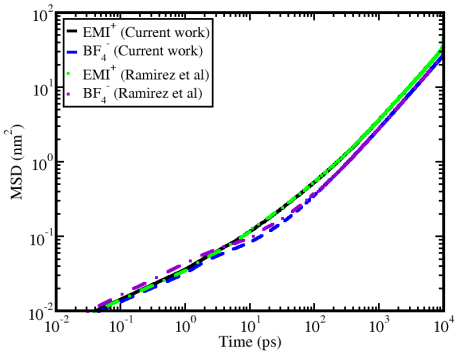

Figure 3.3: The current results for MSD at 500 K compared with the results from Ramirez et al., [7]

In Fig. 3.4 shows the MSD results obtained from the MD simulation. We have chosen three representative temperatures, i.e., T=700, 500, and 300 K for all systems, to illustrate key concepts. The solid lines are for cations, and the dashed lines are for anions.

In the diffusive regime (at large times), interactions become dominant, leading to a slower diffusion of BF_4 compared to EMI^+. Regardless of temperature, the cation consistently exhibits faster diffusion.

In addition, it was also shown that the slope decreases as the temperature decreases.

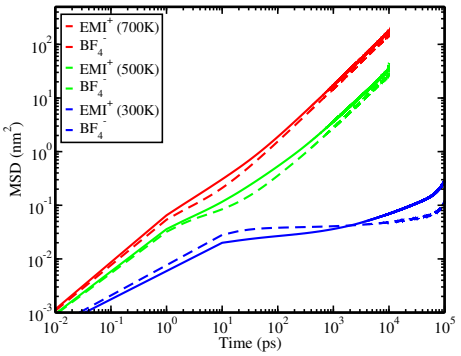

Figure 3.4: The MSD of EMI^+ BF_4 is evaluated at three different temperatures: $T = 700$, 500, and 300 K. Solid lines represent cations, whereas dashed lines correspond to anions.

As mentioned previously, NPT conditions ensure homogeneous states which are similar to reference results. Fig. 3.5(a) shows representative configurations obtained by our results, and Ramirez-Gonzalez [5] Fig. 3.5(b) for EMI-BF_4 IL.

In Figures 3.5(a), and 3.5(b) we observe the comparisons of the final structures of the production run, where we can see that we obtain very similar results to those obtained previously [5]. The Figure 3.5(a) shows the results we obtained with the gromacs 2022.2 version and the Figure 3.5(b) shows what was obtained by Ramírez-González et al [5].

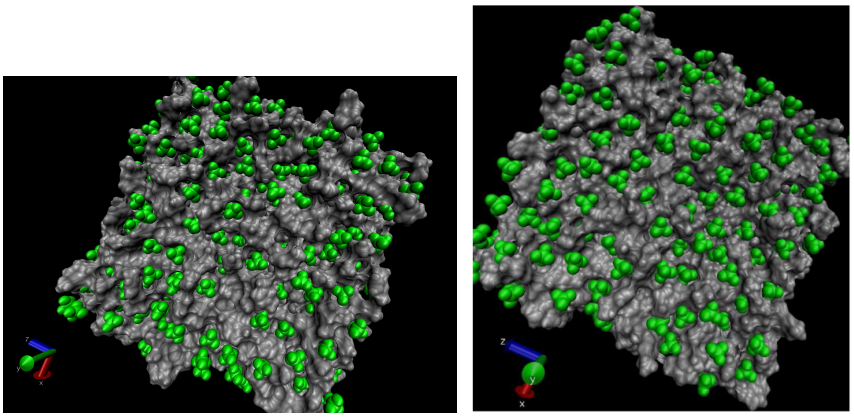

(a) Current results with Gromacs 2022.2. (b) Results from 2016.

Figure 3.5: Comparisons of the final structure obtained with gromacs 2022.2 on the left side and final structure of 2016 on the right side.

Since we obtained the expected results we are ready to carry out the simulations of the other systems, carrying out the correct procedure, for later analyze the structural and dynamical properties of the other systems.

It is worth mentioning that for systems $EMI^+BF_4^-$ and $BMI^+BF_4^-$ the production runs were 10 ns while for the systems $HMI^+BF_4^-$, $OMI^+BF_4^-$, and $DMI^+BF_4^-$ the production runs were 100 ns since the chains are longer and we want to obtain reliable results for dynamical properties.

3.1.2 $BMI^+BF_4^-$

In this section we are going to show the results for the system BMI^+ BF_4^-. An schematic representation of this system, and size is shown in Figure 3.6.

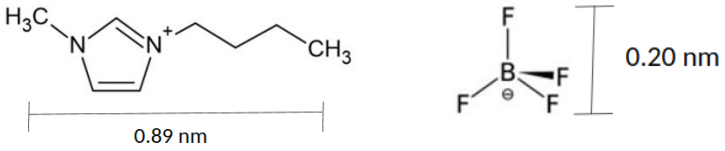

(a) BMI^+. (b) BF_4^-.

Figure 3.6: Schematic representations of the sizes of the ions studied by MD simulation.

Radial Distribution Function

The RDFs of anions and cations around their center of mass are calculated to examine the structural correlations between the ions. The figure 3.8 shows the RDFs between the cation-cation, anion-anion, and cation-anion at 500 °K. The observed well-defined patterns and distinct oscillations indicate the presence of spatial correlations between these species. The first peak of the cation-cation is located at $r = 0.78$ nm, while for anion-anion is at $r = 0.74$ and cation-anion is at $r = 0.48$. As in the system $EMI^+BF_4^-$ we can note that the first peak of anion-anion is more than three times larger than σ_a, and once again we can see the behavior of a Wigner glass.

Figure 3.8 presents the RDFs for three temperatures: $T = 300$ K (blue), $T = 500$ K (green), and $T = 700$ K (red). The dashed, dashed-dotted, and solid lines correspond to $g_{+-}(r)$ ($BMI^+BF_4^-$), $g_{++}(r)$ (BMI^+BMI^+), and $g_{--}(r)$ ($BF_4^-BF_4^-$), respectively. The peak of $g_{++}(r)$ remains at $r = 0.76$ nm, while $g_{+-}(r)$ is positioned around 0.5 nm, both exhibiting weak temperature dependence. In contrast, the peak of $g_{--}(r)$ decreases from 0.78 nm to 0.65 nm as temperature decreases. This behavior closely resembles that of the EMI^+BF_4 system. Additionally, the cation-anion interaction is notably stronger than in the EMI^+BF_4 system.

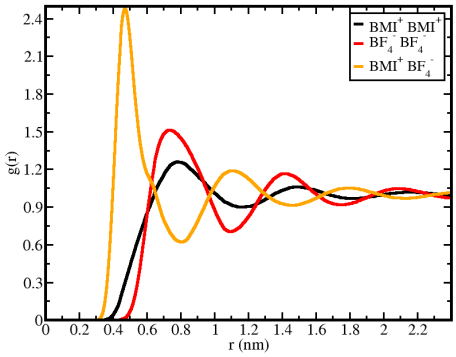

Figure 3.7: Radial distribution functions for the system $BMI^{+}BF_{4}^{-}$ at $P = 1$ atm, and $T = 500K$.

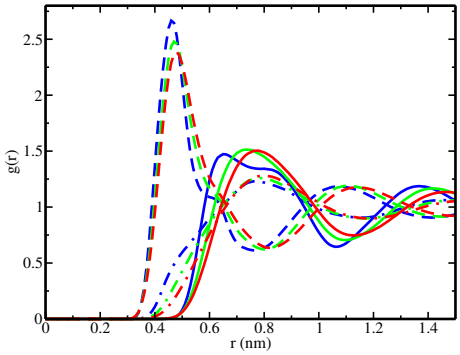

Figure 3.8: Radial distribution funtions for $BMI^{+}BF_{4}^{-}$. The dashed, dashed dotted, and solid lines represent $BMI^{+}BF_{4}^{-}$, $BMI^{+}BMI^{+}$, and $BF_{4}^{-}BF_{4}^{-}$ respectively. We have plotted three representative temperatures, i.e., T=300°K (blue), T=500°K (green), and T=700°K (red).

Mean Squared Displacement

In the figure 3.10 we can see that the same behavior is still maintained where the cation is the one that moves faster than the anion, which is what is observed in the $EMI^{+}BF_4^{-}$ system at 500 °K.

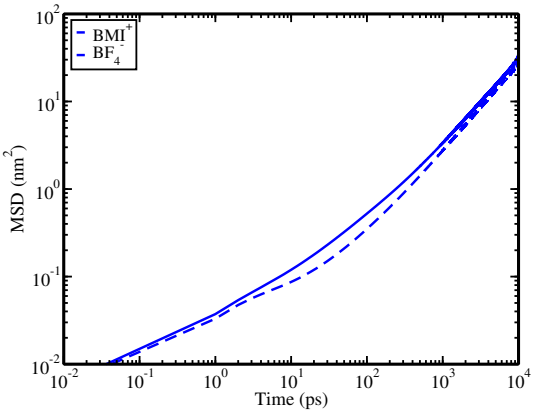

Figure 3.9: Mean Squared Displacement at 500 °K and 10 ns. The solid line is the cation and the dashed line is the anion.

In Fig. 3.10 shows the three representative chosen temperatures, and we can observe as in the EMI^{+} BF_4 system that at large times, the interactions dominate, and the diffusion of BF_4 becomes slower than that of BMI^{+}. And once again, regardless of the temperature, the cation is always the one that diffuses faster. The solid lines are for cations, and the dashed lines are for anions.

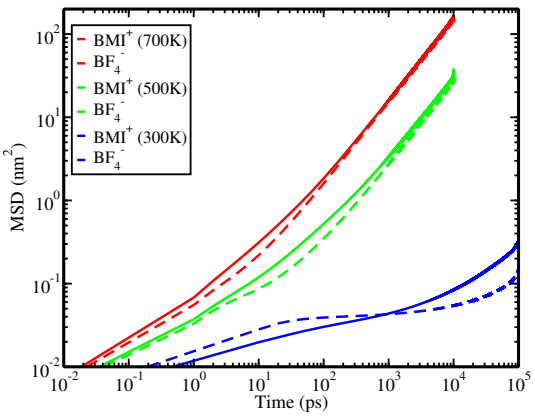

Figure 3.10: The MSD of BMI^{+} BF_4 is evaluated at three different temperatures: $T = 700$, 500, and 300 K. Solid lines represent cations, whereas dashed lines correspond to anions.

In order to confirm the homogeneity of the system, we show the final structure of the production in Figure 3.11.

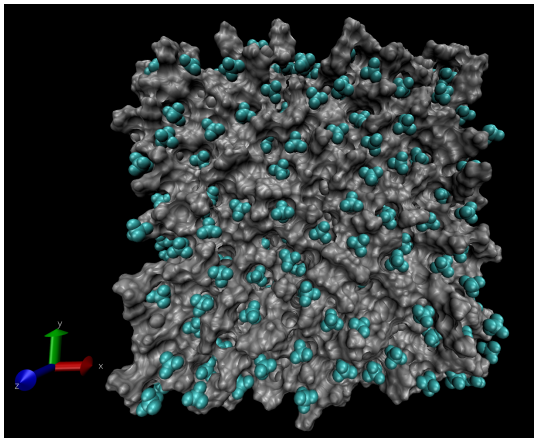

Figure 3.11: Structure of the production at 500 K and 10 ns of the system $BMI^{+}BF_{4}^{-}$.

3.1.3 $HMI^{+}BF_{4}^{-}$

In this section we show the results for the system HMI^{+} BF_4. An schematic representation of this system, and size is shown in Figure 3.12.

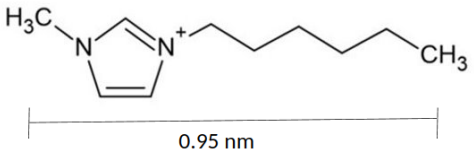

(a) HMI^{+}.

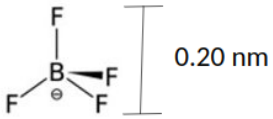

(b) BF_4^{-}.

Figure 3.12: Schematic representations of the sizes of the ions studied by MD simulation.

Radial Distribution Function

The RDFs of anions and cations around their center of mass are calculated to examine the structural correlations between the ions. The figure 3.14 shows the RDFs between the cation-cation,

anion-anion, and cation-anion at 500 °K. We can see well-defined features and distinct oscillations, suggesting the presence of spatial correlations between these species. The first peak of the cation-cation is located at $r = 0.81$ nm, while for anion-anion is at $r = 0.77$ and cation-anion is at $r = 0.46$. As in the last systems $EMI^+BF_4^-$ and $BMI^+BF_4^-$ we can note that the first peak of anion-anion is more than three times larger than σ_a, and once again we can see the behavior of a Wigner glass.

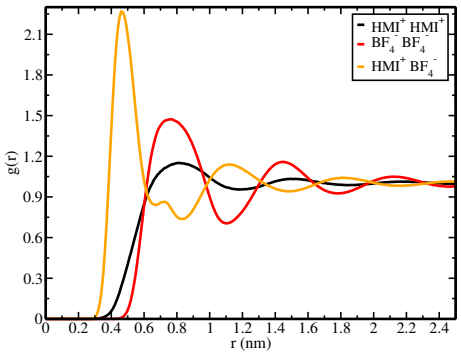

Figure 3.13: Radial distribution functions for the system $HMI^+BF_4^-$ at $P = 1$ atm, and $T = 500K$.

Figure 3.14 displays the RDFs for $T = 300$ K (blue), $T = 500$ K (green), and $T = 700$ K (red). The dashed, dashed-dotted, and solid lines correspond to $g_{+-}(r)$ ($HMI^+BF_4^-$), $g_{++}(r)$ (HMI^+HMI^+), and $g_{--}(r)$ ($BF_4^-BF_4^-$), respectively. The primary peak of $g_{++}(r)$ appears around $r = 0.9$ nm, while $g_{+-}(r)$ is located at approximately 0.5 nm, both remaining largely temperature-independent. Unlike previous systems, the first peak of $g_{--}(r)$ is around 0.8 nm, showing no significant reduction with decreasing temperature. It is evident that in this particular system, the interaction between cations and anions has decreased in comparison to the two previous systems.

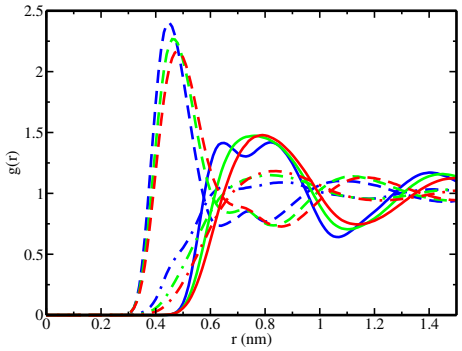

Figure 3.14: Radial distribution funtions for $HMI^+BF_4^-$. The dashed, dashed dotted, and solid lines represent $HMI^+BF_4^-$, HMI^+HMI^+, and $BF_4^-BF_4^-$ respectively. We have plotted three representative temperatures, i.e., T=300°K (blue), T=500°K (green), and T=700°K (red).

Mean Squared Displacement

As we can see in the figure 3.15 for this system it is no longer true that the cation is the one that moves faster than the anion, from this system we begin to see the opposite case. Although in the figure it seems that they are very similar but in reality they are not, the anion moves a little faster than the cation.

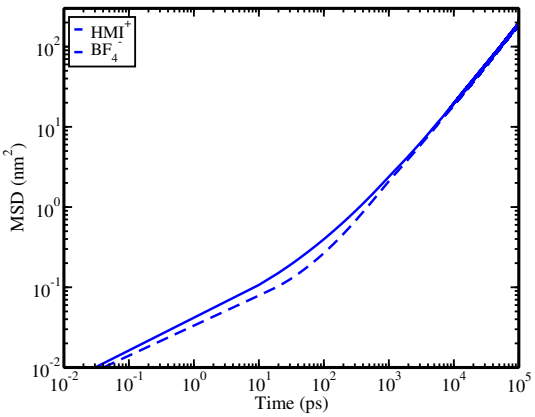

Figure 3.15: Mean Squared Displacement at 500 K and 100 ns. The solid line is the cation and the dashed line is the anion.

In Fig. 3.16 shows the three representative chosen temperatures, and we can observe at large times, the interactions dominate, and the diffusion of HMI^+ becomes slower than that of BF_4^-. What is observed in this plot is that only at low temperatures does the cation diffusion dominate, and as the temperature increases, the anion becomes the faster diffusing species.

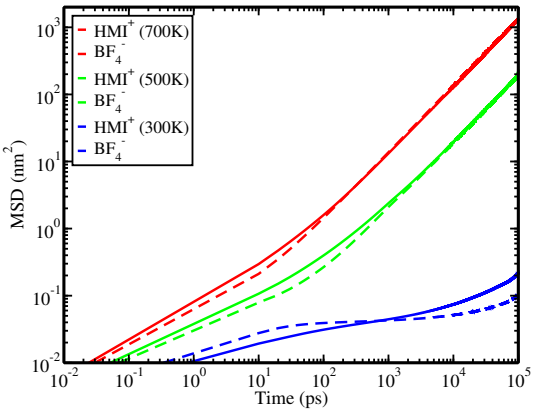

Figure 3.16: The MSD of HMI^+ BF_4 is evaluated at three different temperatures: $T = 700$, 500, and 300 K. Solid lines represent cations, whereas dashed lines correspond to anions.

Figure 3.17 shows the final configuration of the system after the production run, showing that the system remains homogeneous.

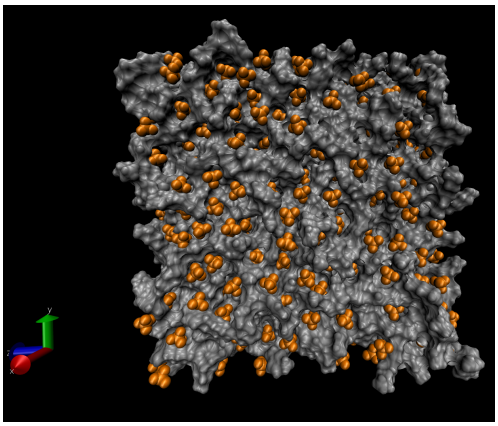

Figure 3.17: Structure of the production at 500 K and 100 ns of the system $HMI^+BF_4^-$.

3.1.4 $OMI^+BF_4^-$

In this section we show the results for the system $OMI^+BF_4^-$. An schematic representation of this system, and size is shown in Figure 3.18.

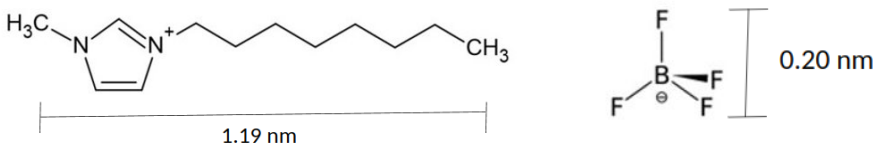

(a) OMI^{+}. (b) BF_4^{-}.

Figure 3.18: Schematic representations of the sizes of the ions studied by MD simulation.

Radial Distribution Function

The RDFs of anions and cations around their center of mass are calculated to examine the structural correlations between the ions. The figure 3.19 shows the RDFs between the cation-cation, anion-anion, and cation-anion at 500 °K. We can see well-defined features and distinct oscillations, suggesting the presence of spatial correlations between these species. The first peak of the cation-cation is located at $r = 0.97$ nm, while for anion-anion is at $r = 0.73$ and cation-anion is at $r = 0.47$. As in the last systems, we continue to observe the same behavior that the first peak of anion-anion is more than three times larger than σ_a, and once again we can see the behavior of a Wigner glass.

In this system, we see that the anions' interaction grows as the tail grows. However on the other hand we have that the interactions between cations decrease as the tails grows.

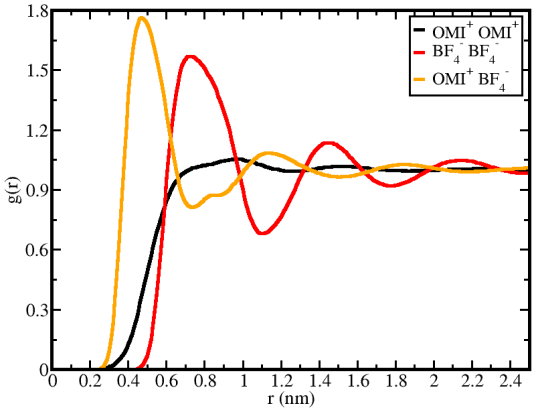

Figure 3.19: Radial distribution functions for the system $OMI^{+}BF_4^{-}$ at $P = 1$ atm, and $T = 500K$.

In Figure 3.20 we show the RDFs for T=300°K (blue), T=500°K (green), and T=700°K (red), where we are using the same notation as the previous systems. In this system we have that the first

peak of g_{++}(r) decreases from 1.43 to 0.91 nm as the temperature increase. For g_{--}(r) we have that the peak decreases from 0.78 to 0.64 as the temperature lowers. The primary peak of $g_{+-}(r)$ is found at approximately 0.5 nm and remains largely unaffected by temperature. As the tail size increases, cation-anion interactions diminish.

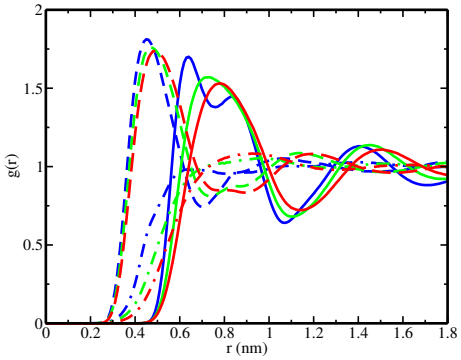

Figure 3.20: Radial distribution funtions for $OMI^+BF_4^-$. The dashed, dashed dotted, and solid lines represent $OMI^+BF_4^-$, OMI^+OMI^+, and $BF_4^-BF_4^-$ respectively. We have plotted three representative temperatures, i.e., T=300°K (blue), T=500°K (green), and T=700°K (red).

Mean Squared Displacement

As we can see in the figure 3.21 for this system it is similar as the $HMI^{+}BF_4^{-}$ system given that the anion is the one that moves faster than the cation, from this system we begin to see the opposite case as in $EMI^{+}BF_4^{-}$ and $BMI^{+}BF_4^{-}$. It is more noticeable visually that the anion diffuses faster than the cation.

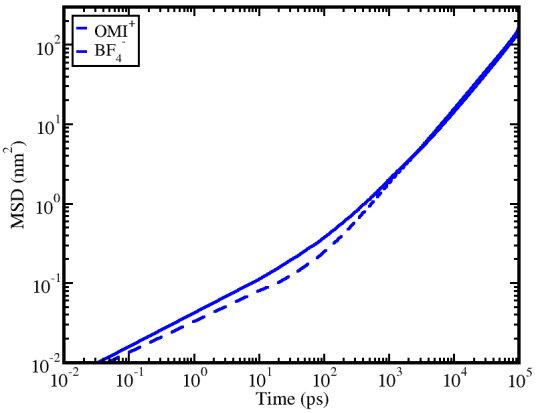

Figure 3.21: Mean Squared Displacement at 500 K and 100 ns. The solid line is the cation and the dashed line is the anion.

In Fig. 3.22 we continue to see that at large times BF_4^{-} moves faster than OMI^{+} as we increase the temperature, we observe that at low temperatures, the cation is the one that diffuses faster.

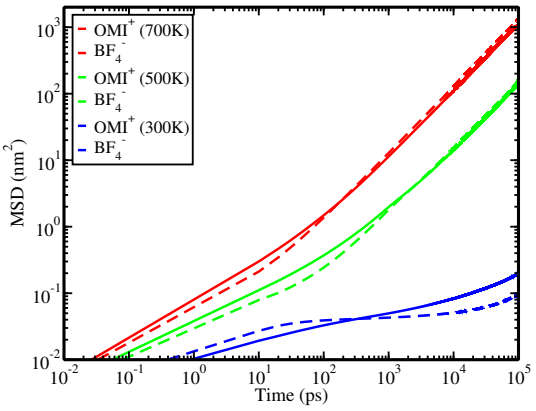

Figure 3.22: The MSD of OMI^{+} BF_4 is evaluated at three different temperatures: $T = 700$, 500, and 300 K. Solid lines represent cations, whereas dashed lines correspond to anions.

Figure 3.23 shows the final configuration of the system after the production run, showing that the system remains homogeneous.

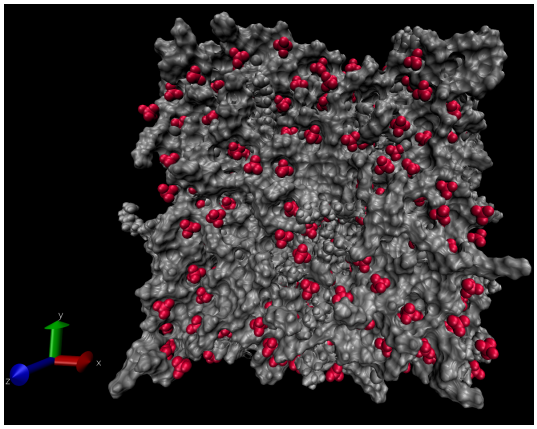

Figure 3.23: Structure of the production at 500 K and 100 ns of the system $OMI^{+}BF_4^{-}$.

3.1.5 $DMI^{+}BF_4^{-}$

In this section we show the results for the system $DMI^{+}BF_4$. An schematic representation of this system, and size is shown in Figure 3.24.

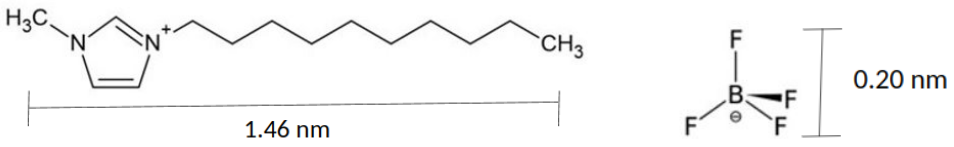

(a) DMI^{+}. (b) BF_4^{-}.

Figure 3.24: Schematic representations of the sizes of the ions studied by MD simulation. Reproduced from [60], with the permission of AIP Publishing.

Radial Distribution Function

The RDFs of anions and cations around their center of mass are calculated to examine the structural correlations between the ions. The figure 3.25 shows the RDFs between the cation-cation,

anion-anion, and cation-anion at 500 °K. We can see well-defined features and distinct oscillations, suggesting the presence of spatial correlations between these species. The first peak of the cation-cation is located at $r = 1.17$ nm, while for anion-anion is at $r = 0.71$ and cation-anion is at $r = 0.52$. As we have been observing in the other systems, we can note that the first peak of anion-anion is more than three times larger than σ_a, and once again we can see the behavior of a Wigner glass, and this is always true regardless of queue size.

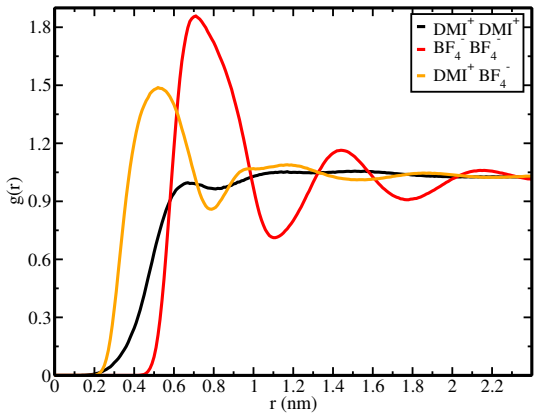

Figure 3.25: Radial distribution functions for the system $DMI^{+}BF_4^{-}$ at $P = 1$ atm, and $T = 500K$.

In Figure 3.26 we show the RDFs for T=300°K (blue), T=500°K (green), and T=700°K (red), where we are using the same notation as the previous systems. In this system we have that the first peak of g_{++}(r) decreases from around 1.15 to 0.58 nm as the temperature decrease. For g_{--}(r) we have that the peak decreases from around 0.77 to 0.64 as the temperature lowers. On the other hand, the first peak of g_{+-}(r) is around 0.5 nm and not depend strongly on the temperature. As we have observed, the longer the chain, the less interaction there is between cations and anions, but the interaction between anions increases.

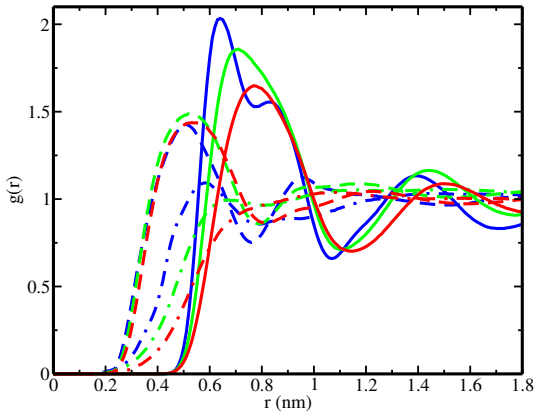

Figure 3.26: Radial distribution funtions for $DMI^+BF_4^-$. The dashed, dashed dotted, and solid lines represent $DMI^+BF_4^-$, DMI^+DMI^+, and $BF_4^-BF_4^-$ respectively. We have plotted three representative temperatures, i.e., T=300°K (blue), T=500°K (green), and T=700°K (red).

Mean Squared Displacement

Once again, as seen in the previous system, it is no longer true that the cation is faster than the anion, in the figure 3.27 it can already be seen that the anion moves faster than the cation.

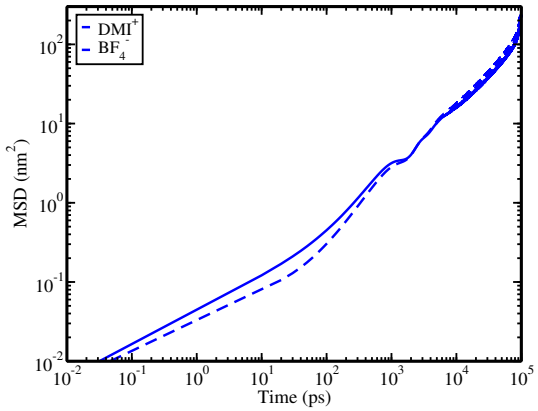

Figure 3.27: Mean Squared Displacement at 500 K and 100 ns. The solid line is the cation and the dashed line is the anion.

In Fig. 3.28 We observe the same behavior that we have been noticing since the HMI^+ system at a temperature of 300 °K the cation is the one that moves faster as we increase the temperature, the diffusion becomes slower, with the roles being reversed, so that the anion now diffuses faster.

Figure 3.29 shows the final configuration of the system after the production run, showing that

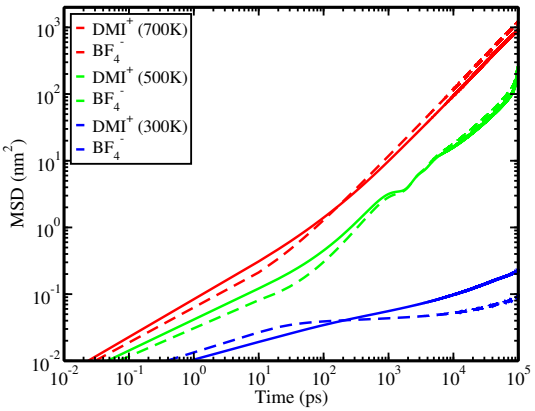

Figure 3.28: The MSD of DMI^+ BF_4 is evaluated at three different temperatures: $T = 700$, 500, and 300 K. Solid lines represent cations, whereas dashed lines correspond to anions.

the system remains homogeneous.

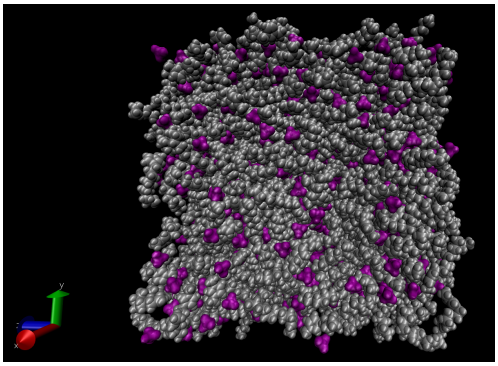

Figure 3.29: Structure of the production at 500 K and 100 ns of the system $DMI^+BF_4^-$.

3.2 Discussion

In this section, we present an analysis of the structural and dynamical properties. Further analysis of different correlation functions can be done in order to obtain a better understanding of the behavior of the systems of interest.

First, we analyze the RDFs of each system at three different temperatures 700°K, 500°K, and 300°K. In the figure 3.30, it is shown how we are representing the head of the cations and the CH_3 group of the tail, which we will refer to as CH_3 to analyze the interactions between them.

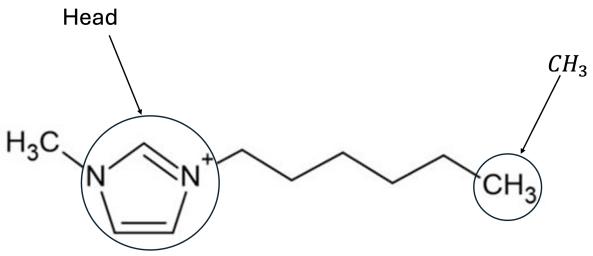

Figure 3.30: Representation that will be used in the following RDFs.

The RDFs of the heads and CH_3 around their center of mass were calculated to analyze the structural correlations. In Figs. 3.31(a), 3.31(b), and 3.31(c), we show the RDFs between the heads of the cations and anions at three different temperatures. As the temperature increases, the RDF's main peak decreases. This occurs because electrostatic interactions are stronger at lower temperatures, where charged particles move more slowly and remain closer. Conversely, at higher temperatures, particles move faster, increasing their separation and weakening these interactions.

This trend is quantitatively captured in the bar chart 3.32, where the height of the bars represents the intensity of the main peak in the RDFs. The decreasing bar height with increasing temperature reflects the weakening head-anion interactions. Additionally, as the tail length increases, the interaction between the cation heads and anions becomes stronger, as seen in both the RDFs and the bar chart, where later systems (OMI^+ and DMI^+) exhibit higher peak intensities.

Figs. 3.33(a), 3.33(b), and 3.33(c) illustrate the interaction between CH_3 (as we show in fig. 3.30) the interaction between the tail and the anions. Here, the interaction is stronger when the cation tail is shorter, decreasing as the tail length increases. These RDFs show that the intensity of the first peak in $g(r)$ decreases as the cation's tail length increases. In other words, the interaction between CH_3 and the anion is stronger for cations with shorter alkyl chains, such as EMI^+BF_4, and progressively weakens for BMI^+BF_4, HMI^+BF_4, OMI^+BF_4, and DMI^+BF_4.

The bar chart 3.34 complements this observation by showing the main peak values of $g(r)$ for each system and temperature. It confirms the trend that the interaction decreases as the cation's chain length increases. Additionally, the peak value decreases with rising temperature, indicating

reduced structuring in the ionic liquid at higher temperatures.

Figures 3.35(a), 3.35(b), and 3.35(c) illustrate the head-to-head interaction at different temperatures (300K, 500K, and 700K). The interaction remains relatively constant across most systems but shows a noticeable increase in the OMI^+ and DMI^+ systems. This trend is further confirmed by the bar chart 3.36, which highlights the rise in the main peak values for these two systems. Additionally, as temperature increases, the intensity of the interaction slightly decreases, indicating a reduction in structural organization at higher temperatures.

Finally, Figures 3.37(a), 3.37(b), and 3.37(c) depict CH_3-CH_3 interactions. As the tail length increases, these interactions become stronger, indicating that the tails preferentially aggregate with other tails while the cation heads interact with each other. This self-segregation into head and tail regions is consistent with the observed trends in both the RDFs and the bar chart 3.38, reinforcing the structural organization of ionic liquids across different temperatures and cation chain lengths.

To provide a clearer visualization of the behavior of the peaks in the radial distribution function at different temperatures, a QR code has been included 3.39. By scanning it, you can access an interactive representation of the peaks at three distinct temperatures, allowing for a more intuitive understanding of their variations.

This is due to several factors, and one of the key factors is the size of the tail (alkyl group or long chain) that is part of the imidazolium base molecule structure. As the size of the tail increases, the interaction between the head and the anion tends to become stronger due to electrostatic and structural effects. Hence, summarizing previous results [19,27, 28] and our own observations, let us break down these factors [22, 30, 31].

3.2.1 Electrostatic shielding and proximity effects

The head of the cation contains a charged group that interacts electrostatically with anions. The size of the tail (alkyl group) can significantly influence the spatial distribution of the molecule.

- Increase in tail size: As the tail size increases, a larger spatial separation is created between the charged group at the head of the molecule and the surrounding environment. This can reduce the electrostatic shielding between the head and the rest of the molecule, allowing the electrostatic interaction between the head and the anion to be more effective. In other words, less shielding from the rest of the molecule and other groups causes the charge on the head to be more strongly felt by the anion.

- Larger tail = stronger interaction: A larger tail can create a ”bubble” around the head, which partially isolates the charged group, allowing the electrostatic interaction between the head and the anion to be stronger because the tail is separated and does not compete as directly with the charge on the head.

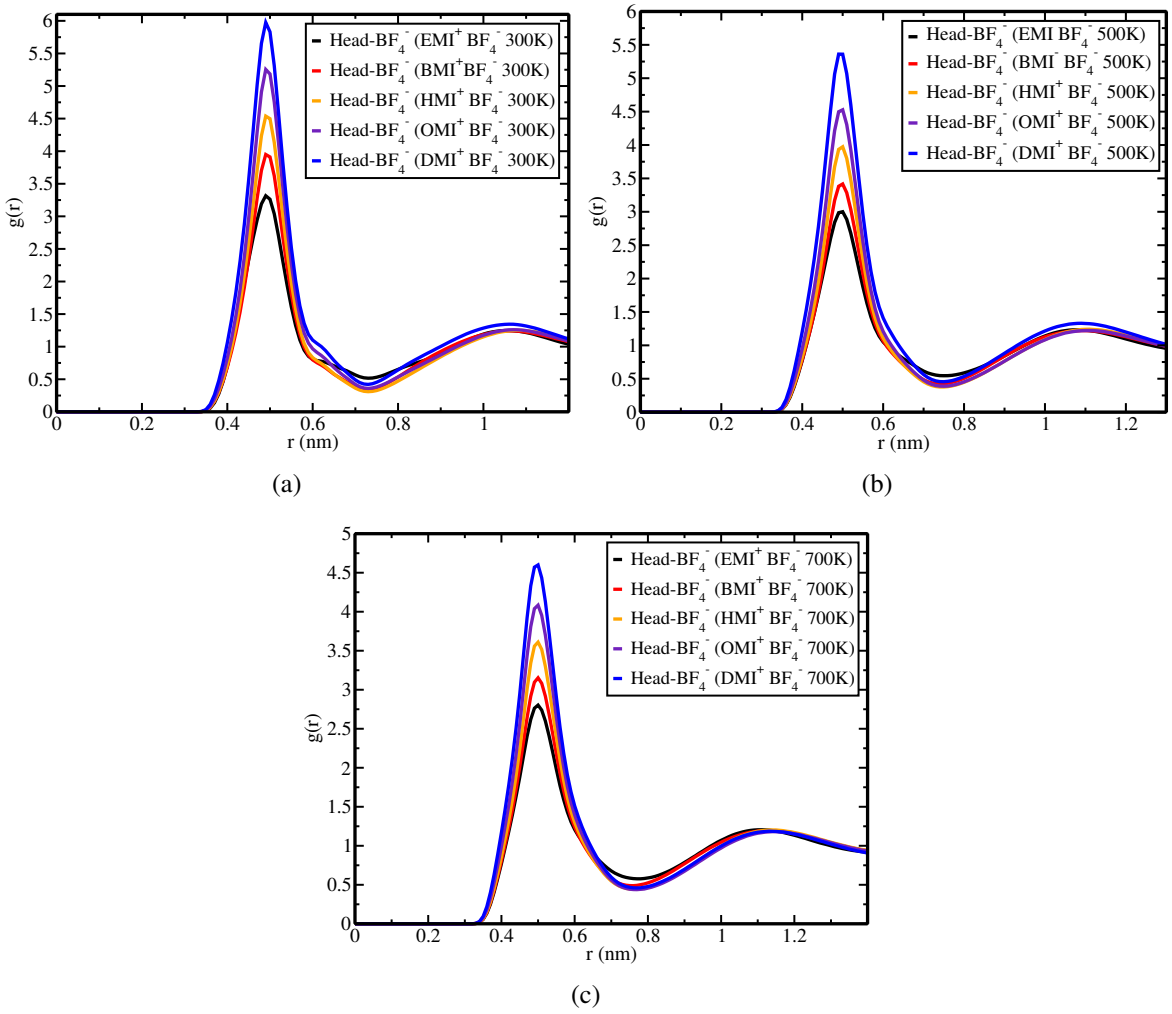

Figure 3.31: Radial distribution functions between heads of the cations and anions at different temperatures T = 300 K, 500 K, and 700 K.

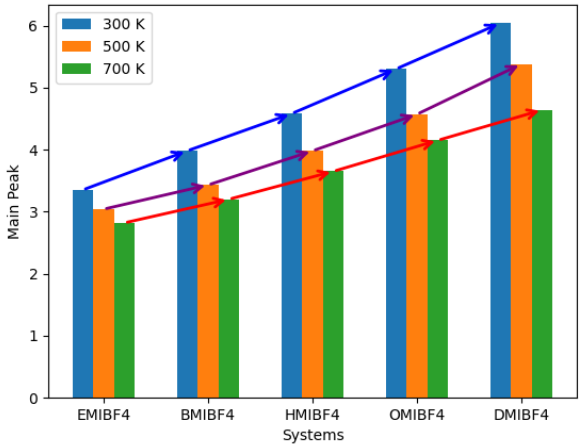

Figure 3.32: Bar chart representing the main peak values of the radial distribution functions $g(r)$ between heads and anions at different temperatures T = 300 K, 500 K, and 700 K. Higher bars indicate an increased number of head-anion pairs in each system, with arrows highlighting the trend across the different ionic liquid systems.

3.2.2 Effect of alkyl groups or long chains

When the tail of the imidazolium base molecule is formed by a long alkyl group or a long-chain group (e.g., a methyl, ethyl, butyl group, etc.), the interaction with an anion is modified as follows:

- Hydrophobic interaction: Long alkyl groups are often hydrophobic, meaning they interact more weakly with the aqueous medium. These hydrophobic interactions can promote the aggregation of imidazolium-based molecules in an aqueous environment, forming clusters or ordered structures that, in turn, can enhance the interaction of the head with anions.

- Greater efficiency in the formation of ionic structures: Longer tail groups can induce a more stable and ordered arrangement among the imidazolium base molecules in solution, promoting the formation of more stable ionic aggregates, which strengthens the interaction between the head and the anion.

3.2.3 Effects of solvation

- Longer tails = lower solvation: In solution, the solvation of molecules plays an important role. Since the tails are long and nonpolar (e.g., hydrocarbon chains), the chains start to associate, expelling the anions to regions with a polar environment. This can result in the charged

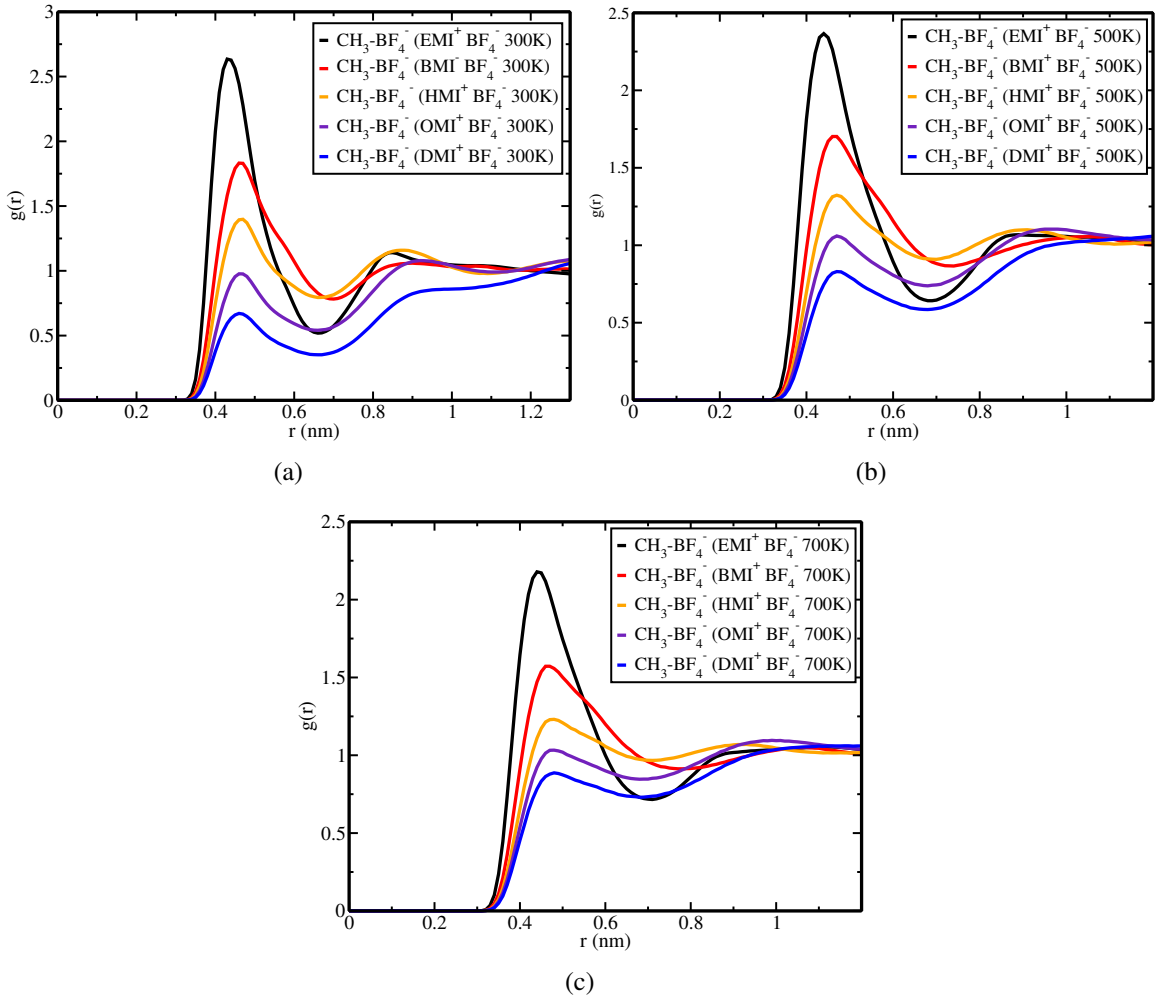

Figure 3.33: Radial distribution functions between CH_3 and anions at different temperatures T = 300 K, 500 K, and 700 K.

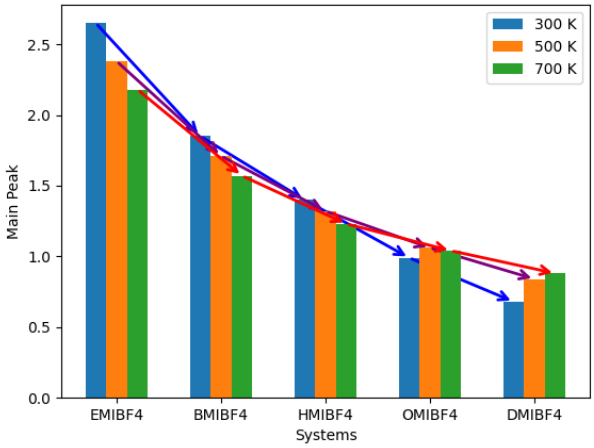

Figure 3.34: Bar chart representing the main peak values of the radial distribution functions $g(r)$ between CH_3 and anions at different temperatures T = 300 K, 500 K, and 700 K. The arrows indicate the trend across the different ionic liquid systems.

imidazolium head being more exposed to the anions, thereby increasing the electrostatic interaction.

- More local interactions: The longer the tail, the greater the distance between the head and other charged groups or solvate molecules, which can lead to more localized and effective interactions with anions.

3.2.4 Mobility and packing effects

- Lower flexibility and higher packing: Long tails can induce denser packing or greater organization in the solution, which restricts the mobility of the molecules and promotes more stable interactions between the heads and the anions.
- Greater interaction capacity: A larger tail size can lead to greater structural stability in ionic liquid solutions or ionic solvents, where the ordered arrangement of the molecules can promote stronger and more lasting interactions with anions.

In conclusion, the interaction of the head with an anion tends to be stronger as the tail size of the molecule increases due to several factors:

- Less electrostatic shielding of the charged head by the rest of the molecule, allowing for a more effective interaction with the anion.

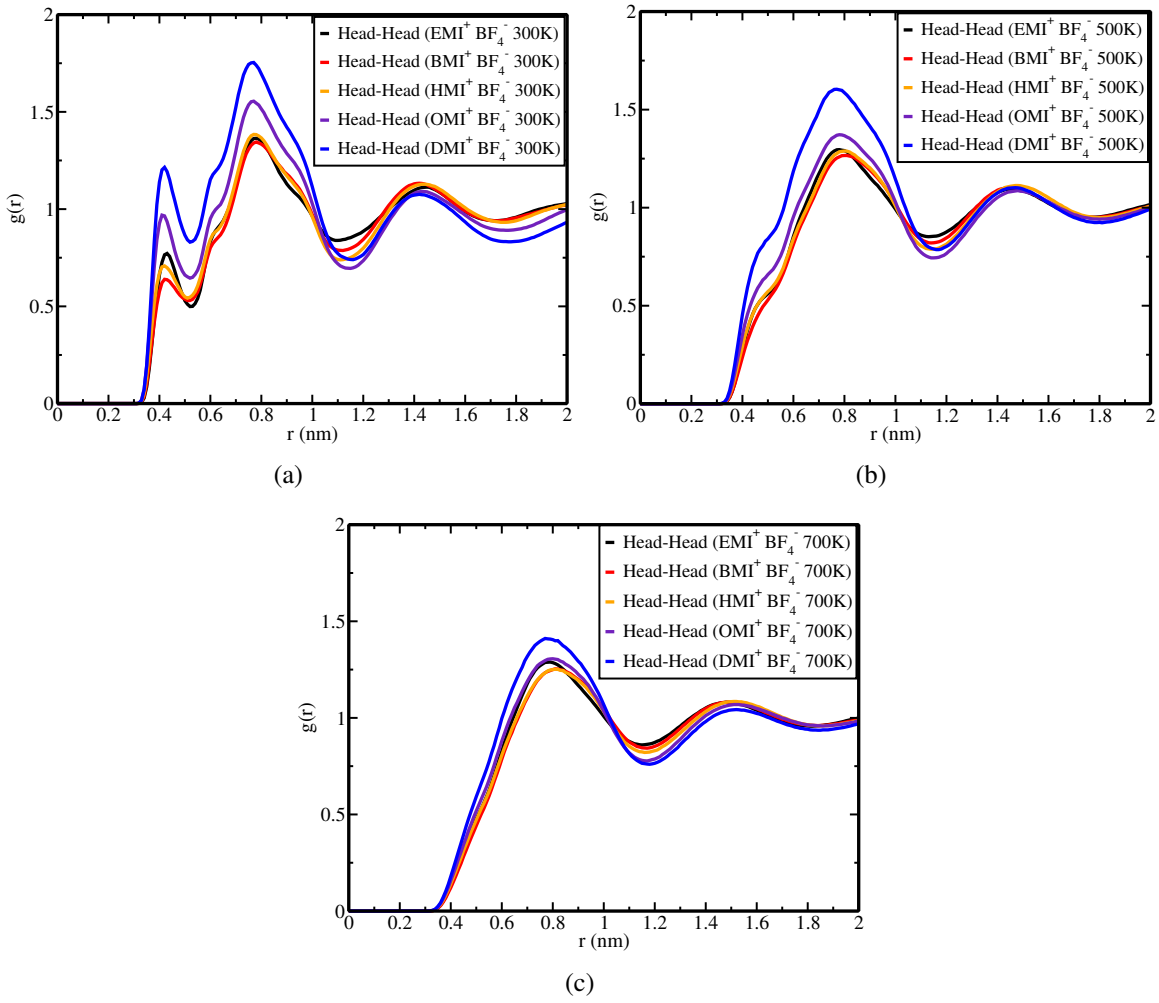

Figure 3.35: Radial distribution functions between head and head at different temperatures T = 300 K, 500 K, and 700 K.

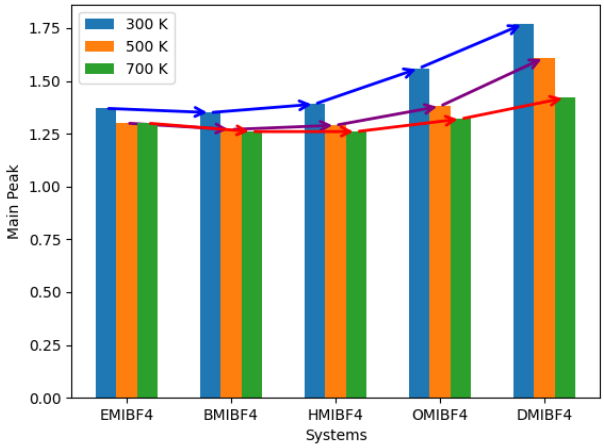

Figure 3.36: Bar chart representing the main peak values of the radial distribution functions $g(r)$ between head and head at different temperatures T = 300 K, 500 K, and 700 K. The arrows indicate the trend across the different ionic liquid systems.

- Greater spatial separation between the charged head and the alkyl groups favors the ionic interaction.
- Hydrophobic effects and structural organization in solutions, increase the efficiency of the ionic interaction.
- Lower solvation of long tails, which makes the charged head more exposed and, therefore, able to interact more strongly with the anions.

Together, a larger tail size enhances the effectiveness of the electrostatic interactions between the head and the anions, resulting in a stronger interaction.

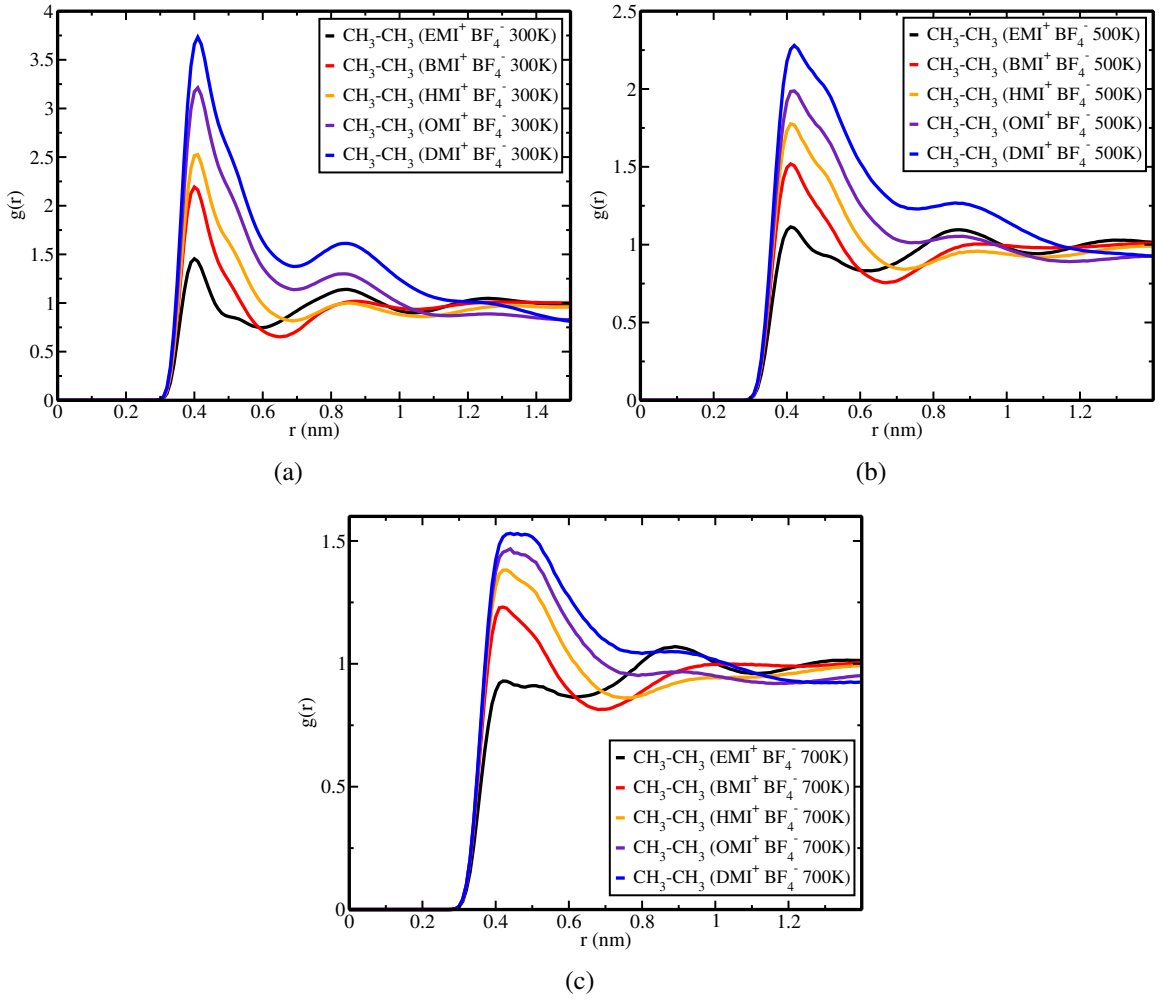

Figure 3.37: Radial distribution functions between CH_3 and CH_3 at different temperatures T = 300 K, 500 K, and 700 K.

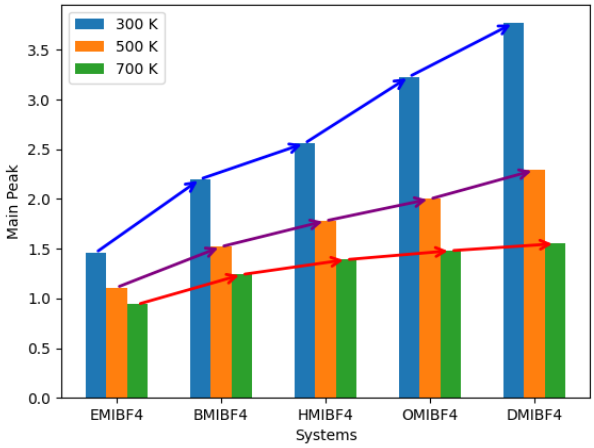

Figure 3.38: Bar chart representing the main peak values of the radial distribution functions $g(r)$ between CH_3 and CH_3 at different temperatures T = 300 K, 500 K, and 700 K. The arrows indicate the trend across the different ionic liquid systems.

Figure 3.39: QR code to visualize the behavior of the peaks in the radial distribution functions at three different temperatures.

3.3 Diffusion coefficient as function of the temperature

The equilibrated sample underwent temperature variations from 700 K to 300 K in steps of $\Delta T = 50$ K. Simulations lasted 10 ns (10,000 configurations) for short chains ($EMI^+BF_4^-$ and $BMI^+BF_4^-$) and 100 ns (100,000 configurations) for long chains ($HMI^+BF_4^-$ and $DMI^+BF_4^-$). For temperatures below 350 K, 100 ns simulations ensured reliable results for long-chain systems.

In order to obtain qualitative comparisons between theory and simulations, we need to calculate the diffusion coefficient as a function of temperature. With the aim of standardize the main state variables, we use definition of dimensionless variables related with thermodynamic quantities, namely, temperature $T^* \equiv k_B T \sigma_{bs} \epsilon_0 / e^2$, $\sigma_{bs} \equiv (\sigma_{big} + \sigma_{small})/2$, where σ_α is the diameter of the corresponding ion, the total volume fraction is given by $\phi \equiv \frac{\pi}{6}(n_{big}\sigma_{big}^3 + n_{small}\sigma_{small}^3)$. In all definitions, ϵ_0 represents the vacuum permittivity, k_B the Boltzmann constant, e the electron charge, and n_α denotes the number density of particles of type α, and isobaric trajectories (P = 1 atm) were used. For future calculations, we will be using a size asymmetry $\delta = \sigma_{big}/\sigma_{small}$ for theoretical calculations.

Table 3.1 shows the mean diameters of the ions and their asymmetry, which will be used in the theoretical calculations. The anion has a tetrahedron structure and a mean size of 0.20 nm, while the cations EMI^+, BMI^+, HMI^+, OMI^+, and DMI^+ are essentially planar and with a mean size (taken from the methyl's CH_3 group to the CH_3 group at the end of the longest chain) of 0.69 nm, 0.89 nm, 0.95 nm, 1.19, and 1.46 nm respectively.

System	σ_{big} (nm)	σ_{small} (nm)	δ
EMI^+ BF_4^-	0.69	0.20	3.5
BMI^+ BF_4^-	0.89	0.20	4.5
HMI^+ BF_4^-	0.95	0.20	4.8
OMI^+ BF_4^-	1.19	0.20	6.0
DMI^+ BF_4^-	1.46	0.20	7.3

Table 3.1: Diameters of each ion in each system, and the size asymmetry for each system.

Table 3.2 shows the equivalence of dimensionless variables with common values of state variables. Such equivalent values were used in Fig. 3.40.

In Fig. 3.40, we can see a continuous decay of the diffusion coefficients with the decreasing of the temperature, typically observed in glass-forming liquids. Such results are exactly the raw data that allow the comparison with theoretical predictions of the PM-SCGLE framework about the glassy behavior of highly asymmetric ionic liquids.

T (K)	T* (EMI^+ BF_4^-)	ϕ	T* (BMI^+ BF_4^-)	ϕ	T* (HMI^+ BF_4^-)	ϕ	T* (OMI^+ BF_4^-)	ϕ	T* (DMI^+ BF_4^-)	ϕ
300	0.0006	0.687	0.0008	1.207	0.0008	1.254	0.0009	2.144	0.0012	3.516
350	0.0007	0.662	0.0009	1.159	0.0010	1.216	0.0012	2.076	0.0014	3.401
400	0.0008	0.641	0.0010	1.123	0.0011	1.177	0.0013	2.008	0.0016	3.285
450	0.0010	0.621	0.0011	1.089	0.0012	1.139	0.0015	1.941	0.0018	3.171
500	0.0011	0.596	0.0013	1.050	0.0014	1.072	0.0017	1.822	0.0020	2.252
550	0.0012	0.584	0.0014	1.022	0.0015	1.066	0.0018	1.814	0.0022	2.956
600	0.0013	0.566	0.0016	0.989	0.0016	1.031	0.0020	1.752	0.0024	2.851
650	0.0014	0.548	0.0017	0.957	0.0018	0.996	0.0022	1.690	0.0026	2.747
700	0.0015	0.531	0.0018	0.926	0.0019	0.961	0.0023	1.629	0.0028	2.643

Table 3.2: Reduced temperatures and volume fraction for each system.

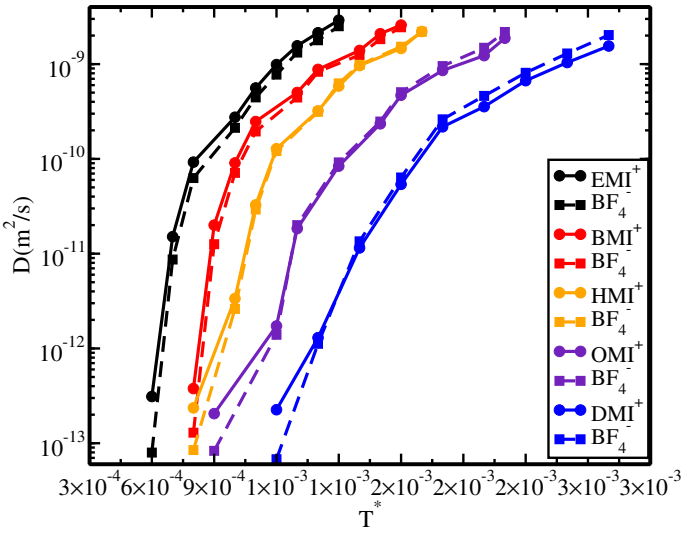

Figure 3.40: Diffusion coefficient as a function of the temperature of each system. Solid lines are for the cations, and the dashed lines are for the anions.

Chapter 4

The PM-SCGLE framework: Predictions and validity limits.

A fluid consisting of s species of charged hard spheres with diameters σ_i and charges q_i ($i = 1, 2, ..., s$), present at concentrations n_i, within a uniform dielectric medium of constant ϵ, constitutes the Primitive Model (PM) of ionic liquids [31]. This model effectively captures the behavior of diverse systems, including electrolytes, macromolecules, micellar solutions, colloidal dispersions, molten salts, and classical plasmas. The competition between hard-sphere and Coulomb interactions results in universal properties, ranging from hard-sphere behavior at high temperatures to purely electrostatic, Debye–Hückel-like behavior under small volume fractions and weak electrostatic coupling. At high interaction strengths (large volume fractions or low temperatures), the system exhibits condensed equilibrium phases such as crystalline solids and molten salts [6]. Additionally, non-equilibrium arrested states like ionic glasses and electrostatic gels can emerge. This study demonstrates that such states arise purely from electrostatic interactions within the PM framework.

The study of dynamically arrested states is a crucial challenge in modern statistical physics and materials science [45, 46, 47]. The mode coupling theory (MCT) [47] is a leading theoretical approach with high predictive power, successfully describing phenomena such as the reentrant glass transition in colloidal suspensions [48, 49]. Similar behavior has been experimentally observed in bicomponent colloidal dispersions with non-adsorbing polymers [50]. However, the bicomponent MCT model failed to predict this reentrant transition [51]. In contrast, the self-consistent generalized Langevin equation (SCGLE) theory [52] provides a satisfactory explanation [53], predicting dynamic arrest scenarios in electroneutral mixtures of charged particles.

Previously, both SCGLE and MCT theories have been applied to the PM of molten salts, enabling first-principles descriptions of liquid dynamics and arrest lines, as depicted in Figure 4.1.

Both theories predict partially arrested states with differences in interpretation. MCT identifies

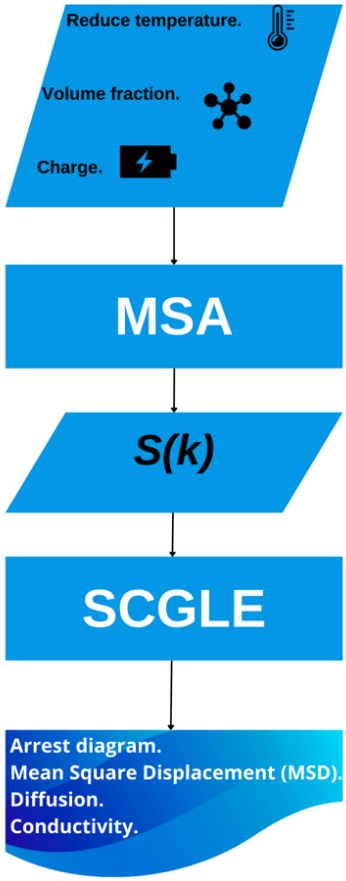

Figure 4.1: The flowchart provides a summary of the SCGLE theory implementation. An analytical solution for the structure factor is derived using specified values of reduced temperature, packing fraction, and charge. These parameters are then input into the SCGLE equations to obtain numerical solutions. The resulting outputs include various relevant dynamical properties [4].

these states via the ergodicity of the self-part of the intermediate scattering function, while SCGLE maintains ergodicity for both collective and self-components of mobile species. Despite these nuances, SCGLE and MCT provide equivalent theoretical frameworks with similar results [54]. For a comprehensive review of these theories, see Janssen [55].

The SCGLE framework requires the equilibrium structure factor, derived analytically from the PM. Using this structural input, SCGLE computes key dynamical properties, including MSD, diffusion coefficients, and dynamic-arrest diagrams.

Various theoretical approximations exist for ionic liquid structures, such as Debye–Hückel limiting laws and mean spherical approximations (MSA, GMSA). This study employs the Hiroike model.

Molecular dynamics simulations have qualitatively confirmed SCGLE predictions for the PM and dipolar hard sphere systems.

SCGLE has been applied to a broad range of systems, accurately predicting thermodynamic and dynamic properties, including MSD and diffusion coefficients of complex materials like molten salts and colloidal Wigner glasses [65, 4, 6].

Systematic theoretical studies of partially arrested states have been made for hard-sphere binary mixtures. The components in the mixtures may be characterized by the volume fractions ϕ_S and ϕ_L of small and large particles, respectively.

4.1 A brief overview of the SCGLE theory

The asymptotic solution of the SCGLE theory is employed to calculate the dynamical arrest diagrams. The dynamic formulation of this theory, applicable to any correlation time t, can be implemented for the same system to provide deeper insights into the Mean Squared Displacement (MSD) behavior of all ionic species involved. Figure 4.1 presents a flowchart outlining the process for applying the theory to compute the arrest line and dynamic properties.

The fundamental structure of the SCGLE theory is described in detail in [4], where analytical expressions are derived for the time-dependent correlation function $F(k,t)$, the self-intermediate scattering function $F_S(k,t)$, and the time-dependent friction function $\Delta\zeta^*_\alpha(t)$.

These three quantities form a system of closed equations, expressed as:

$$F(k,z) = \left\{ zI + k^2 D \cdot [I + \lambda \Delta\zeta^*(t)]^{-1} \cdot S^{-1}(k) \right\}^{-1} \times S(k), \tag{4.1}$$

$$F_S(k,z) = \left\{ zI + k^2 D \cdot [I + \lambda(k) \cdot \Delta\zeta^*(t)]^{-1} \right\}^{-1}, \tag{4.2}$$

$$\Delta\zeta^*_\alpha(t) = \frac{D_0^\alpha}{3(2\pi)^3} \times \int d^3k k^2 \left[F^{(s)(t)} \right]_{\alpha\alpha} \left[c \cdot \sqrt{n} \cdot F(t) \cdot S^{-1} \cdot \sqrt{n} \cdot h \right]_{\alpha\alpha}, \tag{4.3}$$

where $F(z)$ and $F_S(z)$ are matrices with elements $F_{\alpha\beta}(k,z)$ and $F^s_{\alpha\beta}(k,z)$ ($\alpha\beta = 1,2$). These matrix elements correspond to the Laplace transform of the functions $F(k,t)$, and $F_S(k,t)$, with z representing the conjugate variable to t in the Laplace domain. The matrix D has elements given by $D_{\alpha\beta} \equiv \delta_{\alpha\beta} D_0^\alpha$ where D_0^α is the short-time diffusion coefficient of species α, assuming hydrodynamic interactions are neglected. This coefficient is related to the solvent friction coefficient ζ_0 of an isolated particle of species α via the Einstein relation $D_0^\alpha \equiv k_B T/\zeta_0^\alpha$. A detailed derivation of Eqs. (4.1)-(4.3) can be found in [4]. As previously mentioned, the SCGLE theory emerges as a solution to the exact generalized Langevin equation, using a Vineyard-like approximation that links the self-memory function from the Langevin equation to the collective memory function (first-order approximation), thus generating a closed set of self-consistent equations that only require a static property as input.

To analyze the mobility of molecular species within the SCGLE framework, we establish a correlation between the MSD and the time-dependent correlation functions. The MSD is defined as:

$$MSD(\tau) \equiv \left\langle (\mathbf{r}(0) - \mathbf{r}(\tau))^2 \right\rangle, \tag{4.4}$$

where $\mathbf{r}(\tau)$ denotes the position of a given particle at correlation time τ, and the average is computed over all possible particle trajectories. This quantity describes the deviation of a particle's position from its initial location. The long-time self-diffusion coefficient is then defined as the rate of change of the MSD with respect to correlation time:

$$D(\tau) \equiv \frac{1}{6} \frac{d \left\langle (\mathbf{r}(0) - \mathbf{r}(\tau))^2 \right\rangle}{d\tau}. \tag{4.5}$$

The SCGLE equations were numerically solved to determine the MSD of both ionic species for a given total volume fraction.

The long-time self-diffusion coefficient D_L^α represents the limiting case at long diffusion times. Assuming. $\tau \gg \tau'$, it is given by:

$$\begin{aligned} D_L^\alpha &\equiv \lim_{\tau\to\infty} D^\alpha(\tau) \\ &= 1 - \lim_{\tau\to\infty} \int_0^\tau D^\alpha(\tau') \Delta\zeta_\alpha^*(\tau - \tau') d\tau' \\ &= 1 - D_L^\alpha \lim_{\tau\to\infty} \int_0^\tau \Delta\zeta_\alpha^*(u) du, \end{aligned} \tag{4.6}$$

which simplifies to:

$$D_L^\alpha = \frac{1}{1 + \int_0^\infty \Delta\zeta_\alpha^*(\tau') d\tau'}. \tag{4.7}$$

The quantities D_L^α and D^α are expressed in terms of their respective short-time diffusion coefficients D_0^α.

The structure factor serves as the key input for the arrest criteria within the SCGLE formalism. The asymptotic solution, $\gamma_\alpha \equiv \lim_{t\to\infty} \langle(\mathbf{r}(0) - \mathbf{r}(\tau)^2)\rangle$, is given by:

$$\frac{1}{\gamma_\alpha} = \frac{1}{3(2\pi)^3} \int d^3k k^2 \left\{\lambda[\lambda + k^2\gamma]^{-1}\right\}_{\alpha\alpha} \left\{c\sqrt{n}\lambda S[\lambda S + k^2\gamma]^{-1}\sqrt{n}h\right\}_{\alpha\alpha}, \tag{4.8}$$

where $\lambda(k)$ is a diagonal matrix elements $\lambda_{ij} \equiv \delta_{ij}\left[1 + \left(\frac{k}{k_c}\right)^2\right]^{-1}$, and $k_c = 2\pi\frac{1.305}{\sigma_\alpha}$ is an interpolation parameter used to match results for hard spheres in the Baxter approximation.

The parameter γ in Eq. 4.8 corresponds to a unique value for each combination of thermodynamic properties (ϕ, T^*). When $\gamma_\alpha \to \infty$, the system remains in an ergodic fluid state. However, finite values $\gamma_\alpha < 1$ indicate arrested states, where particle mobility is lost. A partially arrested state implies that one species has become immobile ($\frac{1}{\gamma} \neq 0$), while the other remains diffusive ($\frac{1}{\gamma} = 0$).

For a precise comparison between simulations and theoretical predictions, we employed non-dimensional variables. The length unit used is the ionic diameter σ_p, while the time unit is the Brownian time, defined as $\frac{\sigma_p^2}{D_0}$. Other reduced variables are:

$$\sigma_{pm} \equiv \frac{\sigma_p + \sigma_m}{2}, \tag{4.9}$$

$$P^* \equiv P\epsilon_0\frac{\sigma_{pm}^4}{e^2} \quad \text{reduced pressure}, \tag{4.10}$$

$$T^* \equiv k_B T\frac{\sigma_{pm}\epsilon_0}{e^2} \quad \text{reduced temperature}, \tag{4.11}$$

$$\phi \equiv \pi\frac{n_p\sigma_p^3 + n_m\sigma_m^3}{6} \quad \text{total volume fraction}, \tag{4.12}$$

where the subindex p refers to the positively charged ionic species, or cations, and the subindex m refers to the negatively charged ionic species, or anions. The ϵ_0 represents the vacuum permittivity, k_B is the Boltzmann constant, e is the electron charge, and n_α corresponds to the number density of the α particles. In our theoretical calculations, we have chosen size and charge asymmetries, represented by $\delta = \frac{\sigma_p}{\sigma_m}$ and $\varepsilon = |\frac{q_p}{q_m}|$, respectively. Due to charge neutrality $(n_p q_p + n_m q_m = 0)$, the macroscopic states for a given combination of size δ and charge ε asymmetries of this system can be defined with only two control parameters (in this work, we focus only on size asymmetry), for which we choose the total volume fraction ϕ and the reduced temperature T^*.

4.1.1 Ionic conductivity

In the theory of glass structure, it is widely recognized that ion transport is a process that depends on temperature. However, the electrical conductivity of an ionic conducting glass is influenced by frequency, with the dc conductivity remaining constant as long as the frequency at a given temperature is below a characteristic threshold: $\widehat{\sigma}(\nu)(\nu \to 0) = \sigma_{dc}$ [4].

The electrical conductivity σ and the self-diffusion coefficient D are related in the frequency domain through a generalized Nernst-Einstein equation:

$$\widehat{\sigma}(\nu) = \frac{n_i q_i^2}{k_B T \cdot \widehat{H}_R(\nu)} \widehat{D}(\nu), \tag{4.13}$$

where n_i is the number density, q_i is the charge of the mobile ions, and $\widehat{H}_R(\nu)$ is the frequency-dependent complex Haven ratio, typically defined as the ratio of the tracer diffusion coefficient to the charge diffusion coefficient. The Haven ratio reflects the correlation and collective nature of the microscopic mechanisms of ionic diffusion. It is important to note that the SCGLE theory can be used to explore the intricate relationship between the Haven ratio and collective properties. However, such analysis is complex and can only be simplified through approximations. As demonstrated by Farias-Anguiano et al. [4], a simple approximation is sufficient for good agreement with experimental data. Equation 4.13 can be evaluated for any frequency ν, but for macroscopic systems, the long-time limit when $\nu \to 0$ is more significant, i.e., $\widehat{H}_R(\nu)(\nu \to 0) = H_R$ and $\widehat{D}(\nu)(\nu \to 0) = D$.

Additionally, if the correlations between velocities of different ionic species are ignored, the Haven ratio becomes frequency-independent and equals one:

$$\sigma_{dc} = \frac{n_i q_i^2}{k_B T} D. \tag{4.14}$$

It is crucial to emphasize that this relationship is valid only for the glassy states of our system. However, since these glassy states are within the temperature range of interest, they offer a direct measure of electrical conductivity, provided the self-diffusion coefficient is known.

We can use our solutions to determine the electrical conductivity, $\sigma \approx D_L$ for each ionic species, where D_L is the long-time diffusion coefficient [4]. In the following sections, we will present the results obtained.

4.2 Results

This section presents the main results of the PM-SCGLE framework applied to highly size-asymmetric PM.

To calculate the phase diagram of each system, the dynamic-arrest criterion described in the previous section Eq. 4.8 was used. The parameter γ_i has a unique value for a given combination of temperature, density and size-asymmetry. The input parameters for the PM-SCGLE framework, are the molecular diameters, the total volume fraction, and the reduced temperature. Values of $\gamma \to \infty$ correspond to ergodic fluid states, while finite values of $\gamma < 1$ define glassy arrested states. By fixing the value of ϕ (which defines an isochore) and computing γ_i values for one species within a range of temperatures, it is possible to map the change in values and delimit regions in the phase space that exhibits kinetic arrest of one or both species. The results are shown in Figs. 4.2-4.6 where four distinct regions have been found for changes in values of γ_i for the cation and anion species. In each "phase", the kinetic state (fluid F or glass G) of the cation is listed first and that of the anion is listed second. The lower region corresponds to finite small values of γ_i in both species and is a completely arrested phase. At higher temperatures, adhesive interactions between opposite charges are suppressed, so that in systems that have a low enough volume fraction to avoid jamming both species have fluid-like mobility. More interesting are the regions at the top right (high volume fraction, high temperature) where only one of the ionic species is arrested. The partially-arrested F-G and G-F regions will be the focus of our subsequent analysis.

To collect further insights into the phase transition phenomena being observed, we will select several points in the arrest diagram, following the isobaric trajectories (p = 1 atm) shown as the red dashed lines in Figs. 4.2-4.6, and we will calculate the diffusion coefficient of the two ionic species at each region using the dynamic version of the SCGLE theory these will be shown in the next section.

We can observe from these plots that as the tail length increases, the regions where the mixed states are found become larger, and within regions G-F, the hard-sphere interactions dominate leading to the dynamic arrest of the bigger particles due to caging. If the size difference between species is enough, small particles can diffuse through the holes left by the big particles. On the other hand, in regions F-G, the small particles become arrested due to high electrostatic repulsion between anions, leading to enough space for the diffusion of the cations, a state known as Winger glass. The red lines shown in each figure represent an isobaric trajectory that mimics the cooling process performed in the simulated systems.

In Fig. 4.7, we observe that at low temperatures, electrostatic interactions dominate the system's dynamics, significantly affecting the differential mobility of the ions. In particular, the BF_4^- anion experiences dynamic arrest due to the strong repulsion between anionic species, leading to the formation of low-density regions within the ionic liquid structure. These regions create relatively open pathways that facilitate the movement of the EMI^+ cation.

On the other hand, at high temperatures (Fig. 4.8), the dynamics of the ionic liquid are dominated by hard-sphere interactions, where the excluded volume of each species plays a key role in ionic mobility. In this regime, larger molecules tend to experience dynamic arrest due to steric constraints, which limits their effective mobility. As a consequence, the interstitial spaces created

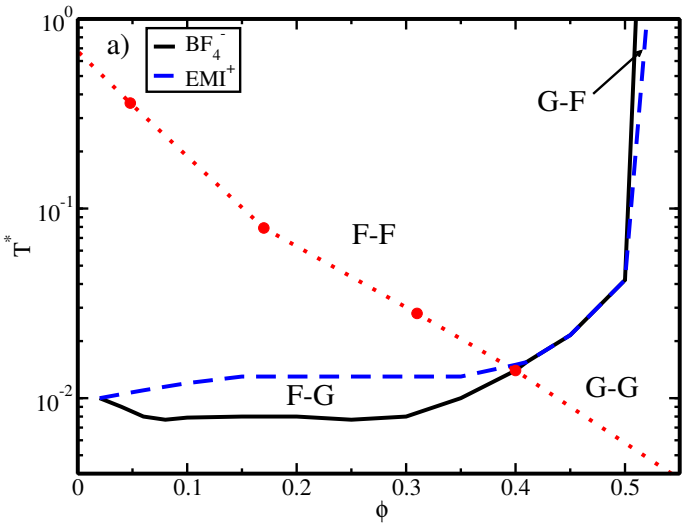

Figure 4.2: Arrest diagram as function of the total packing fraction ϕ_T adn the reduced temperature T^* for the system EMI^+ BF_4^-. Reproduced from [60], with the permission of AIP Publishing.

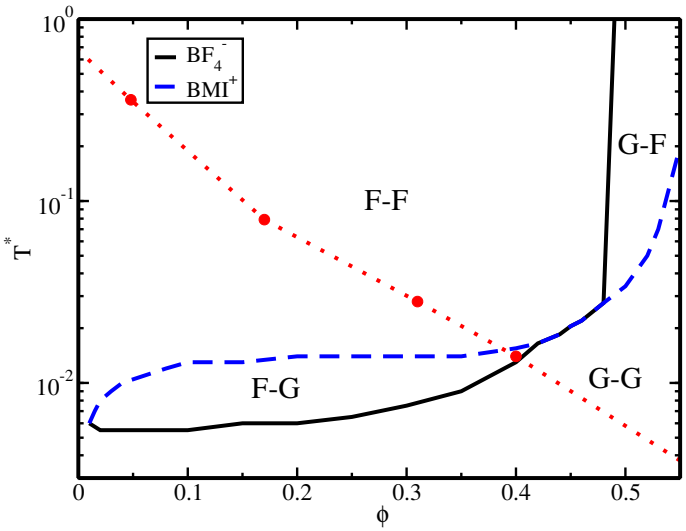

Figure 4.3: Arrest diagram as function of the total packing fraction ϕ_T adn the reduced temperature T^* for the system BMI^+ BF_4^-.

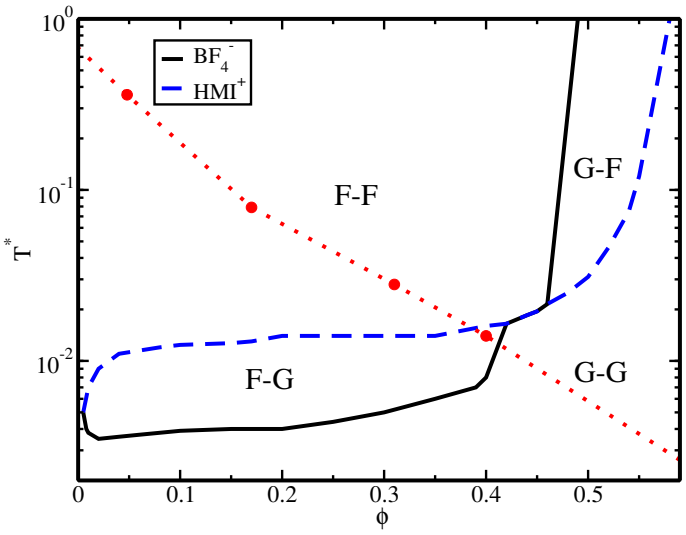

Figure 4.4: Arrest diagram as function of the total packing fraction ϕ_T adn the reduced temperature T^* for the system HMI^+ BF_4^-.

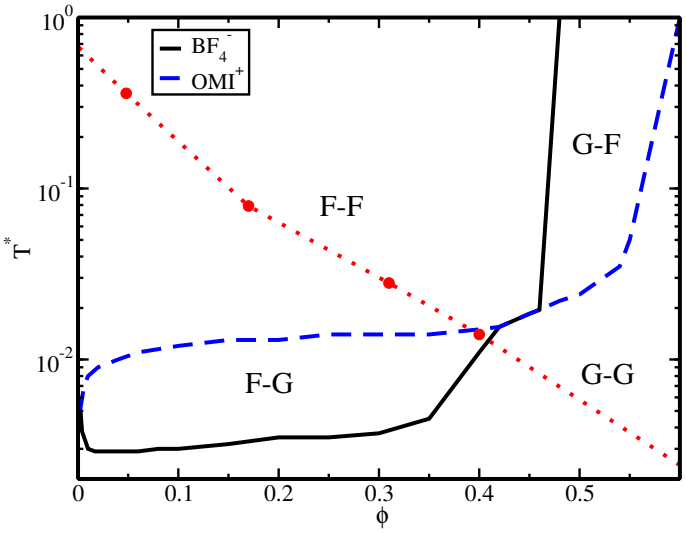

Figure 4.5: Arrest diagram as function of the total packing fraction ϕ_T adn the reduced temperature T^* for the system OMI^+ BF_4^-.

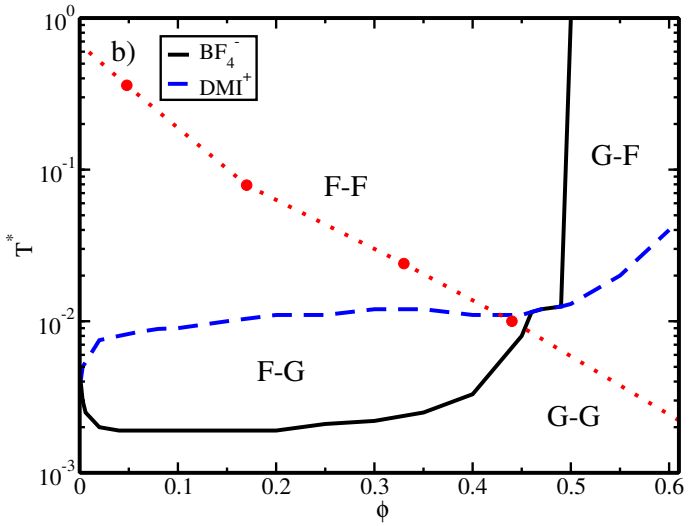

Figure 4.6: Arrest diagram as function of the total packing fraction ϕ_T adn the reduced temperature T^* for the system DMI^+ BF_4^-. Reproduced from [60], with the permission of AIP Publishing.

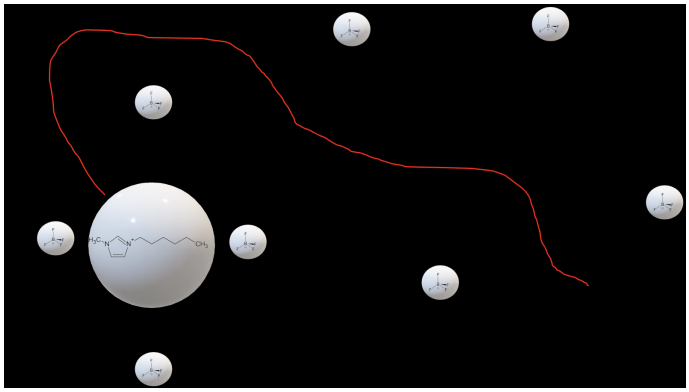

Figure 4.7: Representation of the system at low temperatures, where electrostatic interactions dominate, leading to dynamic arrest of the BF_4^- anion and the formation of low-density regions that facilitate the movement of the EMI^+ cation. The red line in the image indicates that the particle is moving, while the others are arrested.

by the arrangement of these larger species form channels through which smaller ions can diffuse more easily.

This behavior reflects a shift in the transport mechanism compared to low temperatures, where electrostatic interactions predominate. As thermal energy increases, the repulsive forces between anions are reduced in comparison to the geometric and excluded volume effects, leading to a regime where mobility is governed more by spatial constraints than by electrostatic interactions.

Consequently, the differential mobility of ions in the system is influenced by the competition between electrostatic and geometric effects, with the latter dominating at higher temperatures. This shift in the transport regime is a key factor in understanding the viscosity and ionic conductivity of the system as a function of temperature.

As a result, ionic mobility in the system is governed by a mechanism in which the structure imposed by anion–anion interactions constrains cation transport. As temperature increases, thermal energy partially disrupts these interactions, reducing viscosity and promoting a more balanced mobility between both species.

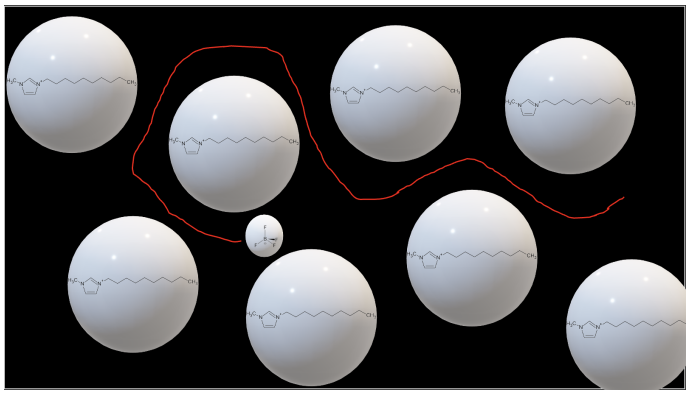

Figure 4.8: Representation of the hard-sphere interaction in ionic liquids at high temperatures. The large cations impose spatial constraints, creating interstitial voids that allow smaller anions to diffuse more freely. The red line in the image indicates that the particle is moving, while the others are arrested.

Chapter 5

Theory vs Simulation

In this chapter, we present a comprehensive comparison between theoretical predictions of the PM-SCGLE framework and the molecular dynamics simulations of model ILs. The main aim is to show if the theoretical scenario is observed in the simulated systems. Additionally, we want to probe the validity limits of the theory. It is important to emphasize that the comparisons made below are qualitative.

The data is interpreted as follows: the main plots display the results from simulations, while the insets show the corresponding theoretical calculations.

Figures 5.1 and 5.2 clearly illustrate the glassy behavior of both cations and anions at low reduced temperatures. This behavior is characterized by a significant decrease in diffusivity as T^* decreases. At very low temperatures, diffusivity drops to extremely small values ($D \sim 0$), ndicating a dramatic reduction in molecular mobility. This trend is consistent with systems approaching a glass transition, where molecular motion becomes increasingly restricted, leading to an amorphous solid-like state. The sharp transition from a diffusive regime at high temperatures to a constrained regime at lower temperatures is a hallmark of glassy dynamics.

The insets further support this interpretation: diffusivity reaches a plateau at high reduced temperatures but becomes nearly negligible as T^* approaches zero. This suggests a well-defined transition in dynamic properties, aligning with both theoretical and experimental expectations for glass-forming systems.

Figures 5.3, 5.4, and 5.5 compare the diffusivity of cations and anions, highlighting their similar qualitative behavior as a function of reduced temperature. Despite minor quantitative differences, the overall trends and curve shapes remain remarkably consistent. At lower temperatures, both species exhibit a steep decline in diffusivity, reflecting the slowdown associated with glassy dynamics. As temperature increases, diffusivity rises sharply before gradually approaching a saturation region at higher temperatures.

This qualitative agreement suggests that both systems share analogous physical mechanisms

governing their dynamics across the examined temperature range. The inset plots reinforce this conclusion, showing overlapping trends on a logarithmic scale. While minor deviations may arise due to differences in molecular interactions or structural properties, the overall behavior remains robustly similar.

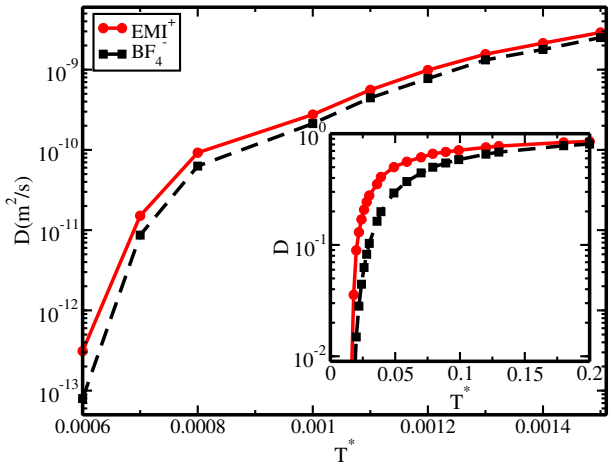

Figure 5.1: Diffusion coefficient versus reduced temperatures for the system EMI^+ BF_4^-. Left panel shows the results obtained using all-atom simulations of systems. The panel at the right contains the theoretical results obtained form the SCGLE theory. Reproduced from [60], with the permission of AIP Publishing.

5.1 Electrical Conductivity and Ion Transport

In addition to diffusivity, we also evaluate the electrical conductivity, which can be approximated as $\sigma \approx D_L$, where D_L is the long-time diffusion coefficient. Figures 5.6 to 5.10 present the logarithm of conductivity multiplied by the reduced temperature as a function of the inverse reduced temperature for various asymmetries:

- $\delta = 3.5$ (Fig. 5.6),
- $\delta = 4.5$ (Fig. 5.7),
- $\delta = 4.8$ (Fig. 5.8),
- $\delta = 6.0$ (Fig. 5.9),
- $\delta = 7.3$ (Fig. 5.10).

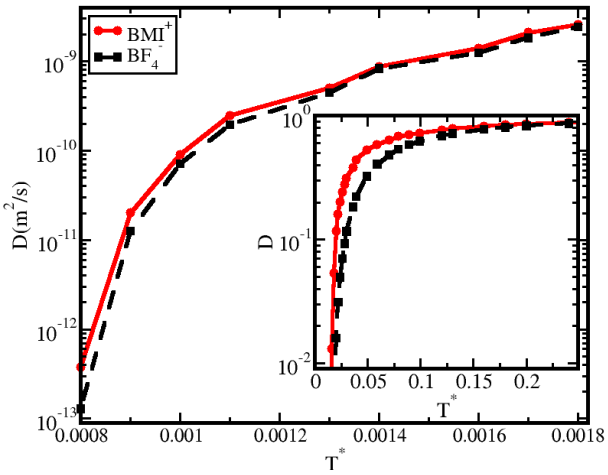

Figure 5.2: Diffusion coefficient versus reduced temperatures for the system BMI^+ BF_4^-. Left panel shows the results obtained using all-atom simulations of systems. The panel at the right contains the theoretical results obtained form the SCGLE theory.

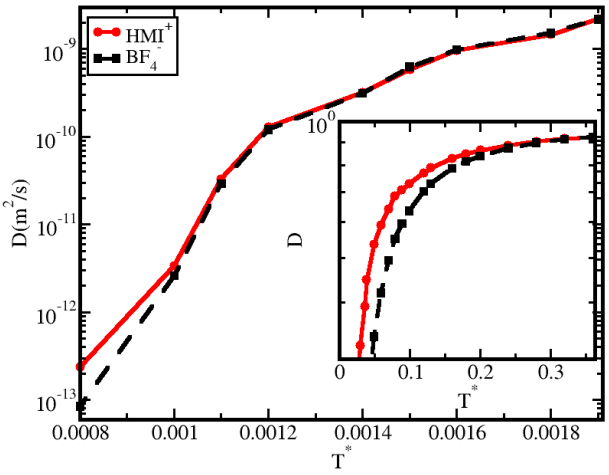

Figure 5.3: Diffusion coefficient versus reduced temperatures for the system HMI^+ BF_4^-. Left panel shows the results obtained using all-atom simulations of systems. The panel at the right contains the theoretical results obtained form the SCGLE theory.

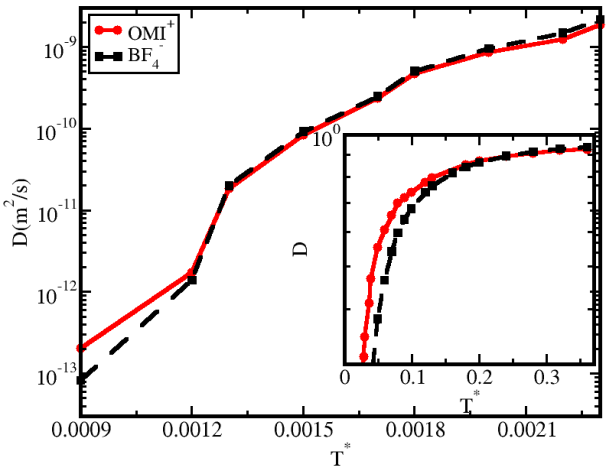

Figure 5.4: Diffusion coefficient versus reduced temperatures for the system OMI^+ BF_4^-. Left panel shows the results obtained using all-atom simulations of systems. The panel at the right contains the theoretical results obtained form the SCGLE theory.

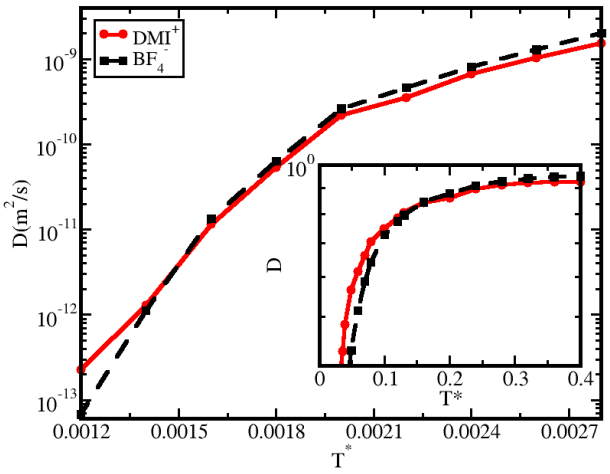

Figure 5.5: Diffusion coefficient versus reduced temperatures for the system DMI^+ BF_4^-. Left panel shows the results obtained using all-atom simulations of systems. The panel at the right contains the theoretical results obtained form the SCGLE theory. Reproduced from [60], with the permission of AIP Publishing.

Despite the complexity of the studied ionic liquids, both theory and simulation exhibit the same general trends, demonstrating the validity of the simplified model for exploring novel phases and behaviors in complex systems.

Furthermore, our results identify regions where partial arrest occurs, with larger ionic species diffusing among the smaller ones. This counterintuitive behavior can be explained by inefficient charge screening of the larger ions due to volume effects. As a result, small-ion electrostatic interactions become stronger than those between oppositely charged species, promoting the formation of a glass phase for the smaller ions while the larger ones remain fluid.

These findings are consistent with previously reported studies. The emergence of electronic conductivity can be attributed to the anomalous diffusion of larger ions within a glassy matrix of smaller ions. From a practical standpoint, we focus on the case where cations become arrested while anions remain fluid. Since charge exchange in our model does not alter thermodynamic or dynamic properties, this configuration serves as a representative state for ionic liquid crystals, such as those described in [66] which involve small lithium cations and bulky TFSI-derived anions.

Our results suggest that bulky cations can be immobilized through steric hindrance or other molecular interactions, allowing smaller species to move freely through the electrolyte. This provides an intriguing design strategy for single-ion conductors, where the salt composition is optimized to maximize the glassy behavior of macro-ionic species while maintaining the mobility of micro-ions.

5.2 Conclusion

The data demonstrates that both cations and anions undergo similar dynamic changes with temperature. At low temperatures, diffusivity approaches negligible values, consistent with glassy behavior, whereas at higher temperatures, molecular mobility is activated, and diffusivity increases sharply. The strong qualitative agreement between the two systems suggests that their underlying dynamic behavior is analogous, despite minor quantitative differences.

This study highlights the universality of glassy dynamics in ionic liquids and underscores the potential of simplified models to capture key features of these complex systems. The insights gained provide valuable guidelines for designing ionic materials with tunable transport properties, particularly in applications involving single-ion conductors and ionic liquid crystals.

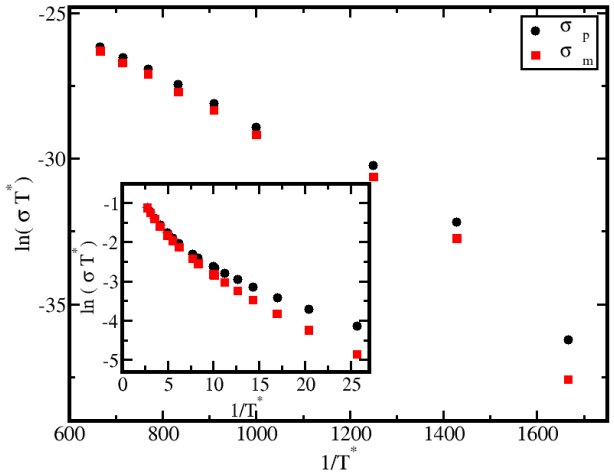

Figure 5.6: The main panel presents results from all-atom simulations, while the inset displays the corresponding theoretical calculations. The data correspond to the EMIM$^+$-BF$_4^-$ system, alongside theoretical predictions based on a primitive model with a size asymmetry of $\delta = \sigma_{big}/\sigma_{small} = 0.69$ nm/0.2 nm. A strong qualitative agreement between simulation and theory is observed. Reproduced from [60], with the permission of AIP Publishing.

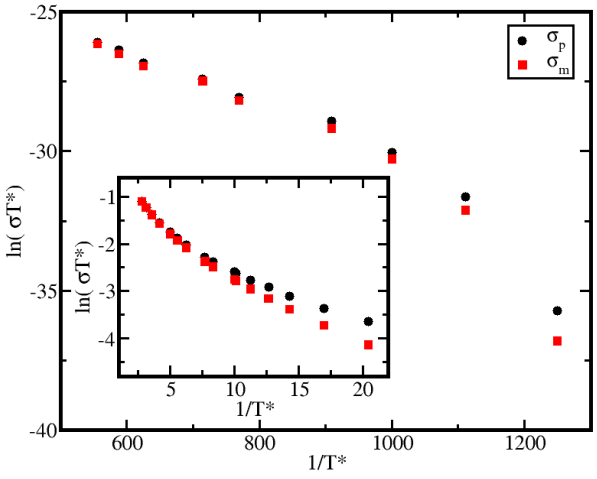

Figure 5.7: Results for the DMIM$^+$-BF$_4^-$ system and a primitive model with $\delta = \sigma_{big}/\sigma_{small} = 0.89$ nm/0.2 nm. Notably, the system with the larger asymmetry exhibits a crossover, which is observed in both simulations and theoretical calculations. Overall, we find a strong qualitative agreement between simulation and theory.

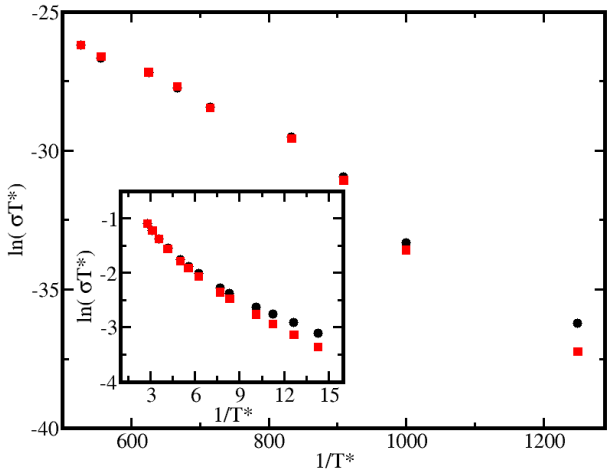

Figure 5.8: Results for the DMIM$^+$-BF$_4^-$ system and a primitive model with $\delta = \sigma_{big}/\sigma_{small} = 1.46$ nm/0.2 nm. Notably, the system with the larger asymmetry exhibits a crossover, which is observed in both simulations and theoretical calculations. Overall, we find a strong qualitative agreement between simulation and theory.

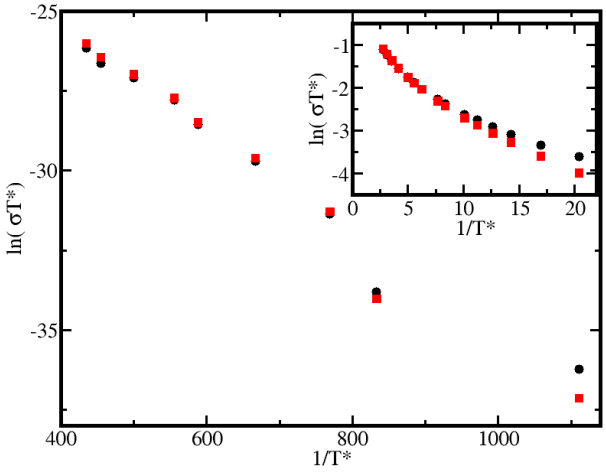

Figure 5.9: Results for the DMIM$^+$-BF$_4^-$ system and a primitive model with $\delta = \sigma_{big}/\sigma_{small} = 1.46$ nm/0.2 nm. Notably, the system with the larger asymmetry exhibits a crossover, which is observed in both simulations and theoretical calculations. Overall, we find a strong qualitative agreement between simulation and theory.

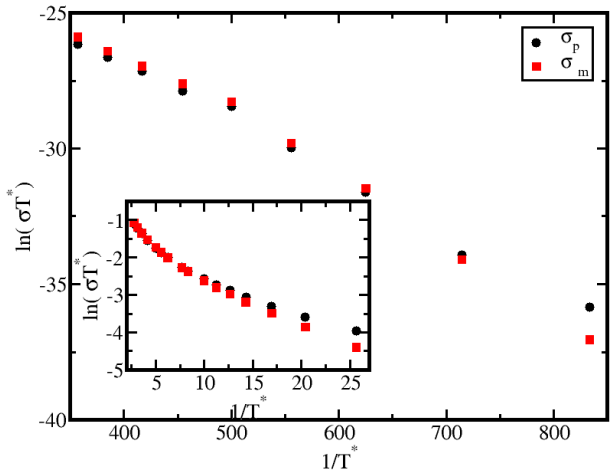

Figure 5.10: Results for the $DMIM^+$-BF_4^- system and a primitive model with $\delta = \sigma_{big}/\sigma_{small} = 1.46$ nm/0.2 nm. Notably, the system with the larger asymmetry exhibits a crossover, which is observed in both simulations and theoretical calculations. Overall, we find a strong qualitative agreement between simulation and theory. Reproduced from [60], with the permission of AIP Publishing.

Chapter 6

Perspectives

The main results presented in previous chapters show the reliability of the PM-SCGLE framework in the fundamental description of the glassy dynamics of a wide spectrum of ionic liquids. Hence, further routes of future research are suggested. This chapter also outlines several directions for future research. One such avenue is the exploration of the fully pure primitive model, which could provide deeper insights into the system's behavior. Another ongoing effort focuses on developing a model that enables the study of systems with more than two species, allowing for a broader understanding of complex mixtures and their phase transitions. These future investigations will be crucial in advancing our comprehension of inhomogeneous states and their implications for the study of ionic liquids.

6.1 Heterogenous systems

This section presents an in-depth analysis of the inhomogeneous states observed in our simulations under NVT conditions. While these conditions generally ensure homogeneity, our results indicate the presence of large empty spaces during system evolution, a phenomenon that has been only marginally addressed in the literature. The emergence of these "holes" raises important questions regarding the nature of the phase behavior in our system.

To explore the underlying mechanisms behind this observation, we investigate two primary hypotheses: the possibility of incorrect application of GROMACS methods or parameters, and the potential occurrence of a true phase transition. Furthermore, our study highlights a consistent trend in the relationship between temperature and hole size, reinforcing the need for further investigation into the thermodynamic behavior of the system.

As demonstrated in the previous section, NPT conditions ensure homogeneity within the system. However, a striking observation in this study, in contrast to previous results, is the emergence of inhomogeneous states characterized by the presence of large empty spaces during the system's

evolution. It is worth noting that such ”holes” observed in our simulations have been marginally reported in the existing literature, with only tentative suggestions found thus far. Nonetheless, several research groups employ NPT conditions for their production runs [32, 33], possibly for reasons similar to those that led us to adopt these conditions. Of course, this assertion regarding other research groups remains speculative.

It is important to highlight that the emergence of ”holes” occurs exclusively during production runs conducted at constant volume. Consequently, two primary hypotheses arise to rationalize this observed behavior: (i) an incorrect application of GROMACS methods or parameters, or (ii) the observation of a genuine phase transition. The first hypothesis could be attributed to advanced sampling techniques implemented in the latest GROMACS release or to potential errors in our input files. Regarding the second hypothesis, theoretical studies on ionic liquids (ILs) predict a gas-liquid transition, wherein coexistence and instability regions arise at low temperatures and densities [22, 34, 35]. Both hypotheses have been systematically explored in this study.

A comprehensive analysis of the inhomogeneous systems observed in this thesis is of main relevance in order to obtain a deep understanding of the phase behavior of ionic liquids. Our preliminary analysis is shown below starting at a high temperature, namely 700 K (Figure 6.1). Subsequently, different temperatures were explored to record relevant data. At 800 K (Figure 6.2), the hole size decreases, prompting the decision to further increase the temperature in the expectation that the hole would disappear. At 900 K (Figure 6.3), although the hole is smaller, it persists. Consequently, instead of continuing to increase the temperature, we lowered it to 600 K (Figure 6.4), where significantly larger holes were observed. Finally, at 500 K (Figure 6.5), a seemingly homogeneous structure appeared at first glance (first figure from left to right); however, upon closer inspection, inhomogeneities persisted.

From the results obtained using the NVT production run, a clear trend emerges: at lower temperatures, the holes are larger, while at higher temperatures, the holes are smaller. Regardless of the temperature applied, the presence of holes remains a consistent feature of the system. This study is left for future research.

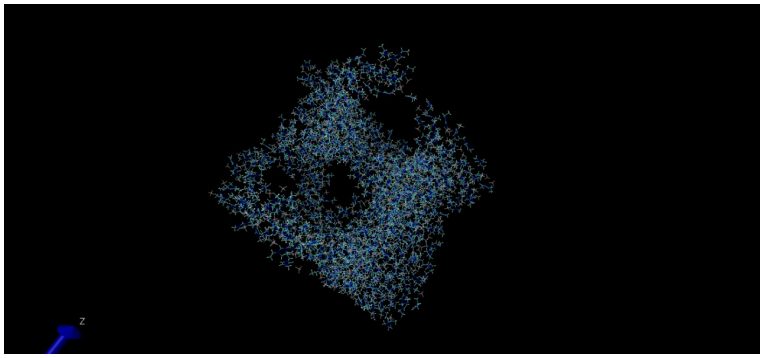

Figure 6.1: Structure of the production at 700 K.

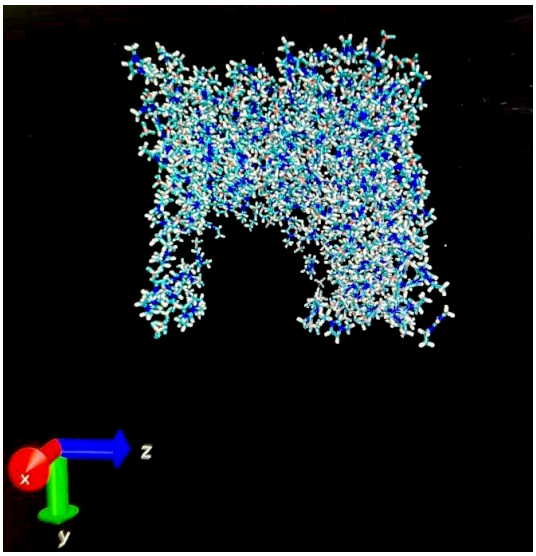

Figure 6.2: Structure of the production at 800 K.

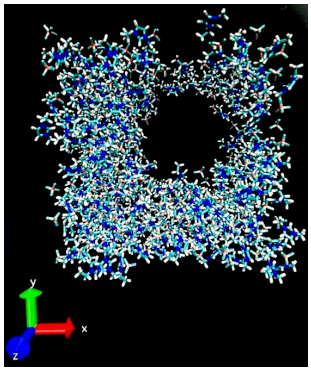

Figure 6.3: Structure of the production at 900 K.

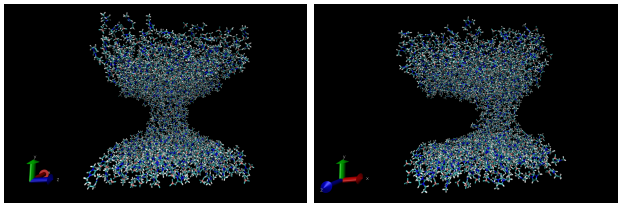

Figure 6.4: Structure of the production at 600 K.

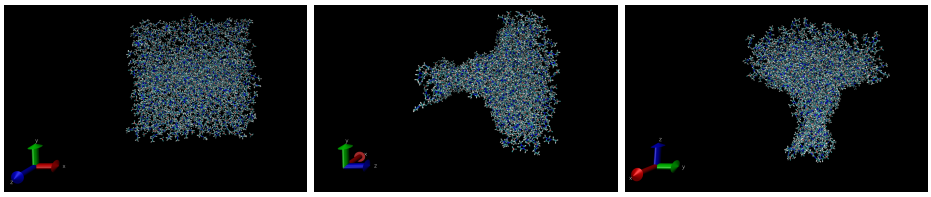

Figure 6.5: Structure of the final production (NVT productioin) at 500 K.

6.2 Brownian dynamics simulations of Primitive Model.

Another avenue for future research is the performing of Brownian dynamics simulations of the Primitive Model, namely, the direct implementation of simulations of electrically charged hard spheres with size asymmetry. Exploring this approach could provide further insights into the observed phenomena and contribute to a deeper understanding of the system's behavior. This aspect is also left for future investigation.

6.3 Development of a three-component Model

Work is currently underway on developing a model that allows the study of systems with more than two species. This approach aims to provide a broader perspective on the behavior of complex mixtures and their phase transitions. However, this model is still under development and will be addressed in future research.

Chapter 7

Conclusions

This thesis employs the Self-Consistent Generalized Langevin Equation (SCGLE) theory to investigate a theoretical binary mixture of charged hard spheres. This theoretical approach is particularly relevant for understanding the dynamic and structural behavior of complex systems, such as ionic liquids and charged colloidal suspensions, which have wide-ranging applications in materials science and energy storage. For each species i , the equilibrium version of SCGLE utilizes the parameter γ_i to identify the limit lines where kinetic arrested states exist. These arrested states delineate the boundaries between fluid and amorphous solid phases in the system. A distinct pair of coordinates, ϕ_T and T^*, representing the total volume fraction and the reduced temperature, respectively, describe a specific location within this phase space. Using the dynamic SCGLE theory, it becomes possible to construct a kinetic arrest diagram that elucidates the interplay between particle size asymmetry and the dynamic behavior of the system.

The results presented in this thesis are consistent with earlier equilibrium investigations, confirming the robustness of the SCGLE framework. Beyond this validation, the study uncovers the existence of partially arrested regions within the phase space, which exhibit unique charge transport properties. These regions represent a fascinating combination of arrested and fluid-like states and are observed in systems with significant size asymmetry between cations and anions, such as the 3.5:1, 4.5:1, 4.8:1, 6.0:1, and 7.3:1 ratios examined here. These findings are especially relevant for systems like polymerized ionic liquids and ionic liquid crystals, where interstitial conductive domains emerge between arrested cations. Such behavior highlights the potential of these systems for applications in advanced energy storage technologies and the design of novel conductive materials.

One of the key strengths of this approach lies in the simplicity of the underlying model. By employing a spherical approximation for ions and an analytical solution for structural properties, the model provides a coherent and comprehensive perspective on the system's behavior. Remarkably, despite its simplicity, the model offers results that are consistent with all-atom molecular dynamics (MD) simulations, which are computationally more intensive. However, while the current model

serves as a solid foundation, it also exhibits limitations. For example, the inaccurate mapping of temperature values in the theoretical framework hinders direct quantitative comparisons with experimental data or MD simulations. To address this, future work should focus on refining the model to incorporate additional factors, such as the non-spherical shape of cations and other relevant effects, enabling a more accurate representation of the system's behavior.

Future refinements to the structural solutions proposed in this thesis could overcome these limitations. By improving the accuracy of the temperature mapping, it would be possible to establish direct quantitative comparisons with both experimental results and high-resolution MD simulations. Furthermore, the insights gained from such refinements could lead to the development of more advanced kinetic arrest diagrams, capturing additional nuances of the dynamic behavior in charged particle systems.

Despite the current model's constraints, the findings reported in this thesis demonstrate new and significant behaviors that are highly relevant to the advancement of energy storage devices. The partially arrested regions identified in this study could inspire the engineering of novel molecular architectures and materials with enhanced charge transport properties. By leveraging these discoveries, future research may pave the way for the development of innovative technologies that exploit the unique dynamics of charged particle systems.

Appendix A

A.1 Purpose and Goals of Molecular Dynamics Simulations

Molecular dynamics (MD) simulations are a computational science method that allows the study of structure and dynamics by solving the equation of motion [21]. These simulations have found applications in various fields, including biophysics, drug design, and fundamental research in chemistry and physics. Some of the systems and materials that can be studied include proteins, liquid crystals, colloidal systems, polymers, and glass-forming liquids.

The goal of a simulation is not necessarily to replicate the real system exactly. Simulations are often used to explore key aspects of the dynamics and/or structures of a model, and they do not need to be fully realistic. Therefore, it is essential to understand the limitations of the methods and assess them based on their intended purpose. As mentioned earlier, MD simulations are capable of studying dynamics because the equation of motion is solved numerically.

Some of the specific purposes for which MD simulations are useful include:

- They allow for the study of important and widely recognized dynamics and structural aspects, such as ion diffusion, conduction mechanisms, vitrification capabilities, and mixed alkali effects.
- Simulations can be used to predict properties of systems that are not known before experimentation. They can provide properties that are difficult to obtain experimentally, such as spatial information about the wavevector dependence of the intermediate scattering function.
- They are valuable for studying systems under extreme conditions, such as high pressure and temperature, which may be challenging to achieve experimentally.
- In some cases, real-world experiments may contaminate the environment through heat and material release, posing safety risks. Simulations provide a way to study systems without the risk of environmental contamination.

- Simulations can be employed to investigate various systems for desired properties. In such cases, the lower resolution of the simulations may not be a disadvantage, especially if the required computational time is short.
- They can be used to examine how system properties change when factors such as structure, composition, mass, size, or other parameters are modified.
- Simulations can be systematically applied to design new materials with better performance for specific applications.
- Of course, simulations can also be used to compare with experimental data and validate theoretical predictions. More recently, they have been employed to build and/or refine theories and models.

In the field of ionics, MD simulations have also been applied to understand the dynamics and structures of new materials and functional compounds, such as solid-state batteries, actuators, and nanomachines. This trend is expected to continue in future studies [21].

A.2 Physical Concepts for Molecular Dynamics Simulations

In this study, we will focus exclusively on classical simulations of liquids. One way to test the classical hypothesis for atomic systems is by evaluating the de Broglie thermal wavelength, Λ, defined as:

$$\Lambda = \left(\frac{2\pi\beta\hbar^2}{m} \right)^{\frac{1}{2}}, \tag{A.1}$$

where m is the mass of the atom, and $\beta = 1/K_B T$. To justify using a classical approach for static properties, it is essential for Λ to be significantly smaller than a, where $a \approx \rho^{-1/3}$ is the mean nearest-neighbor distance [22].

Using the classical approximation simplifies the problem considerably, as Newton's second law is sufficient to describe the dynamics in these simulations.

By applying the classical approximation, we can clearly distinguish the contributions from thermal motion and particle interactions when considering thermodynamic properties.

We can also approach the issue from a broader perspective, such as considering the system size. A realistic simulation would require around 10^{23} particles (Avogadro's number), but this is impractical due to the difficulty of analyzing such a large system. Thus, the first approximation is to simulate a representative sample of molecules. The number of molecules selected should be large enough to provide statistically averaged results with minimal fluctuations, ensuring accurate representation of the system's macroscopic properties.

For our simulations, we will use approximately 1000 molecules, each containing 10 or 20 atoms. The key challenge then is how to scale up the system while maintaining reliable macroscopic properties. Additionally, how can we minimize edge effects (surface effects) given the system's finite size?

A.2.1 Equations of Motion for Atomic Systems

As previously mentioned, Newton's equation of motion is appropriate for describing the dynamics of all molecules in the system, meaning we need to solve:

$$\mathbf{F} = m\mathbf{a} \quad \text{for } N \text{ particles}, \tag{A.2}$$

or

$$\mathbf{F}_i = m^{[i]} \frac{d^2\mathbf{x}^{[i]}}{dt^2} \quad \text{for } i = 1, \ldots, N, \tag{A.3}$$

where $\mathbf{F}_i$ represents the forces acting on particle i, $m^{[i]}$ denotes the particle's mass, and $\mathbf{x}^{[i]}$ are the particle coordinates. Thus, the problem we need to solve is a differential equation.

Several numerical methods are available for integrating the equations of motion [23]. Most integration methods can be disregarded because the most computationally expensive task is force evaluation, and any method that requires more than one force calculation per time step would be inefficient unless it can significantly increase the timestep Δt while maintaining accuracy. However, due to the strong repulsive forces in typical Lennard-Jones (LJ) potentials at short distances, there is an upper limit to Δt, making well-known methods like Runge-Kutta unsuitable beyond this limit. The same applies to adaptive methods that adjust Δt to preserve precision, which is ineffective due to the rapidly changing local environment of each atom.

Only two methods have gained widespread use: the low-order leapfrog technique and the predictor-corrector approach. These methods come in various forms, but we will focus on the leapfrog and Verlet methods. For more information on the predictor-corrector approach, see [23].

The Leapfrog and Verlet Methods

The leapfrog and Verlet methods are simple numerical techniques that are widely used in MD simulations and are mathematically equivalent. In their most basic form, these methods provide coordinates accurate to third order in Δt, and when Lennard-Jones potentials are used, they tend to conserve energy better than higher-order methods. They also require minimal memory.

The Verlet method is derived from the Taylor expansion of the coordinate variable $x(t)$:

$$x(t+h) = x(t) + h\dot{x}(t) + \frac{h^2}{2}\ddot{x}(t) + O(h^3), \tag{A.4}$$

where t is the current time, and $h \equiv \Delta t$. Here, $\dot{x}(t)$ is the velocity, and $\ddot{x}(t)$ is the acceleration. While $\ddot{x}$ is expressed as a function of t, it is actually determined by the force law at time t. By adding the corresponding expansion for $x(t-h)$ and rearranging, we obtain:

$$x(t+h) = 2x(t) - x(t-h) + h^2\ddot{x} + O(h^4). \tag{A.5}$$

The truncation error is of order $O(h^4)$ because the h^3 terms cancel. The velocity is not directly involved in the solution, but if needed, it can be calculated as:

$$\dot{x}(t) = \frac{x(t+h) - x(t-h)}{2h} + O(h^2), \tag{A.6}$$

with higher-order expressions available if necessary, though they are rarely used.

The leapfrog method is derived similarly. Rewriting the Taylor expansion as:

$$x(t+h) = x(t) + h\left[\dot{x}(t) + \frac{h}{2}\ddot{x}(t)\right] + O(h^3), \tag{A.7}$$

the term multiplying h is $\dot{x}(t+\frac{h}{2})$, so equation A.7 becomes:

$$x(t+h) = x(t) + h\dot{x}\left(t + \frac{h}{2}\right). \tag{A.8}$$

Subtracting the corresponding expression for $\dot{x}(t-\frac{h}{2})$ from $\dot{x}(t+\frac{h}{2})$, we get:

$$\dot{x}\left(t + \frac{h}{2}\right) = \dot{x}\left(t - \frac{h}{2}\right) + h\ddot{x}(t). \tag{A.9}$$

The leapfrog integration formulas are then equations A.9 and A.8. The fact that the coordinates and velocities are evaluated at different times does not pose an issue. If an estimate of $\dot{x}(t)$ is required, there is a simple connection:

$$\dot{x}(t) = \dot{x}\left(t \mp \frac{h}{2}\right) \pm \frac{h}{2}\ddot{x}(t). \tag{A.10}$$

The initial conditions can be handled similarly, although a minor inaccuracy in the starting state, namely the distinction between $\dot{x}(0)$ and $\dot{x}\left(\frac{h}{2}\right)$, is often ignored. The method can be implemented in a more convenient two-step form that avoids having coordinates and velocities at different times, which corresponds to:

$$\dot{x}\left(t + \frac{h}{2}\right) = \dot{x}(t) + \frac{h}{2}\ddot{x}(t),\ x(t+h) \qquad = x(t) + h\dot{x}\left(t + \frac{h}{2}\right), \tag{A.11}$$

followed by:

$$\dot{x}(t+h) = \dot{x}\left(t + \frac{h}{2}\right) + \frac{h}{2}\ddot{x}(t+h). \tag{A.12}$$

A.2.2 Periodic bondary conditions

Computer simulations are typically carried out on a small number of molecules, ranging from 10 to $10,000$. The system's size is limited by the available memory on the host computer and, more importantly, by the program's execution speed [19]. The time required for a double loop that calculates forces or potential energy is proportional to N^2. While special techniques can reduce this dependency to $\mathcal{O}(N)$ for extremely large systems, the force/energy loop ultimately determines the simulation speed. As a result, smaller systems will always be more efficient. The intermolecular forces may be sufficient to hold the system together during the simulation; otherwise, the molecules may be confined within a potential that represents a container, preventing them from drifting. However, these setups are not ideal for simulating bulk liquids. A major challenge in such simulations is the significant fraction of molecules that lie on the surface of any small sample. For example, in a system of 1000 molecules arranged in a $10 \times 10 \times 10$ cube, at least 488 molecules will be positioned on the cube's faces. Whether or not the cube is surrounded by a container wall, the molecules on the surface experience different forces compared to those in the bulk.

Surface effects can be addressed by using periodic boundary conditions (PBC). In this approach, the cubic box is repeated throughout space, forming an infinite lattice. As a molecule moves within the original box, its periodic image in each adjacent box moves identically. Therefore, when a molecule exits the central box, one of its images enters through the opposite face. The central box has no walls or surface molecules, providing a convenient reference frame for measuring the coordinates of the N molecules. This system is illustrated in Fig. A.1. The duplicated boxes are labeled arbitrarily as A, B, C, and so on. As particle 1 moves across a boundary, its images 1_A, 1_B, etc. (where the subscript denotes the box containing the image) cross their corresponding boundaries. The number density in the central box, and throughout the entire system, remains constant. It is not necessary to store the coordinates of all the images (which would be infinite); instead, it suffices to store only the coordinates of the molecules in the central box. When a molecule crosses a boundary, the simulation simply shifts its focus to the image it just entered. One can imagine the simulation box as being rolled up to form the surface of a three-dimensional torus, even though such a physical surface doesn't exist.

This method eliminates the need to consider an infinite number of system replicas or image particles. This accurately reflects the system's topology, even if it does not account for its geometry. A similar analogy exists for a three-dimensional periodic system, although it is harder to visualize.

Due to its geometrical simplicity, the cubic box is almost exclusively used in computer simulations. If computational resources allow, it is standard practice to increase both the number of

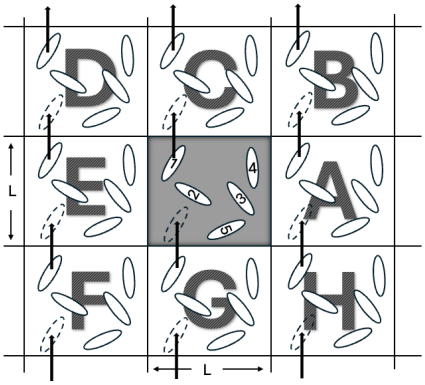

Figure A.1: A two-dimensional periodic system. Molecules can cross each box's four edges. In a three-dimensional system, molecules would be free to cross any of the six faces of a cube [19].

molecules and the box size to maintain a constant density.

Potential Truncation

Next, we must address the calculation of properties for systems subject to periodic boundary conditions. A central aspect of molecular dynamics (MD) simulations involves calculating the potential energy of a given configuration, specifically the forces acting on all molecules. To compute the force on molecule 1 or the contribution to its potential energy, we consider pairwise additivity. Interactions between molecule 1 and every other molecule in the simulation box are included, resulting in a sum of $N-1$ terms. However, in principle, it is essential to consider interactions between molecule 1 and the images i_A, i_B, and others in the surrounding boxes. This leads to an infinite number of terms, which is impractical to compute. For a short-range potential energy function, we can simplify the calculation by using an approximation. We consider molecule 1 to be at the center of a region with the same size and shape as the simulation box (Fig. A.2). Molecule 1 interacts with all the molecules whose centers lie within this region, i.e., the closest periodic images of the other $N-1$ molecules. This is known as the *minimum image convention*. For example, in Fig. A.2, molecule 1 interacts with molecules 2, 3_A, 4_E, and 5_C. This approach is a natural consequence of the PBC.

In the minimum image convention, the calculation of potential energy due to pairwise-additive interactions involves $N(N-1)$ terms. This can still be a large calculation for systems with 1000 particles. A significant improvement is possible by noting that the greatest contribution to the potential and forces comes from nearby molecules, and for short-range forces, we typically apply a spherical cutoff. This means the pair potential $v(r) \to 0$ for $r \geq r_c$, where r_c is the cutoff distance. The dashed circle in Fig. A.2 represents this cutoff, where molecules 2 and 4_E contribute to the

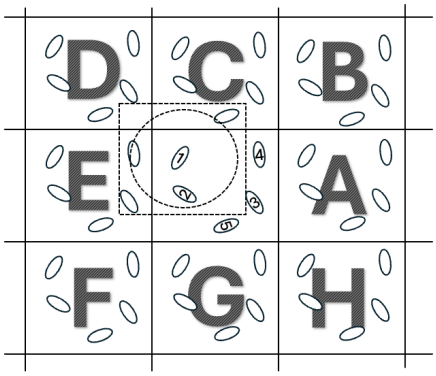

Figure A.2: The minimum image convention in a two-dimensional system. The box centered on molecule 1 contains five molecules. The dashed circle represents a potential cutoff [19].

force on molecule 1, as their centers lie within the cutoff distance, while molecules 3_E and 5_E do not. In a cubic simulation box with side length L, the number of neighbors considered explicitly is reduced by a factor of approximately $\frac{4\pi r_c^3}{3L^3}$, leading to substantial computational savings. The introduction of the spherical cutoff should cause only a small perturbation, provided the cutoff distance is sufficiently large.

The cutoff distance must not exceed $\frac{1}{2}L$ to ensure consistency with the minimum image convention.

A.2.3 Radial Distribution Function (RDF)

The radial distribution function (RDF), denoted as $g(r)$, is a pair distribution function that reveals the local arrangement of atoms within a system.

The $g(r)$ function is proportional to the likelihood of finding two atoms separated by a distance of $r + \Delta r$. By applying a Fourier transform to $g(r)$, we obtain the structure factor $S(k)$, which can be measured experimentally through techniques such as x-ray or neutron diffraction. This allows us to correlate the RDF with the atomic structure and organization determined through experimental methods [19, 24].

Although $g(r)$ can be derived analytically using methods like the hypernetted chain or the Percus-Yevick equation, we will focus on the expression used in molecular dynamics (MD) simulations. MD simulations are often simpler for obtaining $g(r)$ since they provide the trajectories of all atoms over time.

To derive the expression for $g(r)$ used in MD simulations, we begin with its definition from [24]:

$$\rho g(\mathbf{r}) = \frac{1}{N} \left\langle \sum_{i}^{N} \sum_{j \neq i}^{N} \delta[\mathbf{r} - \mathbf{r}_{ij}] \right\rangle,$$

where N is the total number of atoms, $\rho = \frac{N}{V}$ is the number density, $\mathbf{r}_{ij}$ is the vector between the centers of atoms i and j, and δ is the Dirac delta function. For homogeneous and uniform substances, the atomic structure depends only on the distance r between atoms and is independent of the orientation of the vector $\mathbf{r}$, simplifying the expression to:

$$\rho g(r) = \frac{1}{N} \left\langle \sum_{i}^{N} \sum_{j \neq i}^{N} \delta[r - r_{ij}] \right\rangle.$$

The double sum involves $N(N-1)$ terms, and since the distance r_{ij} is symmetric under the exchange of indices i and j, only half of the terms are unique. Thus, we can rewrite equation A.2.3 as:

$$\rho g(r) = \frac{2}{N} \left\langle \sum_{i}^{N} \sum_{j<i}^{N} \delta[r - r_{ij}] \right\rangle.$$

The normalization of $g(r)$ is achieved by integrating over all possible separations between two atoms:

$$\rho \int g(r) d\mathbf{r} = \frac{2}{N} \left\langle \sum_{i}^{N} \sum_{j<i}^{N} \delta[r - r_{ij}] d\mathbf{r} \right\rangle.$$

Using the properties of the Dirac delta function:

$$\delta[r - r_{ij}] = \begin{cases} \infty & \text{if the center of atom } ij \text{ is at } r_{ij}, \\ 0 & \text{if the center of atom } ij \text{ is not at } r_{ij}. \end{cases}$$

The normalization condition of the delta function is:

$$\int \delta[r - r_{ij}] d\mathbf{r} = 1.$$

Thus, we obtain:

$$\rho \int g(r) d\mathbf{r} = N - 1 \approx N.$$

This equation A.2.3 implies that if we focus on a single atom and count the other atoms in the system, we find approximately $N-1$ other atoms. It also leads to a probabilistic interpretation of $g(r)$:

$$\frac{\rho}{N-1}g(r)V(r,\Delta r) = \begin{cases} \text{Probability that an atomic center lies} \\ \text{in a spherical shell of radius } r \text{ and thickness } \Delta r \\ \text{with the shell centered on another atom.} \end{cases}$$

Where $V(r,\Delta r)$ represents the volume of the spherical shell with thickness Δr. The RDF reveals how the presence of one atom influences the positions of neighboring atoms over time. For atomic separations smaller than the atomic diameter, $g(r)=0$, and for large separations in fluids, $g(r)=1$, indicating no influence between atoms and a uniform density.

To calculate $g(r)$ from simulation data, we modify equation A.2.3 by using a small but finite thickness Δr for the shell:

$$\rho \sum_{\Delta r} g(r)V(r,\Delta r) = \frac{2}{N}\sum_{\Delta r}\left\langle \sum_{i}^{N}\sum_{j<i}^{N}\delta[r-r_{ij}]\Delta\mathbf{r}\right\rangle.$$

The double sum in equation A.2.3 represents a counting operation, analogous to:

$$\sum_{i}^{N}\sum_{j<i}^{N}\delta[r-r_{ij}]\Delta\mathbf{r} = N(r,\Delta r),$$

where $N(r,\Delta r)$ is the number of atoms within the spherical shell of radius r and thickness Δr, centered on another atom. Substituting this into equation A.2.3 gives:

$$g(r) = \frac{\langle N(r,\Delta r)\rangle}{\frac{1}{2}N\rho V(r,\Delta r)}.$$

Taking the time average over M time steps:

$$g(r) = \frac{\sum_{k=1}^{M} N_k(r,\Delta r)}{M\left(\frac{1}{2}N\right)\rho V(r,\Delta r)}.$$

Here, N_k is the result of the counting operation at time t_k. Physically, equation A.2.3 represents the ratio of local density $\rho(r)$ to the system's overall density ρ.

Since the simulation is carried out within a cubic container, the RDF can only be calculated for distances up to $\frac{1}{2}L$, the radius of the largest sphere that can fit within the cubic container.

A.2.4 Mean Squared Displacement

The Mean Squared Displacement (MSD) quantifies the deviation of the position of a randomly moving particle from its initial position over time. It can be interpreted as the extent to which the particle "explores" the system.

To derive the MSD, we consider one-dimensional diffusion as governed by Fick's law [24],

$$N\dot{x} = -D\frac{\partial N}{\partial x}, \tag{A.13}$$

where $N = N(x,t)$ represents the number of atoms per unit volume (i.e., length) at position x and time t, $\dot{x}$ is the local velocity at (x,t), and D denotes the diffusion coefficient. Thus, $N\dot{x}$ represents the flux. By applying the material balance to a differential fluid element, we obtain the mass continuity equation

$$\frac{\partial N}{\partial t} + \frac{\partial (N\dot{x})}{\partial x} = 0, \tag{A.14}$$

and combining these two equations results in the diffusion equation:

$$\frac{\partial N}{\partial t} = D\frac{\partial^2 N}{\partial x^2}. \tag{A.15}$$

The diffusion equation can be solved with initial conditions for the temporal and spatial evolution of $N(x,t)$. For instance, if N_0 atoms are initially located at the origin ($x = 0$) at time $t = 0$, the solution to A.15 is

$$N(x,t) = \frac{N_0}{2\sqrt{\pi D t}} \exp\left[\frac{-x^2}{4Dt}\right]. \tag{A.16}$$

Thus, at any time $t > 0$, the atoms are spatially distributed in a Gaussian distribution centered at the origin. As time progresses, atoms diffuse away from the origin, causing the Gaussian to broaden.

At any time $t > 0$, the second moment of the distribution provides the MSD of atoms, expressed as

$$\left\langle [x(t) - x(0)]^2 \right\rangle = \frac{1}{N_0}\int x^2 N(x,t)dx. \tag{A.17}$$

Substituting A.16 into A.17 and performing the integration gives the MSD, which is directly related to the diffusion coefficient:

$$\left\langle [x(t) - x(0)]^2 \right\rangle = 2Dt. \tag{A.18}$$

This result holds when the time t is much greater than the average time between atom collisions. The three-dimensional counterpart of A.18 is:

$$\lim_{t\to\infty} \frac{\left\langle [\mathbf{r}(t) - \mathbf{r}(0)]^2 \right\rangle}{6t} = D. \tag{A.19}$$

In simulations, the brackets represent time-averaged quantities. Since the diffusion coefficient is constant at a given state, A.19 implies that the MSD increases linearly with time at large t.

Another method to derive the MSD is through the Green-Kubo relation [24]. This can be computed using the velocity autocorrelation function, and for a one-dimensional system, we have

$$\lim_{t\to\infty} \frac{\left\langle [x(t) - x(0)]^2 \right\rangle}{2t} = \int_0^\infty d\tau \langle v(\tau) v(0) \rangle. \tag{A.20}$$

The self-diffusion coefficient can be obtained by rewriting the equation A.19 as

$$D = \frac{1}{6N} \lim_{t\to\infty} \frac{d}{dt} \left\langle \sum_i^N [\mathbf{r}_i(t) - \mathbf{r}_i(0)]^2 \right\rangle, \tag{A.21}$$

where D is proportional to the slope of the MSD at long times.

The self-diffusion coefficient, using the Green-Kubo relation, is expressed as

$$D = \int_0^\infty d\tau \langle v(\tau) v(0) \rangle. \tag{A.22}$$

A.2.5 Handling Long-Range Forces

Long-range forces are defined as those whose spatial interaction decays no faster than r^{-d}, where d is the system's dimensionality. Examples include charge-charge interactions between ions ($v^{zz}(r) \sim r^{-1}$) and dipole-dipole interactions between molecules ($v^{\mu\mu}(r) \sim r^{-3}$). These forces present significant challenges in simulations due to their long-range nature, particularly in typical simulations of 500 molecules. A potential solution would be to increase the size of the simulation box L to several hundred nanometers, thus reducing the effective range of the potentials due to screening by nearby molecules. However, this approach is not practical even with modern computers, as the simulation time scales with N^2, or L^6.

How can we handle such potentials? One approach is using lattice methods like the Ewald sum, which accounts for interactions of an ion or molecule with all of its periodic images.

The Ewald sum involves converting the slowly converging sum in r^{-1} into two rapidly converging series. One series represents the short-range potential in real space and can be truncated, while the second is a series over reciprocal-lattice vectors.

The Ewald Sum

The Ewald sum is a method for efficiently calculating the interaction between an ion and all its periodic images. Consider a system of N atoms, each carrying a charge. A periodic array of replicated systems is created, and the total interaction energy includes contributions from all replicas.

The total interaction energy is given by:

$$V = \frac{1}{2} \sum_{\mathbf{n}}{}' \sum_{i=1}^{N} \sum_{j=1}^{N} \frac{q_i q_j}{|\mathbf{r}_{ij} + L\mathbf{n}|}, \tag{A.23}$$

where q_i is the charge of atom i, $\mathbf{n}$ is the box index vector, and L is the box length. The sum is over all integer vectors $\mathbf{n}$, with the prime indicating that terms where $i = j$ (self-interaction) are omitted.

The Ewald sum formula reorganizes the sum into terms over spherical shells, assuming charge neutrality, $\sum_j q_j = 0$. The formula is:

$$\begin{aligned} V &= \sum_{1 \le i < j \le N} q_i q_j \left[\sum_{\mathbf{n}}{}' \frac{\text{erfc}\,(\alpha |\mathbf{r}_{ij} + L\mathbf{n}|)}{|\mathbf{r}_{ij} + L\mathbf{n}|} \right. \\ &+ \left. \frac{1}{\pi L} \sum_{n \neq 0} \frac{1}{n^2} \exp\left(-\frac{\pi^2 n^2}{\alpha^2 L^2} + \frac{2\pi i}{L} \mathbf{n} \cdot \mathbf{r}_{ij} \right) \right] \\ &+ \frac{1}{2} \left[\sum_{n \neq 0} \left(\frac{\text{erfc}(\alpha L n)}{Ln} + \frac{1}{\pi L n^2} \exp\left(-\frac{\pi^2 n^2}{\alpha^2 L^2} \right) \right) - \frac{2\alpha}{\sqrt{\pi}} \right] \sum_{j=1}^{N} q_j^2 \\ &+ \frac{2\pi}{3L^3} \left| \sum_{j=1}^{N} q_j \mathbf{r}_j \right|^2, \end{aligned} \tag{A.24}$$

The complementary error function is defined as:

$$\text{erfc}(x) = \frac{2}{\sqrt{\pi}} \int_x^\infty e^{-t^2} dt. \tag{A.25}$$

Various methods can be used to derive A.24, one involving the introduction of a convergence factor and a Jacobi theta-function transformation.

By choosing an optimal value for the parameter α, the sums in A.24 can be simplified, leading to the following result:

$$\begin{aligned} V &= \sum_{1 \le i < j \le N} \frac{q_i q_j \text{erfc}(\alpha r_{ij})}{r_{ij}} - \frac{\alpha}{\sqrt{\pi}} \sum_{j=1}^{N} q_j^2 \\ &+ \frac{1}{2\pi L} \sum_{n \neq 0} \left[\frac{1}{n^2} \exp\left(-\frac{\pi^2 n^2}{L^2 \alpha^2} \right) \left| \sum_{j=1}^{N} q_j \exp\left(\frac{2\pi i}{L} \mathbf{n} \cdot \mathbf{r}_j \right) \right|^2 \right]. \end{aligned} \tag{A.26}$$

The real-space terms in A.26 are now short-ranged, allowing for truncation with a spherical cutoff. The sum over Fourier space can also be truncated after a limited number of terms.

Particle-Mesh Ewald

Tom Darden introduced the Particle-Mesh Ewald (PME) method to improve the performance of the reciprocal sum. Instead of summing the wave vectors directly, charges are assigned to a grid using interpolation. GROMACS implements PME with cardinal B-spline interpolation, known as smooth PME (SPME). This method significantly improves computational efficiency.

The PME algorithm scales as $N \log(N)$, making it much faster than traditional Ewald summation for medium to large systems. For small systems, however, Ewald summation may still be preferable due to lower setup costs.

A.3 Molecular model and force field

A schematic diagram of the ions used in this study is presented in Figure A.3.

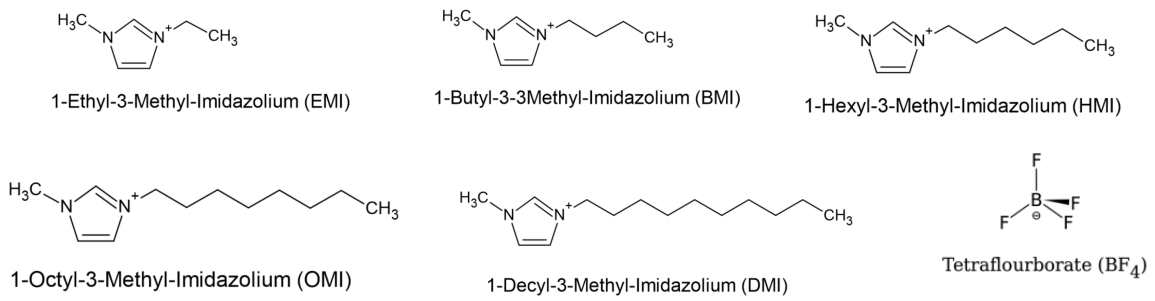

Figure A.3: Molecular structures of the ions in the ionic liquids studied in this research.

The force field parameters for EMI^+, BMI^+, HMI^+, OMI^+, and DMI^+ were adopted from [25], which is based on the AMBER force field [26]. The force field for BF_4^- was developed by J. de Andrade and his colleagues [27]. The AMBER force field was used to model both bonded and nonbonded interactions between ions.

In molecular modeling, the potential energy of a system is referred to as the force field, and the potential form of AMBER 94 can be categorized into bonded interactions (covalent bonds) and nonbonded interactions (electrostatic long-range and Van der Waals interactions). The functional form of this force field is as follows:

$$V(r^N) = \sum_{bonds} k_b(l - l_0)^2 + \sum_{angles} k_a(\theta - \theta_0)^2 + \sum_{torsions} \sum_{n} \frac{1}{2} V_n[1 + \cos(n\omega - \gamma)]$$
$$+ \sum_{j=1} \sum_{i=j+1} f_{ij} \left\{ \epsilon_{ij} \left[\left(\frac{r_{0ij}}{r_{ij}} \right)^{12} - \left(\frac{r_{0ij}}{r_{ij}} \right)^{6} \right] + \frac{q_i q_j}{4\pi\epsilon_0 r_{ij}} \right\}, \tag{A.27}$$

The first term in the equation represents the energy between covalently bonded atoms, modeled as a harmonic force (similar to an ideal spring), as shown in Figure A.4.

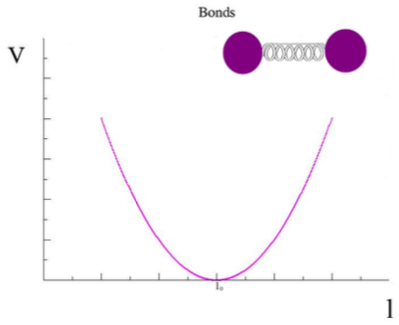

Figure A.4: Bonded interactions [28].

The second term accounts for the energy related to the geometry of the electron orbitals forming the covalent bonds, also modeled as a harmonic force, as shown in Figure A.5.

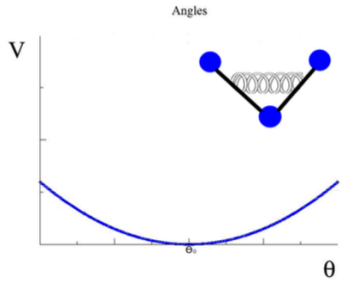

Figure A.5: Angles [28].

The third term models the energy associated with the twisting of bonds due to bond order, as illustrated in Figure A.6.

Finally, the last term represents the energy resulting from Van der Waals and electrostatic interactions, which describe the nonbonded energy between all atom pairs, as shown in Figure A.7.

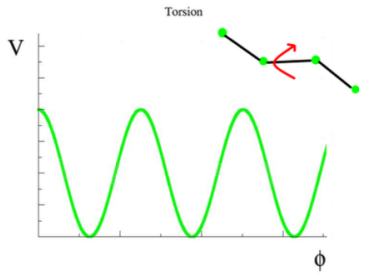

Figure A.6: Torsion [28].

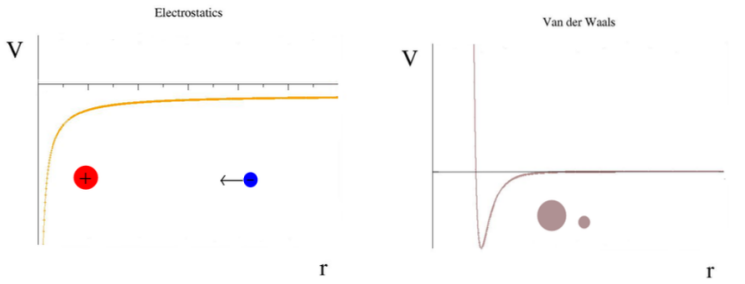

(a) Electrostatic interaction. (b) Van der Waals interaction.

Figure A.7: Non-covalent interactions [28].

A.3.1 Preparation of initial states

Cubic simulation boxes of sizes 7 and 15 nm^3, each containing 1024 ion pairs, were created by randomly inserting ions while avoiding overlaps.

To incorporate the AMBER force field within GROMACS, several input files in the current distribution were modified. A summary of these changes is provided in Appendix A.5.

The steps to prepare the systems are shown in Figure A.8:

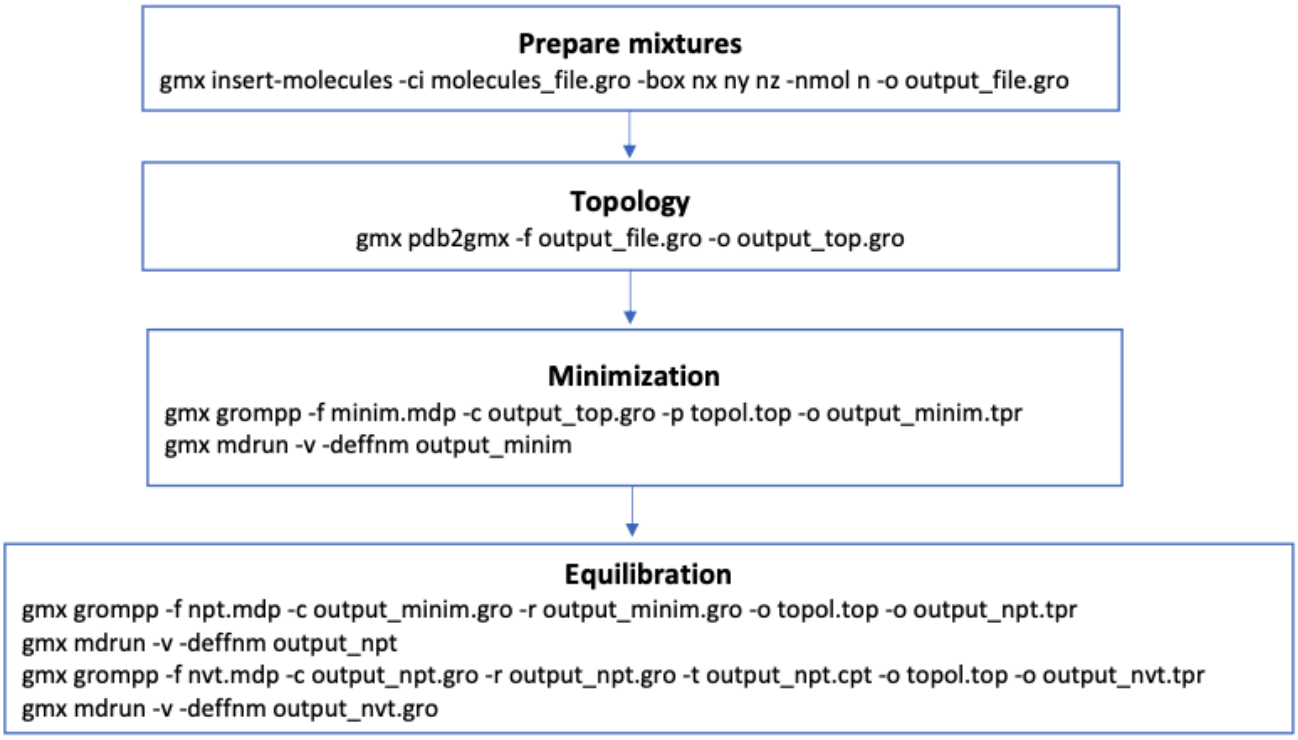

Figure A.8: Steps required to prepare the systems.

- First, we prepared the mixtures using ionic pairs and simultaneously created a cubic box. This was done using a GROMACS tool called "insert-molecules", which generates copies of the molecules and places them randomly in the available space of the selected box size. The selection of the vacant space is based on the Van der Waals radii of the atoms, and the insertion positions are randomized based on an initial seed. The nx, ny, and nz refer to the box's side lengths, while n indicates the number of ion pairs.

- Next, the topology of the molecules was created. The topology contains all the information needed to define the molecule in the simulation, such as bonded and non-bonded parameters. GROMACS offers a tool called "pdb2gmx", which generates the system's topology from the molecule's structure file containing atom positions.
- The structure of the molecules was then minimized using the steepest descent method (Saddle point theorem), and the minimization process was considered converged when the maximum force was smaller than a chosen value.
- The mixtures were then equilibrated using NVT and NPT ensembles over several steps.

A.4 Computational details and simulation methods

All simulations were conducted using the GROMACS 2022.2 MD simulation package [16, 17]. Periodic boundary conditions (PBC) were applied in all three dimensions of the cubic simulation box, and a 1.6 nm cutoff was applied to nonbonded interactions. Long-range electrostatic interactions [19, 20] were handled with the Particle Mesh Ewald (PME) method [29]. The five systems each contained 1024 ion pairs. For our study, we selected $T = 500K$ as the target simulation temperature, as experiments have shown that this temperature is well above the melting point of $EMI^+BF_4^-$ [7].

The steps for equilibration and production runs are shown in Figure A.9. The simulation process for the system $EMI^+BF_4^-$ was equilibrated and simulated as illustrated in the schematic Figure A.9, with two different paths being followed. The steps used in [7] did not yield similar results, as they were far from the desired outcomes.

The initial random configuration underwent several NPT simulations at a constant pressure of $P = 100$ atm and varying temperatures from $T = 2000K$ down to 1500, 1000, 800, 600, and $500K$. At each temperature, the system was simulated for 1 ns. The final configuration was then equilibrated with a 1 ns NPT simulation at $P = 1atm$ and $T = 500K$ to obtain the average simulation volume V. Afterward, the system underwent another simulated annealing process in the NVT ensemble, following the same temperature sequence with the determined V.

For analyzing homogeneous systems, NPT production runs were performed. The equilibrated configuration for the second path went through production runs in the NPT ensemble at $T = 500K$. Simulation durations were 10 ns and 100 ns for molecules with longer chains, allowing reliable results for dynamic properties. The obtained results are presented in Section 3.1.

The equilibrated configuration from the first path went through production runs in the NVT ensemble at $T = 500, 600, 700, 800$, and $900K$. The simulation duration was 10 ns to obtain the results in [7].

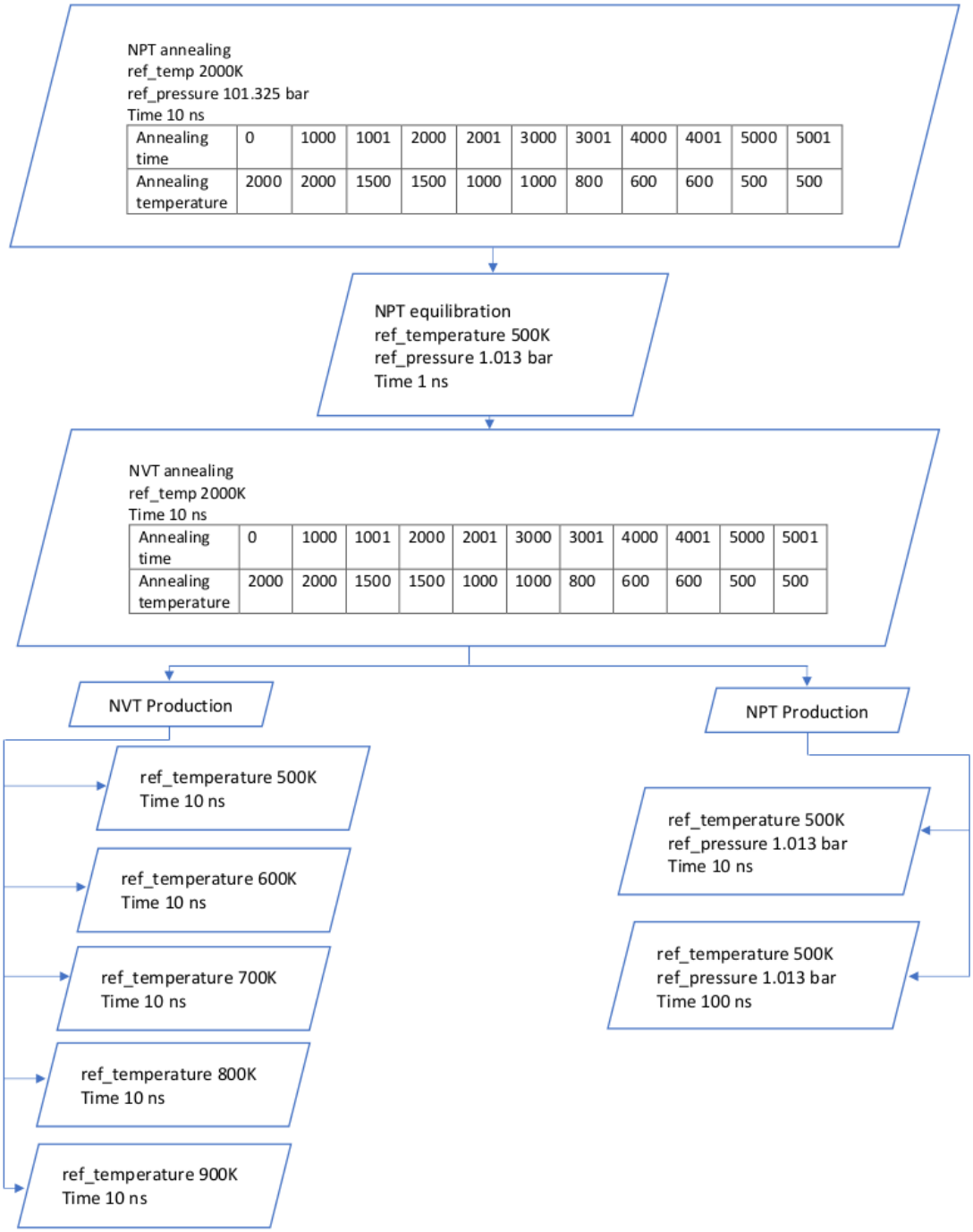

Figure A.9: Steps for simulating the systems.

A.5 Data used for system preparation

In this apendix we show the data that was used in the amber94 force field files. The folders that need to be modified in gromacs in order to perform the calculations can be found at the following paths: for resydutypes.dat the path is /usr/local/gromacs/share/gromacs/top, and for the other files they are in the path /usr/local/gromacs/share/gromacs/top/amber94.ff:

- **resyduetypes.dat**

```
EMI     Ion
BMI     Ion
HMI     Ion
DMI     Ion
BF4     Ion
```

- **atomtypes.atp**

```
B                10.81000      ; Boron atom added by PedroE for BF4-
```

- **aminoacids.rtp**

```
[ BF4 ] ; [BF4-] ADDED BY PEDROE FORM J DE ANDRADE JPCB 2002
 [ atoms ]
    B      B          0.827600       1
   F1      F         -0.456900       2
   F2      F         -0.456900       3
   F3      F         -0.456900       4
   F4      F         -0.456900       5
 [ bonds ]
    B     F1
    B     F2
    B     F3
    B     F4

[ EMI ] ; [EMI+] ADDED BY PEDROE USING YANTING'S BOOK
 [ atoms ]
   CR     CR          0.005500       1
  NA1     NA          0.092400       2
  NA2     NA         -0.002420       3
  CW1     CW         -0.163820       4
  CW2     CW         -0.167520       5
```

```
 H41      H4          0.243400      6
 H42      H4          0.242100      7
 CT1      CT         -0.197320      8
 H11      H1          0.138800      9
 H12      H1          0.138800     10
 H13      H1          0.138800     11
 CT2      CT          0.062500     12
 CT3      CT         -0.129720     13
 H14      H1          0.085800     14
 H15      H1          0.085800     15
 HC1      HC          0.068700     16
 HC2      HC          0.068700     17
 HC3      HC          0.068700     18
  H5      H5          0.220800     19
[ bonds ]
  CR     NA1
 NA1     CW1
 CW1     CW2
 CW2     NA2
 NA2      CR
 CW1     H41
 CW2     H42
 NA1     CT1
 CT1     H11
 CT1     H12
 CT1     H13
 NA2     CT2
 CT2     H14
 CT2     H15
 CT2     CT3
 CT3     HC1
 CT3     HC2
 CT3     HC3
  CR      H5
[ impropers ]
 NA1     NA2      CR      H5
  CR     CW1     NA1     CT1
  CR     CW1     NA2     CT2
```

```
  NA1      CW2    CW1    H41
  NA2      CW1    CW2    H42

[ BMI ] ; [BMI+] ADDED BY PEDROE USING YANTING'S BOOK
 [ atoms ]
   CR       CR          -0.052100         1
  NA1       NA           0.054500         2
  NA2       NA           0.035500         3
  CW1       CW          -0.094000         4
  CW2       CW          -0.157800         5
  H41       H4           0.211800         6
  H42       H4           0.237300         7
  CT1       CT          -0.103500         8
  H11       H1           0.118200         9
  H12       H1           0.118200        10
  H13       H1           0.118200        11
  CT2       CT          -0.028300        12
  CT3       CT           0.000300        13
  CT4       CT           0.018000        14
  CT5       CT          -0.086700        15
  H14       H1           0.092100        16
  H15       H1           0.092100        17
  H16       H1           0.029000        18
  H17       H1           0.029000        19
  H18       H1           0.021000        20
  H19       H1           0.021000        21
  HC1       HC           0.035700        22
  HC2       HC           0.035700        23
  HC3       HC           0.035700        24
   H5        H5          0.219000        25
 [ bonds ]
   CR      NA1
  NA1      CW1
  CW1      CW2
  CW2      NA2
  NA2       CR
  CW1      H41
  CW2      H42
```

```
  NA1      CT1
  CT1      H11
  CT1      H12
  CT1      H13
  NA2      CT2
  CT2      H14
  CT2      H15
  CT2      CT3
  CT3      H16
  CT3      H17
  CT3      CT4
  CT4      H18
  CT4      H19
  CT4      CT5
  CT5      HC1
  CT5      HC2
  CT5      HC3
   CR       H5
[ impropers ]
  NA1      NA2      CR       H5
   CR      CW1      NA1      CT1
   CR      CW1      NA2      CT2
  NA1      CW2      CW1      H41
  NA2      CW1      CW2      H42

[ HMI ] ; [HMI+] ADDED BY PEDROE AND JCAS USING YANTING'S BOOK
[ atoms ]
   CR       CR          -0.056000         1
  NA1       NA           0.056100         2
  NA2       NA           0.031900         3
  CW1       CW          -0.105500         4
  CW2       CW          -0.159400         5
  H41       H4           0.216100         6
  H42       H4           0.242200         7
  CT1       CT          -0.100800         8
  H11       H1           0.118000         9
  H12       H1           0.118000        10
  H13       H1           0.118000        11
```

```
  CT2      CT        -0.018100      12
  CT3      CT         0.016200      13
  CT4      CT        -0.006200      14
  CT5      CT        -0.012500      15
  CT6      CT         0.023400      16
  CT7      CT        -0.095500      17
  H14      H1         0.090000      18
  H15      H1         0.090000      19
  H16      H1         0.022800      20
  H17      H1         0.022800      21
  H18      H1         0.013200      22
  H19      H1         0.013200      23
  H1A      H1         0.012500      24
  H1B      H1         0.012500      25
  H1C      H1         0.011800      26
  H1D      H1         0.011800      27
  HC1      HC         0.030300      28
  HC2      HC         0.030300      29
  HC3      HC         0.030300      30
   H5      H5         0.222400      31
[ bonds ]
   CR     NA1
  NA1     CW1
  CW1     CW2
  CW2     NA2
  NA2      CR
  CW1     H41
  CW2     H42
  NA2     CT1
  CT1     H11
  CT1     H12
  CT1     H13
  NA1     CT2
  CT2     H14
  CT2     H15
  CT2     CT3
  CT3     H16
  CT3     H17
```

```
  CT3      CT4
  CT4      H18
  CT4      H19
  CT4      CT5
  CT5      H1A
  CT5      H1B
  CT5      CT6
  CT6      H1C
  CT6      H1D
  CT6      CT7
  CT7      HC1
  CT7      HC2
  CT7      HC3
   CR       H5
 [ impropers ]
  NA1      NA2      CR       H5
   CR      CW1      NA1      CT1
   CR      CW1      NA2      CT2
  NA1      CW2      CW1      H41
  NA2      CW1      CW2      H42

[ DMI ] ; [DMI+] ADDED BY JCAS USING YANTING'S BOOK
 [ atoms ]
   CR       CR            -0.058700          1
  NA1       NA             0.035300          2
  NA2       NA             0.059600          3
  CW1       CW            -0.095600          4
  CW2       CW            -0.159200          5
  H41       H4             0.210100          6
  H42       H4             0.239400          7
  CT1       CT            -0.100100          8
  H11       H1             0.116500          9
  H12       H1             0.116500         10
  H13       H1             0.116500         11
  CT2       CT            -0.018200         12
  CT3       CT             0.005400         13
  CT4       CT            -0.001100         14
  CT5       CT            -0.013100         15
```

CT6	CT	0.017400	16
CT7	CT	−0.003200	17
H14	H1	0.090000	18
H15	H1	0.090000	19
H16	H1	0.025100	20
H17	H1	0.025100	21
H18	H1	0.014400	22
H19	H1	0.014400	23
H1A	H1	0.009400	24
H1B	H1	0.009400	25
H1C	H1	0.003100	26
H1D	H1	0.003100	27
HC1	HC	0.025000	28
HC2	HC	0.025000	29
HC3	HC	0.025000	30
H5	H5	0.222100	31
CT8	CT	0.006900	32
CT9	CT	−0.005500	33
CTA	CT	0.036300	34
CTB	CT	−0.100600	35
H1E	H1	0.005900	36
H1F	H1	0.005900	37
H1G	H1	0.001900	38
H1H	H1	0.001900	39
H1I	H1	−0.001500	40
H1J	H1	−0.001500	41
H1K	H1	0.000800	42
H1L	H1	0.000800	43

[bonds]

CR	NA1
NA1	CW1
CW1	CW2
CW2	NA2
NA2	CR
CW1	H41
CW2	H42
NA2	CT1
CT1	H11

```
 CT1      H12
 CT1      H13
 NA1      CT2
 CT2      H14
 CT2      H15
 CT2      CT3
 CT3      H16
 CT3      H17
 CT3      CT4
 CT4      H18
 CT4      H19
 CT4      CT5
 CT5      H1A
 CT5      H1B
 CT5      CT6
 CT6      H1C
 CT6      H1D
 CT6      CT7
 CT7      H1K
 CT7      H1L
 CT7      CT8
 CT8      H1I
 CT8      H1J
 CT8      CT9
 CT9      H1E
 CT9      H1F
 CT9      CTA
 CTA      H1G
 CTA      H1H
 CTA      CTB
 CTB      HC1
 CTB      HC2
 CTB      HC3
  CR       H5
[ impropers ]
 NA1      NA2      CR       H5
  CR      CW1      NA1      CT1
  CR      CW1      NA2      CT2
```

```
NA1     CW2     CW1     H41
NA2     CW1     CW2     H42
```

- **ffbonded.itp**

```
[ bondtypes ]
  B   F           1     0.13930    242672.0  ; ADDED BY PEDROE FOR BF4 FORM
  J DE ANDRADE JPCB 2002
  CT NA           1     0.14750    282001.6  ; ADDED BY PEDROE FOR EMI
  FROM YANTING'S BOOK
  CW CW           1     0.13700    455136.0  ; ADDED BY PEDROE FOR EMI
  FROM YANTING'S BOOK

[ angletypes ]
F   B   F           1    109.500     418.400  ; ADDED BY PEDROE FOR BF4
FORM J DE ANDRADE JPCB 2002
CR  NA  CT          1    109.500     292.880  ; ADDED BY PEDROE FOR EMI
FORM YANTING'S BOOK
CW  NA  CT          1    120.000     292.880  ; ADDED BY PEDROE FOR EMI
FORM YANTING'S BOOK
NA  CW  CW          1    120.000     585.760  ; ADDED BY PEDROE FOR EMI
FORM YANTING'S BOOK
CW  CW  H4          1    128.500     292.880  ; ADDED BY PEDROE FOR EMI
FORM YANTING'S BOOK
NA  CT  H1          1    109.500     292.880  ; ADDED BY PEDROE FOR EMI
FORM YANTING'S BOOK
NA  CT  CT          1    111.200     669.440  ; ADDED BY PEDROE FOR EMI
FORM YANTING'S BOOK

[ dihedraltypes ] importers
CR  CW  NA  CT      4      180.00     4.69240     2     ; ADDED BY
PEDROE FOR EMI FROM YANTING'S BOOK

[ dihedraltypes ]
H1   CT  NA  CR    9      000.0      0.00000     2   ; ADDED BY PEDROE
FOR EMI FROM YANTING'S BOOK
H1   CT  NA  CW    9      000.0      0.00000     2   ; ADDED BY PEDROE
FOR EMI FROM YANTING'S BOOK
CR   NA  CT  CT    9      000.0      0.00000     2   ; ADDED BY PEDROE
```

```
FOR EMI FROM YANTING'S BOOK
CW   NA   CT   CT    9      000.0       0.00000      2   ; ADDED BY PEDROE
FOR EMI FROM YANTING'S BOOK
NA   CW   CW   NA    9      180.0      22.48900      2   ; ADDED BY PEDROE
FOR EMI FROM YANTING'S BOOK
NA   CW   CW   H4    9      180.0      22.48900      2   ; ADDED BY PEDROE
FOR EMI FROM YANTING'S BOOK
H4   CW   CW   H4    9      180.0      22.48900      2   ; ADDED BY PEDROE
FOR EMI FROM YANTING'S BOOK
```

- **ffnonbonded.itp**

```
B          5       10.81      0.0000   A   3.58140e-01   3.97480e-01
```

A.6 Units used in Gromacs

Quantity	Unit
length	$nm = 10^{-9}$
mass	u (unified atomic mass unit) = $1.660538921 \times 10^{-27} kg$
time	$ps = 10^{-12} s$
charge	e = elementary charge = $1.602176565 \times 10^{-19} C$
temperature	K

Table A.1: Basic units used in GROMACS

Quantity	Unit
energy	kJ mol^{-1}
Force	kJ mol^{-1} nm^{-1}
pressure	bar
velocity	nm ps^{-1} = 1000 m s^{-1}
dipole moment	e nm
electric potential	kJ mol^{-1} e^{-1} = 0.01036426919 Volt
electric field	kJ mol^{-1} nm^{-1} e^{-1} = $1.036426919 \times 10^{7}$ Vm^{-1}

Table A.2: Derived units.

Symbol	Name	Value
N_{AV}	Avogadro's number	$6.02214129 \times 10^{23}$ mol^{-1}
R	gas constant	8.3144621×10^{-3} kJ mol^{-1} K^{-1}
k_B	Boltzmann's constant	$idem$
h	Planck's constant	0.399031271 kJ mol^{-1}ps
$\hbar$	Dirac's constant	0.0635077993 kJ mol^{-1}ps
c	velocity of light	299792.458 nm ps^{-1}

Table A.3: Physical constants

Bibliography

[1] Zhigang Lei,Biaohua Chen, Yoon-Mo Koo. *Introduction: Ionic Liquids* DOI: 10.1021/acs.chemrev.7b00246 Chem. Rev. 2017, 117, 6633-6635.

[2] Rogers, R. D. CHEMISTRY: Ionic Liquids–Solvents of the Future? Science 2003, 302 (5646), 792-793.

[3] Plechkova, N. V.; Seddon, K. R. Applications of Ionic Liquids in the Chemical Industry. Chem. Soc. Rev. 2008, 37 (1), 123-150.

[4] Mariana E. Farias-Anguiano, Luis E. Sánchez-Días, Ernesto C. Cortes-Morales, and Pedro E. Ramírez González, *General framework for the study of dynamical properties and arrested states of ionic liquids*, Phys. Fluids 34, 084108 (2022); doi: 10.1063/5.0095000.

[5] Pedro E. Ramírez-González, Luis E. Sanchéz-Díaz, Magdaleno Medina-Noyola, and Yanting Wang, *Communication: Probing the existence of partially arrested states in ionic liquids*, http://dx.doi.org/10.1063/1.4967518.

[6] L. E. Sanchez-Díaz, A. Vizcarra-Rendón, and R. Juárez-Maldonado, Phys. Rev. Lett. 103, 035701 (2009).

[7] Pedro E. Ramírez-González, Gan Ren, Giacomo Saielli, and Yanting Wang *Effect of Ion Rigidity on Physical Properties of Ionic Liquids Studied by Molecular Dynamics Simulation*, DOI: 10.1021/acs.jpcb.6b03379.

[8] H. Tanaka, J. Meunier, and D. Bonn, Phys. Rev. E 69, 031404 (2004).

[9] A. Laskar, *Superionic Solids and Solid Electrolytes Recent Trends* (Elsevier, 2012).

[10] A. Varzi, R. Raccichini, S. Passerini, and B. Scrosati, *"Challenges and prospects of the role of solid electrolytes in the revitalization of lithium metal batteries"*, J. Mater. Chem. A (published online).

[11] M. G. Del Popolo and G. A. Voth, J. Phys. Chem. B 108, 1744 (2004).

[12] J. Habasaki and K. L. Ngai, J. Chem. Phys. 142, 164501 (2015).

[13] Grzybowski, Andrzej, *"Glass Transition and Related Phenomena"*, International Journal of Molecular Sciences (2023)

[14] Habasaki, Junko and Leon, Carlos and Ngai, KL, *"Dynamics of glassy, crystalline and liquid ionic conductors"*, Springer (2017).

[15] Ivanov, Mikhail Yu and Surovtsev, Nikolay V and Fedin, Matvey V, *"Ionic liquid glasses: properties and applications"*, Russian Chemical Reviews (2022).

[16] M.J. Abraham, T. Murtola, R. Schulz, S. Páll, J.C. Smith, B. Hess, and E. Lindahl, *"GROMACS: High performance molecular simulations through multi-level parallelism from laptops to supercomputers"*, SoftwareX, 1–2 19–25 (2015).

[17] S. Páll, M.J. Abraham, C. Kutzner, B. Hess, and E. Lindahl, *"Tackling exascale software challenges in molecular dynamics simulations with GROMACS"*; pp. 3–27 in Solving software challenges for exascale. Edited by S. Markidis and E. Laure. Springer International Publishing Switzerland, London, 2015.

[18] M. P. Allen, *Introduction to Molecular Dynamics Simulation*, 1-28 (2004).

[19] M.P. Allen, D.J. Tildesley, *Computer Simulation of Liquids*, First Edition, Oxford University Press (1991).

[20] D. Frenkel, B. Smit, *Understanding molecular simulation: from algorithms to aplications*, Academic Press (1996).

[21] Junko Habasaki, Carlos Leon, K.L Ngai, *Dynamics of Glassy, Crystalline and Liquid Ionic Conductors. Experimentes, Theories, Simulations*. Topics in Applied Physics 132, Springer (2017).

[22] J.P. Hansen, I.R. McDonald, *Theory of Simple Liquids*, Third Edition, Elsevier Science Publishing, San Diego (2006).

[23] Rapaport, D. C. *The Art of Molecular Dynamics Simulation*. Cambridge university press. ISBN 0-521-44561-2, UK (1997).

[24] J.M Haile, *Molecular Dynamis Simulation Elementary Methods*, a Wiley-Interscience publication (1997).

[25] Wang, Y.; Jiang, W.; Voth, G. A. *Spatial Heterogeneity in Ionic Liquids*. In Ionic Liquids IV; Brennecke, J. F., Rogers, R. D., Seddon, K. R., Eds.; American Chemical Society: Washington, DC, 2007; Vol. 975, pp 272-307.

[26] Cornell, W. D.; Cieplak, P.; Bayly, C. I.; Gould, I. R.; Merz, K. M.; Ferguson, D. M.; Spellmeyer, D. C.; Fox, T.; Caldwell, J. W.; Kollman, P. A. A Second Generation Force Field for the Simulation of Proteins, Nucleic Acids, and Organic Molecules. J. Am. Chem. Soc. 1995, 117 (19), 5179-5197.

[27] de Andrade, J.; Böes, E. S.; Stassen, H. Computational Study of Room Temperature Molten Salts Composed by 1-Alkyl-3-Methyl-imidazolium CationsForce-Field Proposal and Validation. J. Phys.Chem. B 2002, 106 (51), 13344-13351.

[28] Rodrigo Rodríguez Gutiérrez, *Comparative study of dynamical and structural properties of two eutectic solvents, using molecular dynamics simulation*, Tesis para obtener el grado de maestro en ciencias (física), Universidad Autónoma de San Luis Potosí.

[29] Essmann, U.; Perera, L.; Berkowitz, M. L.; Darden, T.; Lee, H.; Pedersen, L. G. A Smooth Particle Mesh Ewald Method. J. Chem. Phys. 1995, 103 (19), 8577.

[30] Rogers, Robin D and Seddon, Kenneth R, *Ionic liquids: industrial applications for green chemistry*, ACS Publications, 2002.

[31] D. A. McQuarrie, *Statistical Mechanics*, First Edition, Harper and Row (1976).

[32] Xingang Jia, Xiaoling Hu, Kehe Su, Wenzhen Wang, Chunbao Du. *Molecular screening of ionic liquids for CO_2 absorption and molecular dynamic simulation*, https://doi.org/10.1515/chem-2022-0154.

[33] Tsun-Mei Chang, and Stephanie E. Billeck. *Structure, Molecular Interactions, and Dynamics of Aqueous [BMIM][BF_4] Mixtures: A Molecular Dynamics Study*, https://doi.org/10.1021/acs.jpcb.0c09731, J. Phys. Chem. B 2021, 125, 1227-1240.

[34] E. GonzálezTovar, M. LozadaCassou, L. MieryTerán, and M. MedinaNoyola, *Thermodynamics and structure of the primitive model near its gas–liquid transition*, The Journal of Chemical Physics 95, 6784 (1991); doi: 10.1063/1.461516.

[35] L. E. Sánchez-Díaz, A. Vizcarra-Rendón, and M. Medina-Noyola, *Generalized mean spherical approximation for the multicomponent restricted primitive model*,The Journal of Chemical Physics 132, 234506 (2010); doi: 10.1063/1.3455336.

[36] J. Li, *Basic Molecular Dynamics*, Handbook of Materials Modeling, 565-588(2005).

[37] A. R. Leach, *Molecular Dynamics: Simulation Methods*, Chapter 7, in Molecular Modelling Principles and Applications, Pearson Prentice Hall.

[38] C. N. Yang and R. Mills, Phys. Rev. **96**, 191 (1954).

[39] GROMACS development team, *GROMACS Documentation, Release 2022*, (2022).

[40] H. Goldstein, C. Poole, J. Safko, *Classical Mechanics*, Third Edition, Addison Wesley (2002).

[41] J. Meller, *Molecular Dynamics*, Cornell University, Nature Publishing Group(2005).

[42] https://manual.gromacs.org/current/install-guide/index.html

[43] J.A. Lemkul (2018) *"From Proteins to Perturbed Hamiltonians: A Suite of Tutorials for the GROMACS-2018 Molecular Simulation Package, v1.0"* Living J. Comp. Mol. Sci. 1 (1): 5068.

[44] Rodrigo Rodríguez Gutiérrez, *Comparative study of dynamical and structural properties of two eutectic solvents, using molecular dynamics simulation*. Master's Thesis, UASLP.

[45] C. A. Angell, Science 267, 1924 (1995).

[46] P. G. Debenedetti and F. H. Stillinger, Nature (London) 410, 259 (2001).

[47] W. Götze, in *Liquids, Freezing and Glass Transition*, edited by J. P. Hansen, D. Levesque, and J. Zinn-Justin (North-Holland, Amsterdam, 1991).

[48] J. Bergenholtz and M. Fuchs, Phys. Rev. E 59, 5706 (1999).

[49] L. Fabbian et al., Phys. Rev. E 59, R1347 (1999); 60, 2430 (1999).

[50] K. N. Pham et al., Science 296, 104 (2002).

[51] E. Zaccarelli et al., Phys. Rev. Lett. 92, 225703 (2004).

[52] R. Juárez-Maldonado and M. Medina-Noyola, Phys. Rev. E 77, 051503 (2008).

[53] R. Juárez-Maldonado and M. Medina-Noyola, Phys. Rev. Lett. 101, 267801 (2008).

[54] Elizondo-Aguilera, Luis Fernando and Voigtmann, Th., *Glass-transition asymptotics in two theories of glassy dynamics: Self-consistent generalized Langevin equation and mode-coupling theory*, Physical Review E, APS (2019).

[55] L. M. Janssen, *"Mode-coupling theory of the glass transition: A primer,"* Front. Phys. 6, 97 (2018).

[56] F. H. Stillinger and P. G. Debenedetti, *"Glass transition thermodynamics and kinetics,"* Annu. Rev. Condens. Matter Phys. 4(1), 263–285 (2013).

[57] P. G. Debenedetti and F. H. Stillinger, *"Supercooled liquids and the glass transition,"* Nature 410(6825), 259–267 (2001).

[58] L. Berthier and G. Biroli, *"Theoretical perspective on the glass transition and amorphous materials,"* Rev. Mod. Phys. 83(2), 587–645 (2011).

[59] C. A. Angell, K. L. Ngai, G. B. McKenna, P. F. McMillan, and S. W. Martin, *"Relaxation in glassforming liquids and amorphous solids,"* J. Appl. Phys. 88(6), 3113–3157 (2000).

[60] Juan C. Avilés-Sánchez, Ernesto C. Cortes-Morales, Mariana E. Farías-Anguiano, Jonathan K. Whitmer, and Pedro E. Ramírez-Gonzalez. *Linking dynamics and structure in highly asymmetric ionic liquids*. Phys. Fluids 37, 017173 (2025); doi: 10.1063/5.0245688. https://doi.org/10.1063/5.0245688.

[61] MacFarlane, D. R., Tachikawa, N., Forsyth, M., Pringle, J. M., Howlett, P. C., Elliott, G. D., et al. (2014). *Energy applications of ionic liquids*. Energy Environ. Sci. 7, 232-250. doi: 10.1039/C3EE42099J

[62] Bhattacharyya, S., Filippov, S., and Shah, F. U. (2017). *High CO_2 absorption capacity by chemisorption at cations and anions in choline-based ionic liquids*. Phys. Chem. Chem. Phy. 19, 31216-31226. doi: 10.1039/C7CP07059D

[63] Shah, F. U., Gnezdilov, O., and Filippov, A. (2017). *Ion dynamics in halogen-free phosphonium bis(salicylato)borate ionic liquid electrolytes for lithium-ion batteries*. Phys. Chem. Chem. Phys. 19, 16721-16730. doi: 10.1039/C7CP02722B

[64] Egorova, K. S., Gordeev, E. G., and Ananikov, V. P. (2017). *Biological activity of ionic liquids and their application in pharmaceutics and medicine*. Chem. Rev. 117, 7132-7189. doi: 10.1021/acs.chemrev.6b00562

[65] Shah, F. U., Gnezdilov, O. I., Khan, I., Filippov, A., Slad, N. A., and Johansson, P. (2020). *Structural and ion dynamics in fluorine-free oligoether carboxylate ionic liquid-based electrolytes*. J. Phys. Chem. B 124, 9690-9700. doi: 10.1021/acs.jpcb.0c04749

[66] L. C. Merrill, X. C. Chen, Y. Zhang, H. O. Ford, K. Lou, Y. Zhang, G. Yang, Y. Wang, Y. Wang, J. L. Schaefer, and N. J. Dudney, *Polymer–ceramic composite electrolytes for lithium batteries: A comparison between the single-ion-conducting polymer matrix and its counterpart*, ACS Appl. Energy Mater. 3, 8871 (2020).